X-ray and light scattering from nanostructured thin films

Bassi, Andrea Li

X-ray and Light Scattering from Nanostructured Thin Films

by

Andrea Li Bassi

A thesis submitted in partial fulfilment of the requirements for the degree of Doctor of Philosophy

The University of Durham

Department of Physics

2000

X-ray and Light Scattering from Nanostructured Thin Films

by

Andrea Li Bassi

A thesis submitted in partial fulfilment of the requirements for the degree of Doctor of Philosophy, The University of Durham (2000)

Abstract

The object of this thesis is the study of nanostructured thin films using inelastic light scattering and elastic x-ray scattering techniques. Their use in combination with other techniques is a powerful tool for the investigation of nanostructured materials.

X-ray, Raman and Brillouin characterisation of cluster-assembled carbon films, promising for applications in the field of catalysis, hydrogen storage and field emission, is here presented. X-ray reflectivity (XRR) provided a measure of the density. Raman spectroscopy showed that the local bonding in these amorphous films depends on the size distribution of the clusters and that it is possible to select the cluster size in order to grow films with tailored properties. Brillouin scattering provided a characterisation at the mesoscopic scale and an estimate of the elastic constants, revealing a very soft material.

XRR was employed to study density, layering and roughness of a wide range of amorphous carbon films grown with different techniques. Some films possess an internal layering due to plasma instabilities in the deposition apparatus. By comparing XRR with Electron Energy Loss Spectroscopy, a unique value for the electron "effective mass" was deduced and a general relationship between sp^3 content and density was found. XRR and H effusion were used to determine the hydrogen content.

A study of the size-dependent melting temperature in tin nanoparticle thin films was undertaken with a combined use of X-Ray Diffraction (XRD) and light scattering. A redshift in the position of a Rayleigh peak in the temperature-dependent Brillouin measurements was shown to be related to the melting of the nanoparticles and explained by an effective medium model. XRD also provided information on the low level of stress in the particles. Low-frequency Raman scattering was used to study the behaviour of the acoustic modes of a single particle as a function of temperature.

Acknowledgements

After three years spent between England and Italy, this work represents the final result of a most remarkable experience. It is the occasion to thank all the people who have helped me, in some way, during this period.

First of all I would like to thank my supervisors, Prof. Brian Tanner and Prof. Carlo Bottani, for their invaluable continuous guidance and support, for the trust they put in me and in my work, and for their continuous availability to discussion. Working with them has been an enjoyable and enriching experience.

For the same reasons, I would also like to thank Dr. Paolo Milani, whose feverish activity is at the origin of the research project in which I have been involved.

All of them contributed to the funding of my research, thus giving me the opportunity to continue my studies.

I would like to thank all the people with whom I have been working, for their help and their contribution to this research: Andrea Ferrari, Marco Beghi, Paolo Ossi, Rosanna Pastorelli, Carlo Casari, Andrea Amici, Anna Fioravanti, Paolo Piseri, Emanuele Barborini, Alessandro Podesta', Angiolino Stella, Paolo Tognini, Thomas Hase, Brian Fulthorpe, Ian Pape, John Clarke, John Robertson, the two amazing technicians, John Dobson and Antonio Mantegazza, and many others.

I thank all the researchers and technicians who helped me in my experiments at synchrotron sources.

I would also like to thank all those with whom I spent most of my time in the laboratory or in the office: Dan Read, Ian Daniel, Gwyn Ashcroft, Neil Parkinson, Amir Rozatian, Sean Giblin, Candid Reig, Juan Gonzalez, Luo Guangming, Simon Keys, Adrian Sneary, Stuart Wilkins, Anna Facibeni, Roberto Ferulano, Valeria Russo, Simone Mutti. I am sure I am forgetting someone. Sharing my time with them has been great fun and made my work easier.

Finally I would like to thank my family. Without them nothing of this would have been possible.

List of Publications

The following publications relate to the work presented in this thesis:

Chapter 4

- A.C. Ferrari, B. Kleinsorge, G. Adamopoulos, J. Robertson, W.I. Milne, V. Stolojan, L.M. Brown, A. Li Bassi, B.K. Tanner

Determination of bonding in amorphous carbons by electron energy loss spectroscopy, Raman scattering and X-ray reflectivity
JOURNAL OF NON-CRYSTALLINE SOLIDS 2000, Vol. 266-269, pp.765-768

- A. Li Bassi, A.C. Ferrari, V. Stolojan, B.K. Tanner, J. Robertson, L.M. Brown

Measurement of density, sp^3 content and internal layering of DLC films by X-ray reflectivity and electron energy loss spectroscopy
DIAMOND AND RELATED MATERIALS 2000, Vol. 9, p. 711

- V. Stolojan, L.M. Brown, A.C. Ferrari, J. Robertson, A. Li Bassi, B.K. Tanner

Comparative Study of Properties of DLC films by EELS and XRR
INSTITUTE OF PHYSICS CONFERENCE SERIES 1999 Vol. 161 pp 361-364

- A.C. Ferrari, A. Li Bassi, B.K. Tanner, V. Stolojan, J. Yuan, L.M. Brown, S.E. Rodil, B. Kleinsorge, J. Robertson

Density, sp^3 fraction and cross-sectional structure of amorphous carbons by x-ray reflectivity and electron energy loss spectroscopy
PHYSICAL REVIEW B 2000, Vol. 62, pp. 11089-11103

Chapter 5

- P. Milani, E. Barborini, P. Piseri, C.E. Bottani, A.C. Ferrari, A. Li Bassi

Nanostructured carbon films from supersonic cluster beam deposition: structure and morphology
EUROPEAN PHYSICAL JOURNAL D 1999, Vol. 9, pp. 63-68

- C. Lenardi, P. Piseri, V. Briois, C.E. Bottani, A. Li Bassi, P. Milani

Near-edge x-ray absorption fine structure and Raman characterization of amorphous and nanostructured carbon films
JOURNAL OF APPLIED PHYSICS 1999, Vol 85, Iss 10, pp 7159-7167

- E. Barborini, P. Piseri, A. Li Bassi, A.C. Ferrari, C.E. Bottani, P. Milani

Synthesis of carbon films with controlled nanostructure by separation of neutral clusters in supersonic beams
CHEMICAL PHYSICS LETTERS 1999, Vol 300, Iss 5-6, pp 633-638

- A. Li Bassi, P. Piseri, P. Milani, A.C. Ferrari, C.E. Bottani, C. Cepek, L. Giovanelli, E. Magnano, M. Sancrotti

Carbon-based nanostructured materials via cluster beam deposition: A multi-technique investigation
SURFACE SCIENCE 1998, Vol 404, Iss 1-3, pp 441-444

Chapter 6

- C.E. Bottani, A. Li Bassi, B.K. Tanner, A. Stella, P. Tognini, P. Cheyssac, R. Kofman

Melting in metallic Sn nanoparticles studied by surface Brillouin scattering and synchrotron-x-ray diffraction
PHYSICAL REVIEW B-CONDENSED MATTER 1999, Vol 59, Iss 24, pp R15601-R15604

- A. Li Bassi, C.E. Bottani, B.K. Tanner, A. Stella, P. Tognini, P. Cheyssac, R. Kofman

Origin of anomalous Brillouin redshift during melting of metallic Sn
Accepted for publication in EUROPEAN PHYSICAL JOURNAL B

- A. Li Bassi, C.E. Bottani, A. Stella, P. Tognini, P. Cheyssac, R. Kofman

Damped and overdamped acoustic phonons in tin nanoparticles detected by low frequency Raman scattering
Accepted for publication in PHYSICA E

- C.E. Bottani, A. Li Bassi, B.K. Tanner, A. Stella, P. Tognini, P. Cheyssac., R. Kofman

Brillouin scattering investigation of melting in Sn nanoparticles
Accepted for publication in PHYSICA E

Declaration

I hereby declare that the work contained in this thesis is my own and has not been submitted previously for any other degree. The work of collaborators is acknowledged at the appropriate point. In particular I would like to declare that:

- the films studied in Chapter 4 were produced and characterised, except for the X-ray reflectivity measurements here presented, by J. Robertson, A.C. Ferrari and co-workers of the Department of Engineering, University of Cambridge, and the EELS measurements were performed by V. Stolojan and L.M. Brown of Cavendish Laboratories, Cambridge;
- the films studied in Chapter 5 were produced and characterised, except for the Raman, Brillouin and X-ray scattering measurements here presented, by P. Milani and co-workers of the Nanoaggregates Laboratory, University of Milan; moreover, the simulation of the phonon dispersion relations for the determination of the elastic constants in thin films and the evaluation of the elasto-optic constants were performed by C. Casari of the Materials Laboratory, Politecnico di Milano;
- the films studied in Chapter 6 were produced by P. Cheyssac and R. Kofman of the Condensed Matter Physics Laboratory, University of Nice.

X-Ray and Light Scattering from Nanostructured Thin Films

Table of Contents

Chapter 1: Introduction page 1

1.1 Nanostructured materials 1

1.2 X-ray and inelastic light scattering techniques 4

1.3 Aim of this thesis 7

1.4 Thesis outline 8

References for Chapter 1 9

Chapter 2: Experimental techniques: fundamental physics 11

2.1 Introduction 11

2.2 Raman scattering 12

2.2.1 *Classical theory* 12

2.2.2 *Quantum theory* 14

2.2.3 *Raman tensor and selection rules* 15

2.2.4 *Raman scattering from small crystalline domains and amorphous materials* 16

2.3 Brillouin scattering 17

2.3.1 *Phonon-photon interaction kinematics* 17

2.3.2 *Elastic properties of materials* 19

2.3.3 *Elasto-optic coupling* 20

2.3.4 *Theory of Brillouin scattering cross section* 21

2.3.5 *Surface acoustic phonons* 22

2.3.6 *Opaque materials* 23

2.3.7 *Ripple effect* 25

2.4 Grazing incidence x-ray reflectivity 25
2.5 X-ray diffraction 28
2.6 Radial distribution study of non-crystalline materials 29
2.7 Small angle x-ray scattering 30
References for Chapter 2 32

Chapter 3: Experimental apparatus and data analysis 36
3.1 Raman scattering 36
3.1.1 *Experimental apparatus* 36
3.1.2 *In-situ Raman scattering* 37
3.2 Brillouin scattering 38
3.2.1 *Experimental apparatus* 38
3.2.2 *Analysis software* 41
3.3 X-ray scattering 41
3.3.1 *Experimental setups* 41
3.3.2 *Analysis software* 46
References for Chapter 3 46

Chapter 4: X-ray reflectivity from amorphous carbon films 48
4.1 Introduction 48
4.2 Samples 50
4.3 Experiment 52
4.3.1 *EELS* 52
4.3.1.1 Plasmon energy 53
4.3.2 *X-ray reflectivity* 54
4.3.2.1 Density determination 55
4.4 Results 63
4.4.1 *X-ray reflectivity* 63
4.4.1.1 Density and layering 63
4.4.1.2 Etching 70
4.4.1.3 Roughness 70

4.4.1.4 Comparison of film uniformity 71
4.4.2 *Comparison with EELS* 74
4.4.3 *Hydrogen content* 76
4.5 Conclusions 77
References for Chapter 4 78

Chapter 5: Raman and Brillouin scattering from cluster-assembled carbon films 82
5.1 Introduction 82
5.2 Sample deposition apparatus 83
5.3 Raman scattering from cluster-assembled carbon films 90
5.3.1 *Raman scattering from carbon and fitting of carbon spectra* 90
5.3.2 *Amorphous character of the cluster-assembled carbon films* 94
5.3.3 *Characterisation of carbon materials produced in the arc discharge* 97
5.3.4 *Raman scattering study of the inertial separation effect* 100
5.3.5 *Deposition of films by focused beams* 104
5.3.6 *Possible presence of large graphitic particles in the centre of the beam* 105
5.4 Density measurements by x-ray reflectivity 106
5.5 Brillouin scattering from cluster-assembled carbon films 108
5.5.1 *Films grown by a non-focused beam* 108
5.5.2 *Films grown by a focused beam* 114
5.6 Disorder and confined modes 120
5.7 Conclusions 122
References for Chapter 5 123

Chapter 6: Melting of tin nanoparticles 130
6.1 Introduction 130
6.2 Description of the samples and sample growth 132
6.3 Brillouin scattering 133

6.4 X-ray diffraction 140
6.4.1 *Temperature calibration* 143
6.4.2 *XRD as a function of temperature* 147
6.5 Raman scattering and low-frequency Raman scattering 150
6.5.1 *Experimental results* 152
6.5.2 *Discussion* 155
6.6 Conclusions 159
References for Chapter 6 160

Chapter 7: Conclusions 164
7.1 Summary 164
7.2 Further work 166

Chapter 1

Introduction

1.1 Nanostructured materials

The growth of new materials with tailored properties is one of the most active areas of scientific research. In recent years great efforts have been devoted to the exploitation of novel structures, objects and phenomena rather than to the explanation of fundamental laws. Condensed matter physics has become, at least in part, the synthesis and the study of materials that did not before exist. One of the main fields of this research has been the study of structures whose properties (compositional, chemical, morphological, mechanical, electronic, vibrational, etc.) are related to characteristic lengths of the order of nanometres. These materials are called *nanostructured* materials, and *nanostructures*, *nanoparticles*, *nanotubes*, *nanowires* have become common words in modern physics.

There are two distinct domains where nanostructures can be interesting for applications. The first is related to the desirability of miniaturising electronic devices. The second and more interesting domain is that of the nanostructured materials (e.g. in the form of films, or nanoparticles...) that show attractive mechanical, catalytic, magnetic, electronic and optical properties different from their bulk or even microcrystalline counterparts [1-4]. The physics and chemistry of solids have shown that most properties of solids depend on the microstructure or nanostructure, the chemical composition, the arrangement of atoms, and the size of the solid in one, two or three dimensions. By changing one or more of these parameters, the properties of the solid change. In nanostructured materials a significant fraction of atoms is in a configuration different from the bulk configuration (i.e. grain boundaries, surface bonds). Moreover, their atomic order is intermediate between that of amorphous materials (first-neighbour order) and that of crystalline materials (long-range order). Their peculiar properties are related to the size of the material building blocks, which can in principle be tuned. The new properties exhibited by nanostructured materials are due to different effects:

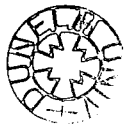

- size effects, resulting if the characteristic size of the building blocks of the nanostructure is reduced to the point where it becomes comparable to critical length scales of physical phenomena (e.g. the mean free path of electrons or phonons, a coherency length, etc.);
- change of the dimensionality of the system, so that we can have characteristic 2D or 1D phenomena;
- change of the atomic structure;
- alloying of elements.

The synthesis of materials or devices with new properties by means of controlled manipulation of their structure on the atomic level has thus become an emerging interdisciplinary field based on solid state physics, chemistry, and materials science.

When considering nanostructured materials with novel properties, one can distinguish between two groups of materials. On one hand, we have materials with reduced dimensions or dimensionality, such as nanometre-sized particles, thin wires, thin films, quantum wells. On the other hand we have bulk solids (or films) with a nanometre-scale microstructure, where the atomic arrangement or the size of building blocks forming the solid (crystallites, or atomic and molecular groups) vary over a length of a few nanometres throughout the bulk. The atomic structure and the chemical composition may vary in space continuously, such as in glasses, gels or implanted materials. However we can also have materials, assembled from nanometre-sized building blocks, which are structurally heterogeneous, i.e. nanocrystalline materials with crystallites and grain boundaries, nanoparticles embedded in a matrix, cluster-assembled materials.

One of the most famous examples of the correlation between the atomic structure and the properties of a bulk material is the variation in the hardness of carbon when passing from graphite to diamond. Size confinement also has a spectacular application in carbon, for example in the family of carbon clusters, or fullerenes, including the most famous C_{60} Buckminsterfullerene [5], or in the family of multiwall or single wall nanotubes, which can be insulating, semiconducting or conducting materials [6] depending on the atomic arrangement. Moreover, doping of these new carbon forms has been investigated, in the hope of tuning the electronic properties.

Thin films or multilayers form another type of nanostructured materials. Though structurally homogeneous, the reduced thickness strongly affects their properties, and the role of the surface becomes increasingly important. Amorphous carbon in the form

of thin films has received a huge amount of attention in the past ten years. Several applications have been found for these materials, from protective coating films, to field emission films for flat panel displays, to large area storage materials or supercapacitors (see sections 4.1 and 5.1).

There are different ways to build nanostructured systems [3, 4, 7], for example atomic deposition, mechanical milling, chemical methods and gas aggregation techniques. The main requisites of these techniques are the ability to control the properties of the deposited materials and the efficiency of the production. One of the most explored ways to grow nanostructured materials is the assembling of clusters. Clusters are intrinsically nanomaterials, objects whose dimensions provide properties completely different from the bulk. The physical and chemical properties of these objects are size-dependent and they can be considered as building blocks for the synthesis of materials with tailored properties, controlled by changing the size and composition of the primeval clusters [8]. By assembling them for example as films, one hopes that some of the peculiar properties of clusters are retained in the solid form.

The possibility of using nanostructures for the building of electronic and electro-optic devices or for the assembling of materials with novel structural properties is thus intimately related to the capability of producing and manipulating small particles with defined and homogeneous sizes. For this reason this field of research can benefit from the efforts devoted to the characterisation of clusters and small aggregates. Aggregates of atoms in the nanometre size range, usually called nanoparticles, exhibit properties which can be considered intermediate between those characterising simple molecules on one side and bulk materials on the other side. Although in recent years a considerable amount of work has been done to study these objects, the production and investigation of small particles remains a challenging problem [9]. Efforts have been concentrated on the manipulation of the optical properties of semiconductor clusters through various degrees of dimensional or quantum confinement. From this point of view the best-known systems are quantum-well structures and only very recently have quantum dots become increasingly important [2, 9].

The assembling of clusters seems to be very promising particularly for thin film synthesis [10-13]. Compared to other techniques, the use of clusters offers new opportunities such as shallow implantation, control of cluster mass distribution and control of cluster deposition energies, which can allow the growth of films with a tailored nanocrystalline structure [10, 13]. Moreover, the low diffusivity of clusters on

a substrate causes different nucleation and growth processes compared to atom-assembled films. A necessary requisite for a large scale and reliable use of this technique is the development of efficient production and characterisation methods to control cluster nucleation, deposition and coalescence [13-16]).

Two main cluster deposition methods have been historically explored. The first idea was to produce beams of accelerated (ionized) clusters and take advantage of the incident kinetic energy to enhance atomic mobility even at low substrate temperatures. This method does not lead, in general, to nanostructured materials, but to films similar to those obtained by atomic deposition, with sometimes better properties. A more recent approach is to deposit beams of neutral clusters, with low kinetic energy to preserve their peculiar properties (characteristic of the free, isolated clusters) when they reach the surface. The limit between the two methods is roughly at a kinetic energy in the range 0.1-1 eV/atom.

In particular, the application of cluster beam deposition to the synthesis of nanocrystalline carbon thin films seems to be very attractive. The control of deposition energy and mass distribution can in theory open the possibility of tuning the carbon coordination (sp^2–sp^3 ratio) in the film. Also, the introduction of fullerenic structures embedded in an amorphous matrix could influence the mechanical properties of the nanostructured materials [17, 18]. A great deal of experimental and theoretical work has been performed on carbon films grown from an atomic plasma ([19], see also Chapter 4). However the characterisation of cluster-assembled carbon materials lacks detail, despite theoretical investigations having been done on the properties of solids based on the assembly of small carbon units [20-22]. The structural and functional properties of amorphous carbon films, assembled atom by atom, are largely determined by the kinetic energy of the ions reaching the substrate during the film growth [1, 7, 8]. The use of carbon clusters, together with carbon atoms, can open new possibilities for the synthesis of materials where the structural and functional properties are also determined by the organisation of units with dimensions ranging from mesoscopic to nanoscopic scale [10, 23].

1.2 X-ray and inelastic light scattering techniques

For both nanoparticles and cluster-assembled materials, and especially for thin films, it is crucial to have diagnostic techniques allowing the characterisation of particle

structure, size distribution and of their variation during post-deposition processing. Both x-ray and inelastic light scattering have the advantage, over other techniques (i.e. electron scattering techniques), of being non-destructive, and this is very important particularly when studying thin films. Moreover, microscopy techniques (e.g. Atomic Force Microscopy) are usually limited to the study of surfaces.

Vibrational spectroscopy and in particular Raman and Brillouin spectroscopy accomplish the task of providing information about the dynamics of phonons in small particles, substructures and thin films. Since exact theories have been formulated and tested to explain the confinement effects, these techniques, and in particular Raman spectroscopy, can also be used as particle size and nanostructure characterisation tools.

The first works on the use of Raman scattering for the study of confinement effects have been published more than 20 years ago. Since then this technique has become a routine approach to the characterisation of small particle systems (e.g. study of particle size distribution). Raman scattering is now widely accepted as a standard characterisation technique for the study of amorphous carbons, and can provide information about the local bonding in these materials.

On the other hand Brillouin spectroscopy is a very sensitive technique for the detection of acoustic modes, and if applied to supported thin films or multilayers it can provide useful information on their elastic properties. It can also be used to study disorder effects on the vibrational properties (e.g. in surface or volume fractal-like aggregates, or induced by the roughness). Vibrational characterisation of materials presenting multiscale granularity such as cluster-assembled carbon films is still poorly developed.

Systems with a characteristic size ranging from a few nanometers to several tens of nanometers can be investigated with vibrational spectroscopy. Beyond these limits several problems remain. The structure of particles with size below a few nanometres is poorly known and difficult to describe theoretically. The assumptions made for the crystalline state are no longer valid. This implies the exploration of an ill-defined region where high structural disorder typical of amorphous solids coexists with features typical of nanocrystalline materials, leading to different contributions to the modification of the phonon spectra. This situation is particularly relevant and is often underestimated for disordered carbons. In these systems the presence of different scales of disorder and the coexistence of different allotropic forms confuses the interpretation of vibrational scattering from carbon. A similar situation can be found at the other

extreme of mesoscopic systems for scales of tens and hundreds of nanometres. These are lengths typical of acoustic phonons visible by means of Brillouin spectroscopy.

X-ray scattering techniques are also widely used for structural characterisations. These include X-Ray Diffraction (XRD) for crystalline order investigation (it can also provide size information in the case of small particles), Wide Angle X-ray Scattering (WAXS) for radial distribution function determination in amorphous materials, Small Angle X-ray Scattering (SAXS) for obtaining structural information over a wider range of lengths (e.g. fractal or self-affine aggregation properties, radius of gyration of small particles), and X-Ray Reflectivity (XRR) for the determination of density, roughness and layering in thin films or multilayers. In particular, grazing incidence x-ray scattering is very powerful for the investigation of thin films. The grazing incidence geometry increases the x-ray path in the film, and minimises the probing of the substrate (in particular if the incidence angle is close to the critical angle of total external reflection of the film). This enhances the useful signal, from the thin film, that can be detected. Moreover, by changing the incidence angle it is possible to tune the x-ray penetration depth and thus probe thin films at different depths. This allows, for example, the study of buried interfaces.

By combining inelastic light scattering and x-ray techniques a considerable amount of information can be gathered concerning the vibrational and structural properties of nanostructured materials. For example, XRR can be used to perform the structural characterisation needed for the thin film geometry modelling to be used in the analysis of Brillouin data (layering, thickness, density). XRD can be employed for particle size determination and crystalline order characterisation, indispensable in the interpretation of Raman or low-frequency Raman spectra of nanosystems. In the case of nanocrystalline or amorphous materials (e.g. carbon) WAXS can help in interpreting the Raman data (e.g. providing information about the presence and size of ordered domains), while SAXS can be coupled with low-frequency inelastic light measurements to study the possible existence of dynamical or static self-affine properties of the system.

In summary, not only can these techniques be combined to access complementary information, but also the results of one experiment can help provide the necessary input needed for the modelling, analysis and interpretation of the data obtained using a different experimental technique.

1.3 Aim of this thesis

The subject of this thesis has been the study of different nanostructured materials, and in particular of thin films, using different techniques involving the scattering of electromagnetic radiation. Light scattering (with wavelength of the excitation light in the visible range) and different x-ray scattering techniques (x-ray reflectivity, x-ray diffraction, small and wide-angle x-ray scattering, from laboratory and synchrotron sources) have been employed, together with other characterisation techniques. In collaboration with several research groups we have obtained structural and dynamical information relevant to the study of both the properties and the deposition processes of the materials investigated.

While inelastic light scattering provided information about the dynamical behaviour, only elastic x-ray scattering has been employed. Due to the smaller wavelength, x-ray scattering is more sensitive to the local ordering of atoms, and has been used to clarify aspects of the static structure of the materials under investigation.

The experiments undertaken must be interpreted in the wider framework of a research project funded by the Italian National Institute for Condensed Matter Physics (INFM) and involving the partnership of the University of Milan, Politecnico di Milano, University of Durham, and other European and Italian research groups. The aim of the project was the design, construction and characterisation of a Pulsed Microplasma Cluster Source (PMCS), and the deposition and characterisation of cluster-assembled carbon films with tailored nanostructural properties. Many different characterisation techniques have been employed (as explained in chapter 5), and the work here presented is only a contribution to the whole research project. The control of the carbon film nanostructure can open interesting perspectives for the application of these systems for field emission, catalysis, and gas adsorption. In particular, due to the interest in the field emitting properties of nanostructured carbon films, a collaborative project with J. Robertson's group at the University of Cambridge, leader in the production and study of "atom by atom" assembled amorphous carbon films (from an atomic plasma), was started. Moreover, the possibility of using Brillouin scattering to determine the mechanical properties of tetrahedral amorphous carbon films (ta-C) grown in Cambridge strengthened this link. It was within the framework of this collaboration that the XRR study of density and layering properties of ta-C films was carried out.

The study of melting of tin nanoparticles as a function of their size was not directly related to the above-mentioned projects. This work was undertaken in collaboration with the University of Nice (sample growth) and the University of Pavia (optical characterisation). It proved to be an interesting example of the combined use of x-ray and inelastic light scattering techniques.

1.4 Thesis outline

In chapter 2 the theory behind the experimental techniques employed in this thesis is introduced. A simple classical picture and the fundamental ideas behind the quantum theory of Raman scattering are presented, and the characteristics of Raman scattering from small crystallites and amorphous materials are outlined. The theory of Brillouin scattering is then discussed, in relation to the elastic properties of materials and to the propagation of sound waves, particularly in the case of supported films. Finally the main theoretical points concerning x-ray reflectivity, diffraction, small angle scattering and wide angle scattering from amorphous materials, and related to the work here presented, are introduced.

Chapter 3 briefly describes all the experimental requirements and the instrumentation required for the experiments performed and described in this thesis, both for laboratory and synchrotron measurements. The analysis techniques and fitting or simulating software employed for data analysis are introduced.

The above-mentioned scattering techniques were able to provide a wide characterisation of the properties of the investigated materials, but attention was also given to some interesting aspects of the scattering itself, from such peculiar systems as nanostructured thin films.

In Chapter 4 it is demonstrated how, in the case of a wide variety of carbon films (both pure and hydrogen or nitrogen containing), assembled "atom by atom", with very low surface roughness, x-ray reflectivity can be usefully employed to study their density, surface roughness and internal layering. Coupled with Electron Energy Loss Spectroscopy (EELS), XRR was used to obtain a single value for the effective mass to be used in density determination by EELS, and a general relationship between density and sp^3 hybridization content was demonstrated. By coupling XRR with H effusion, we were able to determine the hydrogen content in these films.

In Chapter 5 the experimental results related to the cluster-assembled carbon films project are presented. After a brief introduction concerning the deposition technique, a section is devoted to the particular and widely studied case of Raman scattering from amorphous carbons. The study and characterisation of the films grown in the University of Milan, using Raman and Brillouin scattering and x-ray scattering techniques, is then discussed. It is shown how inertial separation effects in the cluster beam, and the possibility of focusing the beam, enable the deposition of films in which the local bonding character and also the mesoscopic structure can be tuned. Brillouin scattering permits the evaluation of the elastic properties of the material. In addition to the material characterisation, inelastic light scattering from these nanostructured systems presents interesting aspects (e.g. presence of localised, non-propagating vibrational modes).

Chapter 6 shows how a combination of high-resolution x-ray diffraction and Brillouin scattering was used to study the size-dependent melting transition in tin nanoparticles embedded in an amorphous matrix. Low frequency Raman scattering from acoustic vibrations of the particles was also studied across the melting temperature.

Finally, chapter 7 reviews the main conclusions resulting from the work presented, and discusses the possible future developments of this research.

References for Chapter 1:

[1] R.W. Siegel, Mater. Sci. Eng. B **19**, 37 (1993)

[2] A.S. Edelstein, R.C. Cammarata (edited by), "Nanomaterials: Synthesis, Properties and Applications", IOP, Bristol (1996)

[3] H. Gleiter, Acta Mater. **48**, 1 (2000)

[4] P. Jensen, Rev. Mod. Phys. **71**, 1695 (1999)

[5] P. Milani, Riv. Nuovo Cimento **19**, 1 (1996)

[6] P.M. Ajayan, T.W. Ebbesen, Reports On Progress in Physics **60**, 1025 (1997)

[7] H. Gleiter, Prog. Mater. Sci. **33**, 223 (1989)

[8] H.P. Cheng, U. Landman, Science **260**, 1304 (1993)

[9] R.F. Service, Science **271**, 920 (1996)

[10] P. Melinon, V. Paillard, V. Dupuis, A. Perez, P. Jensen, A. Hoareau, J. P. Perez, J. Tuaillon, M. Broyer, J. L. Vialle, M. Pellarin, B. Baguenard, and J. Lerme, Int. J. Mod. Phys. B **9**, 339 (1995)

[11] I. Yamada, Nucl. Instrum. Methods Phys. Res. B **112**, 242 (1996)

[12] E. Barborini, P. Piseri, P. Milani, Journal of Physics D-Applied Physics **32**, L105 (1999)

[13] P. Milani, P. Piseri, in "Application of Accelerators in Research and Industry", edited by J. L. Duggan and I. L. Morgan, AIP Conf. Proc. **392**, 495 (1997)

[14] A. Perez, P. Melinon, V. Dupuis, P. Jensen, B. Prevel, J. Tuaillon, L. Bardotti, C. Martet, M. Treilleux, M. Broyer, M. Pellarin, J.L. Vialle, B. Palpant, J. Lerme, J. Phys. D: Appl. Phys. **30**, 709 (1997)

[15] M. Ehbrecht, H. Ferkel, F. Huisken, Z. Phys. D **40**, 88 (1997)

[16] P. Milani, S. Iannotta, "Synthesis of Nanophase Materials by Cluster Beam Deposition", Springer, Berlin (1999)

[17] G.A.J. Amaratunga, M. Chowalla, C.J. Kiely, I. Alexandrou, R. Aharonov, R.M. Devenish, Nature **383**, 321 (1996)

[18] H. Sjostrom, S. Stafstrom, M. Roman, J.-F. Sundgren, Phys. Rev. Lett. **75**, 1336 (1995)

[19] D.R. McKenzie, Rep. Prog. Phys. **59**, 1611 (1996)

[20] A. Canning, G. Galli, J. Kim, Phys. Rev. Lett. **78**, 4442 (1997)

[21] D. Donadio, L. Colombo, P. Milani, G. Benedek, Phys. Rev. Lett. **83**, 776 (1999)

[22] G. Benedek, L. Colombo, Mater. Sci. Forum **232**, 247 (1996)

[23] E. Barborini, P. Piseri, A. Li Bassi, A.C. Ferrari, C.E. Bottani, P. Milani, Chem. Phys. Lett. **300**, 633 (1999)

Chapter 2

Experimental techniques: fundamental physics

2.1 Introduction

The results presented in this thesis were obtained using different techniques, which can be divided in two groups, i.e. inelastic light scattering and x-ray scattering. Raman scattering and Brillouin scattering fall into the first category; x-ray diffraction (XRD), small and wide angle x-ray scattering (SAXS and WAXS) and x-ray reflectivity (XRR) fall into the second category. This chapter will provide an overview of the theory behind the techniques employed, with particular attention to their application to thin films and nanostructured materials.

Most of the light travelling into a medium is transmitted or absorbed according to the laws of reflection and refraction; a small fraction is diffused in all directions because of the inhomogeneities in the medium. Structural inhomogeneities are static diffusers and scatter the light elastically (without change of frequency). Density fluctuations due to atomic vibrations are dynamical diffusers, as well as charge or spin fluctuations. Inelastic light scattering by acoustic waves was first proposed by Brillouin [1]; inelastic light scattering by molecular vibrations was proposed by Raman [2]. For simplicity, we can say that (at least in a crystal) Raman scattering is inelastic light scattering from optical phonons, while Brillouin scattering is from acoustic phonons.

Grazing incidence elastic x-ray experiments are powerful, non-destructive tools enabling surface and sub-surface structures of thin films and multilayers to be explored at the Ångstrom length scale, due to the small wavelength of x-rays. While XRD and WAXS permit the study of the crystal lattice and atomic arrangement, x-ray reflectivity can provide information about thickness, density and interface roughness of layers in a film.

2.2 Raman scattering

Raman scattering is a widely used technique for the characterisation of many different materials. It can be used to investigate the vibrational dynamics of the molecules or lattice cells constituting the material, and it provides a sort of fingerprint of the molecule or crystal analysed.

Let us consider the scattering of photons with energies in the range 2-4 eV by optical phonons. When the spectrum of a crystal illuminated with monochromatic light of frequency ω_L is analysed, it is found that it consists of a very strong line at frequency ω_L, as well as weaker lines with frequencies $\omega_L \pm \omega_j(\mathbf{q})$, where $\omega_j(\mathbf{q})$ are phonon frequencies. The strong line centred at ω_L is due to the elastic scattering of photons and is known as Rayleigh scattering. The other lines originate from inelastic scattering of photons by phonons and constitute the Raman spectrum. The Raman bands at frequencies $\omega_L - \omega_j(\mathbf{q})$ are called *Stokes* lines, those at frequencies $\omega_L + \omega_j(\mathbf{q})$ are known as *anti-Stokes* lines. The intensities of the anti-Stokes lines are usually considerably weaker than those of the Stokes lines. In first order Raman scattering only optical phonons with $\mathbf{q} \cong \mathbf{0}$ are involved, as a consequence of momentum conservation.

A brief overview of Raman scattering theory is presented here; the reader is referred to ref. [2-7] for a more complete discussion of Raman scattering.

2.2.1 Classical theory

The classical theory of the Raman effect [4] is based on the fact that the incident electromagnetic field induces in the system a time-dependent dipole moment $\mathbf{M}(t)$. The intensity of the scattering field is proportional to $\left|\ddot{\mathbf{M}}(t)\right|$. The relationship between $\mathbf{E}(t) = \mathbf{E}_L(\mathbf{k}_L,\omega_L)\cos(\mathbf{k}_L\cdot\mathbf{r}-\omega_L t)$ and $\mathbf{M}(t)$ is expressed through the electronic polarizability tensor α and higher order factors:

$$\mathbf{M} = \alpha\mathbf{E} + \frac{1}{2}\beta\mathbf{E}^2 + \ldots \qquad (2.1)$$

α is a function of the electronic charge distribution and is thus sensitive to molecular vibrations. For small displacements with respect to the equilibrium position, it is possible to express α using a Taylor series as a function of the normal coordinates Q associated with the phonon $(\mathbf{q}, \omega_0)$, [i.e. $Q = Q_0 \cos(\mathbf{q}\cdot\mathbf{r} - \omega_0 t)$]:

$$\alpha = \alpha_0 + \left(\frac{\partial \alpha}{\partial Q}\right)_0 Q + \frac{1}{2}\left(\frac{\partial^2 \alpha}{\partial Q^2}\right)_0 Q^2 + \ldots \tag{2.2}$$

Let us consider the first order effect. From Eqs. (2.1) and (2.2) we have

$$\begin{aligned} &\mathbf{M}(t) = \alpha_0 \mathbf{E}_L \cos(\mathbf{k}_L \cdot \mathbf{r} - \omega_L t) + \\ &\frac{1}{2}\left(\frac{\partial \alpha}{\partial Q}\right)_0 Q_0 \mathbf{E}_L \begin{bmatrix} \cos((\mathbf{k}_L - \mathbf{q}) \cdot \mathbf{r} - (\omega_L - \omega_0)t) + \\ \cos((\mathbf{k}_L + \mathbf{q}) \cdot \mathbf{r} - (\omega_L + \omega_0)t) \end{bmatrix} + \ldots \end{aligned} \tag{2.3}$$

The scattered intensity per solid angle unit is proportional to the second derivative of the dipole moment and can be expressed as

$$I(t) \propto \mathbf{E}_L^2 \begin{bmatrix} k_0^2 \cos(\mathbf{k}_L \cdot \mathbf{r} - \omega_L t) + \\ k_1^2 \cos((\mathbf{k}_L - \mathbf{q}) \cdot \mathbf{r} - (\omega_L - \omega_0)t) + \\ k_2^2 \cos((\mathbf{k}_L + \mathbf{q}) \cdot \mathbf{r} - (\omega_L + \omega_0)t) \end{bmatrix} + \ldots \tag{2.4}$$

where

$$\begin{aligned} k_0^2 &= \alpha_0 \omega_L^4 \\ k_1^2 &= \frac{1}{4}\left(\frac{\partial^2 \alpha}{\partial Q^2}\right)_0 Q_0^2 (\omega_L - \omega_0)^4 \\ k_2^2 &= \frac{1}{4}\left(\frac{\partial^2 \alpha}{\partial Q^2}\right)_0 Q_0^2 (\omega_L + \omega_0)^4 \end{aligned} \tag{2.5}$$

From Eq. (2.4) (or calculating the corresponding power spectrum) one can see the presence of the elastically scattered component and of the inelastic Stokes and anti-Stokes components. Thus the classical theory exactly predicts the positions of the peaks in the Raman spectrum, but not the correct intensity ratio between the Stokes and anti-Stokes branches. From Eq. (2.5) one obtains:

$$\frac{I_{Stokes}}{I_{anti-Stokes}} = \frac{(\omega_L - \omega_0)^4}{(\omega_L + \omega_0)^4} \tag{2.6}$$

while experimentally it is found that the Stokes component has a larger intensity. Most of the light is elastically scattered (Rayleigh scattering). The frequency difference between incident and scattered light is called the Raman frequency or Raman shift. More phonons can be involved in the scattering process, thus contributing to the so-called second order Raman scattering. Usually, the unit used to express the Raman shift is wavenumber, expressed in cm^{-1} ($1\ cm^{-1} \equiv 30\ GHz \equiv 1.2407 \cdot 10^{-4}\ eV$).

2.2.2 Quantum theory

The quantum theory of Raman scattering is rather complicated (see [5]). Only a very simple picture of the photon-phonon interaction will therefore be given.

Let (ω_L, $\mathbf{k}_L$) be the photon in the laser beam, (ω_{sc}, $\mathbf{k}_{sc}$) the scattered photon and (ω_j, $\mathbf{q}$) the optical phonon involved in the scattering process. Energy and momentum are conserved between initial and final states. For the Rayleigh scattering:

$$\begin{aligned} \omega_L &= \omega_{sc} \\ \mathbf{k}_L &= \mathbf{k}_{sc} \end{aligned} \tag{2.7}$$

while for Raman scattering

$$\begin{aligned} \omega_L &= \omega_{sc} \pm \omega_j(\mathbf{q}) \\ \mathbf{k}_L &= \mathbf{k}_{sc} \pm \mathbf{q} \end{aligned} \tag{2.8}$$

Under usual experimental circumstances, $\omega_L >> \omega_j(\mathbf{q})$, so that $\omega_L \cong \omega_{sc}$ (typical values are $\omega_L \cong 20000$ cm^{-1} and $\omega_j \cong 1000$ cm^{-1}). At these incident frequencies there is little dispersion, so that $n(\omega_L) = n(\omega_{sc}) = n$. $\mathbf{k}_L$ and $\mathbf{k}_{sc}$ are the wavevectors inside the crystal, and so $|\mathbf{k}_L| = n(\omega_L)\omega_L/c \cong n(\omega_{sc})\omega_{sc}/c = |\mathbf{k}_{sc}|$. $\mathbf{k}_L$ and $\mathbf{k}_{sc}$ are much smaller than the Brillouin zone-edge wavector, and also $\mathbf{q}$ is very small. From here one can deduce the fundamental selection rule $\mathbf{q} \cong \mathbf{0}$, that is, in first order Raman scattering only the optical phonons at the centre of the Brillouin zone can be excited. Moreover, in crystals other selection rules exist due to the symmetries of the unit cell (see below).

A simple picture of the scattering process is given in fig. 2.1, where the virtual state is introduced only to model the scattering process and the perturbative process due to the photon; "absorption" of photon $\hbar\omega_L$ and "emission" of photon $\hbar\omega_{sc}$ are simultaneous; this is not an absorption process.

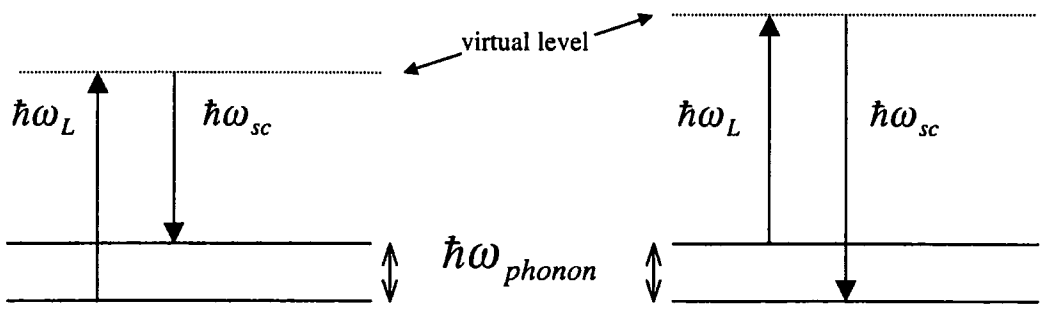

Fig. 2.1: Schematic representation of Stokes (left) and anti-Stokes (right) scattering. If the excitation energy $\hbar\omega_L$ is close to an electronic transition, resonance enhanced Raman scattering is possible.

If the frequency of the incident radiation is close to the energy of an electronic transition, Raman intensity is strongly enhanced; the subsequent scattering phenomenon is called resonant Raman scattering.

The simple quantum model here described accounts for the higher intensity of the Stokes lines with respect to the anti-Stokes lines. In fact the population in the ground vibrational state is much higher than that of the excited states, and taking into account that the states are populated according to Bose-Einstein statistics, one can obtain

$$\frac{I_{Stokes}}{I_{anti-Stokes}} = \frac{(\omega_L - \omega_j(\mathbf{q}))^4}{(\omega_L + \omega_j(\mathbf{q}))^4} \exp\left(\frac{\hbar\omega_j(\mathbf{q})}{k_B T}\right) \tag{2.9}$$

This ratio is always greater than one. The exponential factor is obtained only in the quantum theory, not in the classical one.

Second order Raman scattering is a phenomenon involving two phonons at the same time. Without entering in details, we can say that selection rules are the same but take into account an interaction between two phonons and a photon:

$$\begin{aligned} \mathbf{k}_L &= \mathbf{k}_{sc} \pm \mathbf{q}' \pm \mathbf{q}'' \\ \omega_L &= \omega_{sc} \pm \omega_1(\mathbf{q}') \pm \omega_2(\mathbf{q}'') \end{aligned} \tag{2.10}$$

Frequencies observed in second order Raman spectra can be a combination (sum) of two phonon frequencies ($\omega_1+\omega_2$), an overtone (that is a combination of two phonons with the same frequency), or a difference ($\omega_1-\omega_2$). Now, since $|\mathbf{k}_L| \approx |\mathbf{k}_{sc}|$, it must be $\pm \mathbf{q}' \pm \mathbf{q}'' \approx \mathbf{0}$. This means that the two phonons can now be from the entire Brillouin zone, provided that the vector sum of their wavevectors is close to zero.

2.2.3 Raman tensor and selection rules

When thermal fluctuations exist in the material the polarizability tensor can be written as $\alpha = \alpha_0 + \delta\alpha_s$ (see Eq. (2.2)). $\delta\alpha_s$ contains the fluctuations of the normal mode Q_s, and this mode is Raman-active only if at least one of the components of $\delta\alpha_s$ is different from zero.

Thus selection rules arise which depend on the symmetry of the equilibrium configuration and of the vibrational mode (see [4]).

2.2.4 Raman scattering from small crystalline domains and amorphous materials

Conservation of momentum and the subsequent selection rule for the Raman scattering ($\mathbf{q} \cong \mathbf{0}$) strictly hold only in an infinite perfect crystal. In a finite size domain the phonon cannot be described by a plane wave, but by a wave packet with spatial extension of the order of the domain size; this introduces a momentum indetermination.

Let us consider Heisenberg's uncertainty principle:

$$\Delta p \Delta x \geq h \tag{2.11}$$

For a phonon $\Delta p = \hbar \Delta q$ and being $\Delta x = d$ the crystal domain size, one obtains

$$\Delta q \geq \frac{2\pi}{d}. \tag{2.12}$$

The smaller the crystal size, the greater the wave vector uncertainty; for very small crystal sizes nearly all the phonons in the first Brillouin zone can participate in the scattering event. This phenomenon is known as phonon confinement. Nemanich, Solin and Martin [8] showed that the Raman scattering intensity of a finite crystal is given by

$$I(\omega) = \frac{n(\omega)+1}{\omega} \sum_{\mathbf{q},j} C(\mathbf{q},\omega_j(\mathbf{q}))\left|F(\mathbf{q})\right|^2 \frac{\Gamma/2\pi}{[\omega - \omega_j(\mathbf{q})]^2 + \Gamma^2/4} \tag{2.13}$$

where $n(\omega)$ is the boson occupation factor, Γ is the phonon lifetime broadening, $C(\mathbf{q},\omega_j(\mathbf{q}))$ is the Raman coupling coefficient for a phonon of wavevector $\mathbf{q}$, branch j and dispersion relation $\omega_j(\mathbf{q})$, and $|F(\mathbf{q})|^2$ is the wavevector uncertainty of the phonons involved in the light scattering (see also [9-12]). Introducing a greater number of defects so that the crystallites become smaller and smaller, and the material becomes amorphous, Shuker and Gammon [13] derived a formula for Raman scattering by amorphous materials:

$$I(\omega) = \frac{n(\omega)+1}{\omega} C(\omega) G(\omega) \tag{2.14}$$

where $n(\omega)$ is the boson occupation factor, $G(\omega)$ is the Phonon Density Of States (PDOS) of the disordered material (usually rather different from that of the crystal of origin) and $C(\omega)$ is a coupling coefficient, often unknown and often neglected.

2.3 Brillouin scattering

Brillouin light scattering is the inelastic scattering of an incident optical wave field by thermally excited elastic waves (usually called acoustic phonons). Since the advent of lasers Brillouin scattering has received considerable interest for the characterisation of elastic and optoelastic bulk and surface properties of materials.

From an empirical point of view, the two types of scattering (Raman and Brillouin) differ only in the distinction that optical phonons are involved in Raman scattering and acoustic modes are involved in Brillouin scattering. In both phenomena, the intensity of the scattered radiation depends on the change in the electronic polarizability (or susceptibility) of the crystal induced by the phonons.

If the wave vector $\mathbf{q}$ of an acoustic mode is exactly zero we are dealing with rigid displacements of the entire crystal lattice. Such displacements lead to no change in the polarizability and so do not contribute to Brillouin scattering. It is therefore necessary to consider small but nonzero wavevectors $\mathbf{q}$, which correspond to sound waves.

Due to the small frequencies of acoustic phonons for small $\mathbf{q}$ vectors, the Brillouin lines are separated by small frequency shifts, of the order of less than 1 cm^{-1}, from the Rayleigh line. For this reason it is not possible to use a grating monochromator as for Raman scattering, but rather a Fabry-Perot interferometer must be used (see chapter 3).

In terms of corpuscular theory of light, first order Brillouin scattering corresponds to an inelastic collision of a photon (ω_L, $\mathbf{k}_L$) with an acoustic phonon (ω_j, $\mathbf{q}$). As for Raman scattering, the photon either loses a quantum of vibrational energy (Stokes line) or acquires such a quantum (anti-Stokes line). The conservation of energy and momentum are the same as in Raman scattering. For a complete presentation of Brillouin scattering theory the reader is referred to refs. [1, 3, 4, 5, 14-20].

2.3.1 Phonon-photon interaction kinematics

We assume that the incident wave is already travelling inside an isotropic medium, thus disregarding problems related to refraction and reflection of electromagnetic waves at the boundary. Let us assume that a single thermal elastic wave (acoustic phonon) is propagating within the medium with wavevector $\mathbf{q}$ and frequency $\omega_j(\mathbf{q})$. This wave sets up a modulation in the dielectric constant ε, which is viewed as a moving diffraction grating by an incident light wave. Then Brillouin

scattering can be explained by the familiar concepts of Bragg reflection and Doppler shift; conservation of total momentum and energy must be obeyed:

$$\begin{aligned} \omega_{sc} &= \omega_L \pm \omega_j(\mathbf{q}) \\ \mathbf{k}_{sc} &= \mathbf{k}_L \pm \mathbf{q} \end{aligned} \tag{2.15}$$

for *anti-Stokes* (annihilation of a phonon) and *Stokes* (creation of a phonon) events respectively. The phonon wavevector ($\approx 10^5$ cm^{-1}) is much smaller than the dimension of the Brillouin zone ($\approx 10^8$ cm^{-1}), so information is provided only about phonons near the centre of the Brillouin zone ($\mathbf{q} \approx \mathbf{0}$). In this region the dispersion relation is linear for acoustic phonons:

$$\omega(\mathbf{q}) = \mathrm{v}|\mathbf{q}| \tag{2.16}$$

where v is the velocity of sound. Using Eqs. (2.15) and the dispersion relation for photons $\omega_L = (c/n)|\mathbf{k}_L|$ and $\omega_{sc} = (c/n)|\mathbf{k}_{sc}|$, we have

$$\frac{|\mathbf{k}_{sc}| - |\mathbf{k}_L|}{n|\mathbf{q}|} = \frac{\mathrm{v}}{c}; \tag{2.17}$$

v/c is typically $\approx 10^{-5}$ so that $|\mathbf{k}_{sc}| \approx |\mathbf{k}_L| = k$. Thus we can write

$$|\mathbf{q}| = \frac{2\pi}{\lambda_{ph}} = 2k\sin(\phi/2) \tag{2.18}$$

where ϕ is the scattering angle and λ_{ph} is the wavelength of the scattering phonon. In backscattering $\phi = \pi$ and so

$$|\mathbf{q}| = 2k = \frac{4\pi}{\lambda_L} = \frac{4\pi}{\lambda_0} n \tag{2.19}$$

where n is the refractive index and $\lambda_L = \lambda_0/n$ (λ_0 is the photon wavelength in vacuum). The measurement of the Brillouin shift $\nu_{BS} = \Delta\omega/2\pi = |\omega_{sc}-\omega_L|/2\pi$ leads to the possibility of measuring the sound velocity by the following formula:

$$\mathrm{v} = \frac{\lambda_0|\Delta\omega|}{4\pi n\sin(\phi/2)} = \frac{\lambda_0 \nu_{BS}}{2n\sin(\phi/2)} \tag{2.20}$$

In backscattering $\phi = \pi$ and so

$$\mathrm{v} = \frac{\lambda_0|\Delta\omega|}{4\pi n} = \frac{\lambda_0 \nu_{BS}}{2n} \quad . \tag{2.21}$$

2.3.2 Elastic properties of materials

It is useful to define here some elastic quantities that will be used throughout the thesis (see [21]). In an elastic medium the displacement vector field $\mathbf{u}(\mathbf{r},t)$ is related to the stress tensor $\sigma_{\alpha\beta}(\mathbf{r},t)$ by the generalized Hooke's law:

$$\sigma_{\alpha\beta} = \sum_{\gamma\delta} C_{\alpha\beta\gamma\delta} \frac{\partial u_\gamma}{\partial x_\delta} \tag{2.22}$$

The strain tensor is defined as

$$\eta_{\gamma\delta} = \frac{1}{2}\left(\frac{\partial u_\gamma}{\partial x_\delta} + \frac{\partial u_\delta}{\partial x_\gamma} \right) \tag{2.23}$$

Both the stress tensor and the strain tensor are symmetric, and it can be shown that the elastic constants $C_{\alpha\beta\gamma\delta}$ can be identified by two indexes only (m and n) according to the following table:

$C_{\alpha\beta\gamma\delta} \longrightarrow C_{mn}$

$\alpha\beta \longrightarrow m$		$\gamma\delta \longrightarrow n$	
11	1	23,32	4
22	2	13,31	5
33	3	12,21	6

For an isotropic medium the elastic constant matrix reduces to

$$\begin{bmatrix} C_{11} & C_{12} & C_{12} & 0 & 0 & 0 \\ C_{11} & C_{11} & C_{12} & 0 & 0 & 0 \\ C_{12} & C_{12} & C_{11} & 0 & 0 & 0 \\ 0 & 0 & 0 & C_{44} & 0 & 0 \\ 0 & 0 & 0 & 0 & C_{44} & 0 \\ 0 & 0 & 0 & 0 & 0 & C_{44} \end{bmatrix}$$

with only two independent constants since $C_{12} = C_{11}\text{-}2C_{44}$. For an easy interpretation of the elastic constants, the elastic moduli E, G and B are introduced by the following relationships:

$$\begin{aligned} \eta_{kk} &= \frac{1}{E}\sigma_{kk} - \frac{\nu}{E}(\sigma_{jl}\delta_{jl}), \quad j,l \neq k \\ \eta_{jk} &= \frac{1}{2G}\sigma_{jk} \\ B &= -V\frac{dp}{dV} \end{aligned} \tag{2.24}$$

where δ_{jl} is the Kronecker symbol, V is the volume and p the pressure. E is the Young modulus, B is the bulk modulus, G (or μ) is the shear modulus and ν is the Poisson ratio. Since there are only 2 independent constants, the following relationships hold:

$$\begin{aligned} E &= \frac{3C_{11} - 4C_{44}}{C_{11} - C_{44}} C_{44} \\ G &= \mu = C_{44} \\ \nu &= \frac{C_{11} - 2C_{44}}{2(C_{11} - C_{44})} = \frac{C_{12}}{C_{11} + C_{12}} \\ B &= C_{11} - \frac{4}{3} C_{44} \end{aligned} \tag{2.25}$$

2.3.3 Elasto-optic coupling

The electric field of the incident light induces a polarization that depends on the position and polarizability of the atoms of the equilibrium-state crystal. This property of the material is described by the dielectric susceptibility tensor χ which relates the electric field **E** to the polarization vector **P**, or similarly by the dielectric constant tensor ε, which relates **E** to the induction vector **D**. The propagation of an acoustic wave induces a displacement of atoms from their equilibrium positions, and so we must introduce a term $\delta\varepsilon$ in the expression of the dielectric tensor. In a Born approximation description, that is a first order perturbative theory, the fluctuation of the polarization is induced only by the incident field, and not by the induced secondary field. We can write

$$\varepsilon_{\alpha\beta}(\mathbf{r},t) = \varepsilon^0_{\alpha\beta} + \delta\varepsilon_{\alpha\beta}(\mathbf{r},t) \tag{2.26}$$

where ε^0 is the tensor when no vibrations are present in the medium. The relationship between the fluctuating part of the dielectric constant and the strain tensor η in the material is governed by the elasto-optic (or Pockels) coefficients $k_{\alpha\beta\gamma\delta}$:

$$\delta\varepsilon_{\alpha\beta}(\mathbf{r},t) = k_{\alpha\beta\gamma\delta}\eta_{\gamma\delta}(\mathbf{r},t) \tag{2.27}$$

The elasto-optic coefficients represent the possibility of the material to be polarized as a consequence of a deformation of its structure. In an isotropic medium the indices of the elasto-optic tensor can be contracted in the same way as for the elastic constants (section 2.3.2), with $k_{44} = (k_{11}\text{-}k_{12})/2$.

2.3.4 Theory of Brillouin scattering cross section

To understand the intensity of the scattered wave and hence the form of a spectrum, one must be able to describe the strength of the interaction between photons and phonons. Selection rules arise in connection with the scattering angle, the polarizations of both photons and phonons, and their relative orientations with respect to the scattering plane. In a Brillouin scattering experiment one measures the power spectrum of a polarization component of the scattered field E^S:

$$S_{E^S}(\omega) = \int_{-\infty}^{+\infty} \left\langle E^S(t+\tau) E^S(t)^* \right\rangle_{th} e^{i\omega\tau} d\tau \tag{2.28}$$

where $\langle\rangle_{th}$ indicates the thermal average. The scattered electric field can be computed by means of first-order perturbation theory (Born approximation).

The expression for the scattered electric field [16, 20] in the far-field approximation [22], appropriate for most Brillouin scattering experiments, is

$$\mathbf{E}^S(\mathbf{r},t) \approx \mathrm{Re}\left\{ -\frac{E_0 e^{i(\mathbf{k}_{sc}\cdot\mathbf{r}-\omega_{sc}t)}}{4\pi\varepsilon r} \mathbf{k}_{sc} \times (\mathbf{k}_{sc} \times \mathbf{G}) \right\} \tag{2.29}$$

The components of the vector **G** (scattering integral) are given by the following expression

$$G_i = \int_V (\delta\varepsilon_{ij} e_j) e^{-i(\mathbf{Q}\cdot\mathbf{r}')} d\mathbf{r}' \tag{2.30}$$

The transferred wavevector **Q** is defined as $\mathbf{Q} = \mathbf{k}_{sc}\text{-}\mathbf{k}_L$; e_j are the components of the polarization vector of the electromagnetic wave. In a medium that is elastically and optically isotropic, Eq. (2.27) is simplified and the elasto-optic tensor reduces to two components:

$$\delta\varepsilon_{ij} = a_1 \eta_{ij} + a_2 \eta_{ll} \delta_{ij} \tag{2.31}$$

where δ_{ij} is the Kronecker symbol and $a_1 = k_{11}\text{-}k_{12}$, $a_2 = k_{12}$. The spatial part of the displacement vector can be written as $\mathbf{u} = \mathrm{Re}\left\{\mathbf{u}^0 e^{i\mathbf{q}\cdot\mathbf{r}}\right\}$. Under this assumption the scattering integral becomes

$$\mathbf{G} = \mathbf{g} \int_V e^{-i(\mathbf{Q}-\mathbf{q})\cdot\mathbf{r}'} d\mathbf{r}' \tag{2.32}$$

where

$$g_i = i[(a_1/2)(u_i^0 q_k + u_k^0 q_i) + a_2 u_l^0 q_l \delta_{ik}] e_k \tag{2.33}$$

Integrating over a volume $V >> |\mathbf{q}|^{-3}$ we finally obtain

$$\int_V e^{-i(\mathbf{Q}-\mathbf{q})\cdot\mathbf{r}'} d\mathbf{r}' \propto \delta(\mathbb{Q}-\mathbb{q}) \qquad (2.34)$$

which shows that scattering is possible only if wavevector conservation is satisfied. From the previous equations it is now possible to give some general selection rules:

- light scattered by transverse phonons is completely depolarized, i.e. it does not conserve the polarization of the incident wave;
- there is no scattering by transverse phonons polarized in the scattering plane;
- the intensity of scattering from transverse phonons goes to zero in backscattering (in elastically isotropic materials);
- scattering by longitudinal phonons is fully polarized.

2.3.5 Surface acoustic phonons

In 1887 Lord Rayleigh [23] proposed the existence of surface acoustic waves travelling in a semi-infinite medium. Since then many studies [14, 17, 19, 20, 24-27] have analysed this problem and shown that many kinds of surface waves can exist in semi-infinite media, or in thin films, free or supported (i.e. on a substrate), or in multilayers.

When a thin film is considered, acoustic surface and bulk waves propagate in the total "film plus substrate" system. The theory of elasticity enables one to calculate the modes propagating in such a system and their dispersion relations, which usually represent the velocity of the mode as a function of $q_{||}h$, where $q_{||}$ is the phonon wavevector component parallel to the surface, usually fixed in a Brillouin scattering experiment and determined by the incidence angle (see below), and h is the film thickness. The calculation can be very complicated, depending on the system geometry, and often the modes and the dispersion relations have to be computed numerically. There can be many different modes (e.g. Rayleigh phonons and Sezawa phonons, which are guided waves in the film), and the vibrational spectrum can present both discrete and continuum regions. The modes can be differently polarized (shear modes, longitudinal modes, sagittal modes, i.e. polarized in the plane containing the wave direction of propagation and the surface normal direction). For the description of the possible acoustic modes in such a system we refer the reader to references [19, 20, 26, 27].

In particular, for a semi-infinite medium or a supported film (e.g. a layer on a substrate), three regimes can be distinguished depending on the value of the surface wave velocity v with respect to the substrate transverse velocity $v_t^{(s)} = \sqrt{C_{44}/\rho}$ (called the *"transverse threshold"*) and to the substrate longitudinal velocity $v_l^{(s)} = \sqrt{C_{11}/\rho}$ (called the *"longitudinal threshold"*).:

1. ***Discrete spectrum*** ($v < v_t^{(s)}$), with two subcases in the case of a supported film, depending on the transverse sound velocity in the film, $v_t^{(f)}$:
   - $v_t^{(f)} < v_t^{(s)}$. Two modes can be present, the modified Rayleigh wave ("modified" refers to the presence of the substrate below the film) and the Sezawa wave. The velocity of the first is smaller than that of the latter; the Sezawa modes can also have $v > v_t^{(s)}$, in this case they are called pseudo-Sezawa. The two modes have a dispersion relation in which v decreases as a function of $q_{||}h$;
   - $v_t^{(f)} > v_t^{(s)}$. Only the modified Rayleigh wave is present; its dispersion relation is such that v increases with increasing $q_{||}h$ (note that the Rayleigh wave is non-dispersive in the case of a semi-infinite medium);
2. ***Continuum spectrum of mixed modes*** ($v_t^{(s)} < v < v_l^{(s)}$). Here, propagating bulk transverse waves and evanescent longitudinal waves are present. These waves must be thought of as wave packets with a pronounced surface localization of the longitudinal component. A maximum can be present at about $v_l^{(s)}$, called the *modified longitudinal resonance* or *modified high frequency pseudo-surface wave*;
3. ***Continuum spectrum of bulk modes*** ($v > v_l^{(s)}$). Here, all modes are propagating bulk waves reflected by the surface.

2.3.6 Opaque Materials

In opaque materials, such as those studied in this thesis, scattering mechanisms different from those so far illustrated can exist [15, 17, 20]. Absorption reduces the active scattering volume (limited by the penetration or skin depth) and leads to non-conservation of the component of the wavevector normal to the surface. We can define the transferred wavevector as a complex quantity

$$\mathbf{Q} = Q_{\|}\hat{\mathbf{i}}_x + (Q_{\perp} - i\delta^{-1})\hat{\mathbf{i}}_z \qquad (2.35)$$

where δ^{-1} is the skin depth. Substituting in Eq. (2.32) we have

$$\mathbf{G} \propto -2\pi\delta(Q_{\|} - q_{\|})\frac{1}{\delta^{-1} - i(q_{\perp} - Q_{\perp})} \tag{2.36}$$

The component of the wavevector parallel to the surface is conserved and the scattering intensity for a volume peak is proportional to $\frac{1}{\delta^{-2} + (q_{\perp} - Q_{\perp})^2}$, i.e. its width is related to the penetration depth.

In addition to bulk phonons, scattering from surface phonons is possible. Surface acoustic phonons are completely characterized by their wavevector $\mathbf{q}_{||}$ parallel to the surface. The wavevector conservation law for surface Brillouin scattering therefore becomes

$$\mathbf{k}_{sc,||} - \mathbf{k}_{L,||} = \pm\mathbf{q}_{||} \tag{2.37}$$

where $\mathbf{k}_{sc,||}$ and $\mathbf{k}_{L,||}$ are the projection of the scattered and incident photon wavevectors parallel to the surface, respectively. For backscattering from SAWs (Surface Acoustic Waves), $\mathbf{q}_{||}$ is fixed by the angle of incidence (fig.2.2), and the SAW phase velocity v_{SAW} can be obtained by

$$v_{SAW} = \frac{(\lambda_0 / \sin\theta_i)|\Delta\omega|}{4\pi} = \frac{(\lambda_0 / \sin\theta_i)v_{BS}}{2} \tag{2.38}$$

where θ_i is the angle between the incident photon wavevector and the direction normal to the surface. With scattering from surface phonons, it is not necessary to know the index of refraction of the medium to determine the SAW phase velocity, but the angle of incidence must be known.

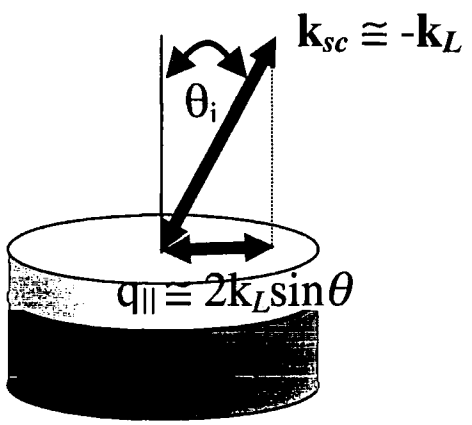

Fig. 2.2: Backscattering geometry of surface Brillouin scattering.

The spectrum of the scattered light is in general the union of a discrete and a continuum part [3, 15, 16]. In the low frequency discrete part one can detect lines associated with the true surface waves that can exist in the specific sample geometry with given elastic properties. Besides the Rayleigh wave other sagittal waves such as the Sezawa waves and the Stoneley waves (when $v_t^{(f)} \approx v_t^{(s)}$) can be observed. Furthermore, shear horizontal surface waves (Love waves) can be detected. Also the continuous high frequency part of the spectrum, beyond the transverse threshold of the substrate material, can sometimes exhibit rather defined peaks corresponding to scattering by packets of bulk (or mixed) waves with a strong surface character, such as the longitudinal resonance.

2.3.7 Ripple effect

In opaque materials the elasto-optic effect, which is a volume effect, is less important due the reduction of the active scattering volume. Nevertheless, a new scattering mechanism is possible, called the ripple effect [17, 18], which is essentially a surface effect. Surface acoustic phonons induce a modulation of the surface profile. The electromagnetic field is thus incident onto a corrugated surface that can be considered as a dynamic grating that can scatter light. The importance of this contribution to the scattered intensity depends on the surface reflectivity and is active only for shear vertical modes, i.e. with a transverse polarization perpendicular to the surface. This effect can play a role both at the film surface and at the film-substrate interface. The resulting total Brillouin scattering cross-section is the result of a coherent sum between all the scattering mechanisms, i.e. interference between ripple and elasto-optic effects is possible.

2.4 Grazing incidence x-ray reflectivity

X-ray reflectivity is a fast and non-destructive technique for the characterization of thin films, and in particular for single or multiple layers on good quality substrates. It has become a widely used technique over the past few years and the theory is well documented (see for example [28-37]).

For x-rays the refractive index in solids is slightly smaller than unity, so that total external reflection occurs at low angles of incidence. As the incidence angle θ_i increases above a critical angle θ_c, x-rays start to penetrate into the film. For x-rays the expression for the refractive index in the case of a substance with elements j (atomic number Z_j, molar masses M_j, density ρ_j) is [28]

$$n = 1 - \frac{N_A}{2\pi} r_0 \lambda^2 \sum_j \frac{\rho_j}{A_j} f_j \tag{2.39}$$

where $r_0 = e^2/4\pi\varepsilon_0 m_e c^2$ is the classical electron radius, e is the electron charge, m_e is the electron mass, N_A is the Avogadro number, c is the velocity of light, ε_0 is the dielectric permittivity of vacuum and

$$f_j = Z_j + f_j' + i f_j'' \tag{2.40}$$

takes dispersion and absorption corrections into account. Thus n can be written as:

$$n = 1 - \delta - i\beta \tag{2.41}$$

with $$\delta = \frac{N_A}{2\pi} r_0 \lambda^2 \sum_j \frac{\rho_j}{M_j} (Z_j + f_j') \tag{2.42}$$

and $$\beta = \frac{N_A}{2\pi} r_0 \lambda^2 \sum_j \frac{\rho_j}{M_j} f_j'' = \mu \frac{\lambda}{4\pi} \tag{2.43}$$

where μ is the linear absorption coefficient, given by the product of the mass attenuation coefficient and the density (e.g. μ ~2.8ρ cm^{-1} for carbon at λ=1.3926Å [38]).

From Snell's law (at the air/film interface) one can obtain the critical angle:

$$\theta_c = \sqrt{2\delta} = \lambda \sqrt{\frac{N_A r_0}{\pi} \sum_j \frac{\rho_j}{M_j} (Z_j + f_j')} \tag{2.44}$$

θ_c is usually very small, e.g. at λ=1.3926 Å it is 0.201° for Si and 0.245° for diamond (3.51 g/cm^3). From this one can infer the electron density of the material provided the wavelength is known. Corrections due to anomalous dispersion are significant near the characteristic x-ray absorption edges.

Above the critical angle x-rays begin to penetrate into the sample, and for an ideally smooth surface the reflected intensity falls off as $(2\theta)^{-4}$, as predicted by Fresnel's equations. For a real sample the fall off is more rapid, because of the surface roughness which scatters x-rays out of the specular beam [35].

If we now consider a thin layer, of refractive index n_1, deposited onto a bulk substrate, of refractive index n_2, reflections at the different interfaces will cause interference effects; in particular, there will be constructive interference when the path difference between the reflected beams is $\delta = (m+1/2)\lambda$ or $\delta = m\lambda$, where m is an integer, for $n_1 < n_2$ and $n_1 > n_2$ respectively. Snell's law can show that this happens only at certain angles of incidence

$$\theta_m^2 = \theta_c^{\,2} + \frac{\lambda^2}{4d^2}(m+1/2)^2 \quad \text{or} \quad \theta_m^2 = \theta_c^{\,2} + \frac{\lambda^2}{4d^2}m^2 \tag{2.45}$$

for $n_1 < n_2$ and $n_1 > n_2$ respectively. Here again θ_c is the critical angle at the air/film interface.

The period $\Delta\theta$ of the fringes leads to a first determination of the layer thickness, for $\theta_i >> \theta_c$:

$$d \cong \frac{\lambda}{2\Delta\theta} \tag{2.46}$$

The presence of a small surface layer of different density on the top of the film usually manifests itself in a modulation of the reflected intensity. The reflectivity curve thus presents a double periodicity, the short period corresponding to the total thickness, the long period to the thickness of the surface layer (see examples in Chapter 4). On the other hand, the reflectivity curve is less sensitive to the presence of a layer of different density at the film-substrate interface. Sometimes this situation is revealed by the presence of a beating effect, i.e. a modulation of the fringes amplitude. In the case of a multilayer (e.g. a repeated bilayer structure) the structure periodicity causes the presence of Bragg peaks in the reflectivity curve. For this situation Parrat [32] developed a recursive form of Fresnel's equations, imposing the continuity of the electric and magnetic fields across each of the interfaces of the multilayer. This leads to an expression from which the period of the superlattice may be calculated.

In a real case all the interfaces are not perfectly smooth, but there are changes in the electron density either as a result of roughness at the interfaces or as an effect of grading. This will alter the specular scatter, which is sensitive to the electron density, causing its intensity to decrease [37]. The decrease is due to phase shifts induced by the grading in the electron density normal to the surface, while surface roughness scatters x-rays out of the specular beam. To separate these effects, impossible to distinguish from a specular scan, it is necessary to model the diffuse scatter. This can also give us

information about the degree of correlated or uncorrelated roughness between the layers composing the film.

A fitting program (REFS-MERCURY, developed by Bede Scientific Instruments) has been used in this work to reproduce the experimental reflectivity data and to obtain the best model for the structural parameters of the films. Surface and interface roughness are considered within the distorted Born wave approximation (DBWA) using a Gaussian variation of the electron density gradient, so that the values obtained refer to r.m.s. roughness.

In the Born wave approximation, the attenuation of the specular scatter, caused by the presence of roughness at the interface, is included through a Debye-Waller factor

$$I_{spec} = I_0 \exp(-q_z^2 \sigma^2) \tag{2.47}$$

where q_z is the vertical component of the scattering vector and σ is the r.m.s. roughness. From conservation of energy, the diffuse intensity can be expressed as

$$I_{diff} = I_0 - I_{spec} = I_0(1 - \exp[-q_z^2 \sigma^2]) \tag{2.48}$$

The ratio of the integrated diffuse intensity to the integrated specular intensity will therefore only depend on the scattering vector and the roughness of the interface [33]:

$$\frac{I_{diff}}{I_{spec}} = \exp(q_z^2 \sigma^2) - 1 \tag{2.49}$$

Thus by measuring the integrated intensity of the diffuse and specular scatter in a transverse scan (i.e. a scan in which the detector angle, and so q_z, is fixed and the detector is scanned across the specular condition), the roughness of the surface can be deduced. This method assumes that all diffuse scatter is accessible. This is not true in general, and so this can result in an underestimation of the true roughness [30]. In the case of multiple interfaces [34] it is still possible to obtain estimates of the roughness with this method, provided that the interface roughness is highly uncorrelated (as in our case) from one interface to the other.

2.5 X-ray diffraction

High angle x-ray diffraction has been used in part of the present work to study the crystalline structure of metal nanoparticles. The position of the peaks in a 2θ (scattering

angle) representation is simply related to the distance d between the scattering planes by Bragg's law:

$$2d\sin\theta = n\lambda \tag{2.50}$$

where n is the diffraction order. The allowed values of d are related to the lattice parameters and the lattice type.

The full width at half maximum of the diffraction peaks gives a measure of the crystal domain average size via Scherrer's equation [39]:

$$D = \frac{0.94\lambda}{\Delta 2\theta \cos\theta} \tag{2.51}$$

where λ is the x-ray wavelength, D is the grain size, $\Delta 2\theta$ is the FWHM of the diffraction peak in radians and θ the Bragg angle corresponding to the peak in question.

In a standard $\theta/2\theta$ diffraction experiment, scattering is from planes parallel to the substrate. However, in our samples the crystallites were randomly oriented with respect to the substrate, and thus measurements at a fixed incidence angle were performed. Since we are dealing with thin films, very low incidence angles were chosen, in order to maximise the x-ray path within the film.

2.6 Radial distribution study of non-crystalline materials

Not all the samples studied were crystalline. The elementary formula for x-ray or neutron diffraction intensity by an assembly of atoms whether crystalline, amorphous or liquid can be written as

$$I(\mathbf{q}) \propto S(\mathbf{q})|u(\mathbf{q})|^2 \tag{2.52}$$

where $u(\mathbf{q})$ is the Fourier transform of a single atomic potential and $|\mathbf{q}| = 4\pi\sin\theta/\lambda$ is the scattering wavevector, when 2θ is the scattering angle.

The atomic form factor $|u(\mathbf{q})|^2$ is supposed to be known independently, being no more than the scattering cross section of a single atomic potential for the radiation in question. In the case of disordered materials the measurement of $I(\theta)$ can thus be interpreted as the observation of the interference function or structure factor of the material itself [39-42]:

$$S(\mathbf{q}) = \frac{1}{N}\sum_{i,j}\exp(-i\mathbf{q}\cdot(\mathbf{r}_i - \mathbf{r}_j)) \tag{2.53}$$

The basic assumption of homogeneity allows us to replace the summation over all sites with an ensemble average over site position measured relative to some standard site at $\mathbf{r} = \mathbf{0}$; this gives:

$$S(\mathbf{q}) = 1 + n\int g(\mathbf{r})\exp(-i\mathbf{q}\cdot\mathbf{r})d^3\mathbf{r} \tag{2.54}$$

where $g(\mathbf{r})$ is simply the pair distribution function and n the atomic density. A diffraction experiment can determine the pair distribution of the atoms in the sample. Normally the specimen is macroscopically isotropic so that $g(\mathbf{r})$ becomes the radial distribution function (rdf) $g(r)$, and the structure factor depends only on the modulus of $\mathbf{q}$, i.e. on the scattering angle 2θ. As $q \to 0$ the integral diverges to generate a delta-function singularity. Subtracting this singularity as the Fourier transform of unity, we obtain

$$S(q) = 1 + n\int_0^\infty h(r)\frac{\sin qr}{qr}4\pi r^2 dr \tag{2.55}$$

where $h(r)=g(r)-1$ is the total correlation function. This integral is well behaved for large r and may therefore be inverted by standard methods. This gives

$$g(r) = 1 + \frac{1}{8\pi^3 n}\int_0^\infty [S(q) - 1]\frac{\sin qr}{qr}4\pi q^2 dq\,. \tag{2.56}$$

Despite the analytical simplicity of these formulae, the Fourier inversion of an observed structure factor to give the rdf is subject to a number of practical difficulties. It is not possible to measure $S(q)$ for all q, so that errors arise from the truncation of the integral at high and low values of q [39-44].

2.7 Small angle x-ray scattering

Small angle scattering of light (SALS), x-rays (SAXS) [45-51], or neutrons (SANS) are important techniques for structural analysis of discontinuous media. Diffuse scattering arises from variations of scattering length density (neutrons), electron density (x-rays), or refractive index (light). The scattering process is characterized by an inverse relationship between feature size and scattering angle. Because of the wavelength similarity, the feature sizes studied by SANS and SAXS are similar (from 1 Å to less than 1 μm). The longer wavelength of visible light renders

SALS suitable for the study of larger structures ($\cong$ 1 μm). Many porous materials are amorphous, which often complicates data analysis in the high angle region (q > 1 Å^{-1}). In the small-angle (small-q) regime, however, disorder has proved to simplify interpretation when power-law scattering profiles are observed.

Let us consider fractal systems. One especially important characteristic of fractal systems is that many properties of these systems can often be described by quantities that are proportional to a power of another quantity. This relation is frequently called a power law. In particular, the intensity $I(q)$ of the small-angle x-ray or neutron scattering from many disordered systems has been found to be proportional to a negative power of the wavevector modulus $q = \frac{4\pi}{\lambda}\sin\theta$, where 2θ is, as usual, the scattering angle. Usually this dependence of $I(q)$ is observed only when q satisfies the condition $1/\xi_2 << q << 1/\xi_1$, where ξ_1 and ξ_2 are the characteristic (cut-off) lengths defining the range over which the structure behaves as a fractal (any real object is fractal only over a particular range of lengths).

In the discussion of the small angle scattering from fractals (see [52-58]), it is important to consider two types of fractal systems: mass fractals and surface fractals (for a definition see [53]). Mass fractals, which are often aggregates of subunits, are structures for which the mass inside a spherical surface with radius r and with its centre at a point in the mass-fractal centre is given by $M(r) \propto r^D$, where D ($D \leq 3$) is the fractal dimension. A power law of the scattered intensity characterizes mass fractal objects:

$$I(q) = I_0 q^{-D}. \qquad (2.57)$$

A surface fractal is a region with mass-fractal dimension 3, embedded in a space of euclidean dimension d=3 and bounded by a fractal surface with surface-fractal dimension D_s (where $2 \leq D_s \leq 3$). In a scattering experiment, information about the surface fractal properties can be obtained from the following power law:

$$I(q) = I_0 q^{D_s - 6}. \qquad (2.58)$$

A smooth surface yields a slope of -4 (this is Porod's law).

For non-fractal systems, theories have been developed to calculate the intensity scattered by objects with different shapes and size distributions. For dilute isolated scatterers (spheres or pores), Guinier's approximation [39, 45] applies at small q values, providing a simple characterization of the mean sphere or pore radius of

gyration R_g. The initial profile (in the range where $qR<<1$, being R the radius of the particles) decays as

$$I(q) \propto I_0 \exp\left(\frac{-R_g^2 q^2}{3}\right), \tag{2.59}$$

so that a plot of $\ln[I(q)]$ vs. q^2 has a slope proportional to R_g.

If the sample is made of interacting particles, the scattered intensity reflects both the geometry of the particles and their spatial correlations, and can be often written as

$$I(q) = P(q)S(q) \tag{2.60}$$

where $P(q)$ is the form factor of the particles and $S(q)$ the structure factor of the assembly.

References for Chapter 2:

[1] L. Brillouin, Ann. Phys. **17**, 88 (1922)

[2] C.V. Raman, K.S. Krisham, Nature **121**, 501 (1928)

[3] P. Milani, C.E. Bottani, "Vibrational Properties of Mesoscopic Structures", in "Handbook of Nanostructured Materials and Nanotechnology", Academic Press (1998)

[4] P. Bruesch, "Phonons: Theory and Experiments II", Springer-Verlag (1986)

[5] M. Cardona, in "Light Scattering in Solids, vol. I & II - Topics in Applied Physics", Springer, Berlin (1982)

[6] D.A. Long, "Raman spectroscopy", McGraw-Hill (1977)

[7] G. Placzek, "Handbuch der Radiologie", vol. VI, ed. by E. Marx, Akademische Verlagsgesellschaft, Leipzig (1934)

[8] R.J. Nemanich, S.A. Solin, R.M. Martin, Phys. Rev. B **23**, 6348 (1981)

[9] P.M. Fauchet and J.H. Campbell, Cri. Rev. Solid State Mater. Sci. **14**, S79 (1988)

[10] J. Gonzalez-Hernandez, G.H. Azerbayejani, R. Tsu and F.H. Pollak, Appl. Phys. Lett. **47**, 1350 (1985)

[11] M.I. Vasilevskiy, A.G. Rolo and M. J. M. Gomes, Solid State Comm. **104**, 381 (1997)

[12] C. E. Bottani, C. Mantini, P. Milani, M. Manfredini, A. Stella, P. Tognini, P. Cheyssac, R. Kofman, Appl. Phys. Lett. **69**, 2409 (1996)

[13] R. Shuker and R.W. Gammon, Phys. Rev. Lett. **25**, 222 (1970)

[14] I.A. Viktorov, "Rayleigh and Lamb waves", Plenum Press, New York (1967)

[15] J. R. Sandercock, "Trend in Brillouin Scattering: Studies of Opaque Materials, Supported Films and Central Modes", in "Light Scattering in Solids III", edited by M. Cardona and G. Guntherodt, Springer-Verlag, Berlin (1982)

[16] P. Mutti, C.E. Bottani, G. Ghislotti, M.G. Beghi, G.A.D. Briggs, J.R. Sandercock in "Advances in Acoustic Microscopy", Vol.1, Ed. A. Briggs, Plenum Press, New York (1995), p.249

[17] A. M. Marvin, V. Bortolani and F. Nizzoli, J. Phys. C **13**, 299 (1980)

[18] R. Loudon, J.R. Sandercock, J. Phys. C: Solid St. Phys. **13**, 2609 (1980)

[19] F. Nizzoli and J.R. Sandercock, "Surface Brillouin Scattering from Phonons", in "Dynamical Properties of Solids", edited by G. K. Norton and A. A. Maradudin, North-Holland, Amsterdam (1990)

[20] F. Nizzoli, D.L. Mills, "Light Scattering from Phonons and Spin Waves on Surfaces", in "Non linear Surface Electromagnetic Phenomena", edited by H.E. Ponath and G.I. Stageman, Elsevier Science Publishers (1991)

[21] G. Grimvall, "Thermophysical Properties of Materials", North-Holland, Amsterdam (1986)

[22] L.D. Landau, E.M. Lifshitz, "Electrodynamics of continouos media", Pergamon Press, Oxford (1970)

[23] Lord Rayleigh, London Math. Soc. Proc. **17**, 4 (1887)

[24] A.E.H. Love, "A treatise on the Mathematical Theory of Elasticity", Dover Publ., New York (1944)

[25] G.P. Srivastava, "The Physics of Phonons", Adam Hilger (1990)

[26] G. W. Farnell, "Properties of Elastic Surface Waves", in "Physical Acoustics", edited by W. P. Mason and R. N. Thurston, Academic Press, New York (1970)

[27] G. W. Farnell and E. L. Adler, "Elastic Wave Propagation in Thin Layers", in "Physical Acoustics", edited by W. P. Mason and R. N. Thurston, Academic Press, New York (1972)

[28] B. Lengeler, X-ray Absorption and Reflection in the Hard X-Ray Range, eds. M. Campagna and K.Rosei, North Holland (1990)

[29] I. Pape, Ph.D. Thesis, University of Durham (1997)

[30] I. Pape, B.K. Tanner, M. Wormington, J. Non Cryst. Solids **248**, 75 (1999)

[31] V. Holy, T. Baumbach, Phys. Rev. B **49**, (15) 10668 (1994)

[32] L.G. Parrat, Phys. Rev. **95**, 359 (1954)

[33] D.E. Savage, J. Kleiner, N. Schimke, Y.H. Phang, T. Jankowsky, J. Jacobs, R. Kariotis, M.G. Legally, J. Appl. Phys. **69**, 1411 (1991)

[34] D.E. Savage, N. Schimke, Y.H. Pang, M.G. Legally, J. Appl. Phys. **71**, 3283 (1992)

[35] M. Wormington, I. Pape, T.P.A. Hase, B.K. Tanner, and D.K. Bowen, Phil. Mag. Lett. **74**, 211 (1996)

[36] M. Wormington, C. Panaccione, K.M. Matney, D.K. Bowen, Phil. Trans. Roy. Soc. A **357**, 2827 (1999)

[37] S.K. Sinha, E.N. Sirota, S. Garoff, Phys. Rev. B **38**, 2297 (1988)

[38] B.L. Henke, E.M. Gullikson, J.C. Davis, "X-ray interactions: photoabsorption, scattering, transmission, and reflection at E=50-30000 eV, Z=1-92", Atomic Data and Nuclear Data Tables **54**, 181 (1993)

[39] A. Guinier, "X-ray diffraction in crystals, imperfect crystals and amorphous bodies", Dover Publications, New York (1944)

[40] B.E. Warren, "X-Ray Diffraction", Dover, New York (1990)

[41] J.S. Rigden, R.J. Newport, G. Bushnell-Wye, J. Mater. Res. **12**, 264 (1997)

[42] H.P. Klug, L.E. Alexander, "X-Ray Diffraction Procedures for Polycrystalline and Amorphous Materials", Wiley, New York (1974)

[43] J.K. Walters, M. Kuhn, C. Spaeth, E. Dooryhee, R.J. Newport, J. Appl. Phys. **83**, 3529 (1998)

[44] D.F.R. Mildner, J.M. Carpenter, J. Non-Cryst. Solids **47**, 391 (1982)

[45] A. Guinier, G. Fournet, "Small-Angle Scattering of X-Rays", Wiley, New York (1955)

[46] "Small angle x-ray scattering", edited by O. Glatter and O. Kratky, Academic Press (1982)

[47] W.S. Rothwell, J. Appl. Phys. **39**, 1840 (1968)

[48] J.R. Levine, J.B. Cohen, Y.W. Chung, P. Georgopoulos, J. Appl. Cryst. **22**, 528 (1989)

[49] T. Slimani, P. Goudeau, A. Naudon, G. Farges, J.L. Derep, J. Appl. Cryst. **24**, 628 (1991)

[50] A. Naudon, T. Slimani, P. Goudeau, J. Appl. Cryst. **24**, 501 (1991)

[51] A. Naudon, D. Thiaudiere, J. Appl. Cryst. **30**, 822 (1997)

[52] P.W. Schmidt, in "The Fractal Approach to Heterogeneous Chemistry", Ed. D. Avnir, John Wiley & Sons Ltd. (1989)

[53] P.W. Schmidt, J. Appl. Cryst. **24**, 414 (1991)

[54] H.D. Bale, P.W. Schmidt, Phys. Rev. Lett. **53**, 596 (1984)

[55] P. Fratzl, P. Vogl, S. Klaumunzer, J. Appl. Cryst. **24**, 588 (1991)

[56] P. Dimon, S.K. Sinha, D.A. Weitz, C.R. Safinya, G.S. Smith, W.A. Varady, H.M. Lindsay, Phys. Rev. Lett. **57**, 595 (1986)

[57] Z. Dachun, Q. Zhongkai, P. Xiaoren, JVST A **14**, 2547 (1996)

[58] Z. Yihua, Y. Qing, P. Xiaoren, R. Zhongming, H. Maoqi, Sol. State Comm. **86**, 175 (1993)

Chapter 3

Experimental apparatus and data analysis

3.1 Raman scattering

3.1.1 Experimental apparatus

Raman spectroscopy measurements were performed in the Materials Laboratory at Politecnico di Milano (Milan, Italy). Unpolarized Raman and micro-Raman spectra were recorded ex-situ, at room temperature and in back scattering geometry. An I.S.A. Jobin-Yvon T64000 triple grating spectrometer [1] and a liquid nitrogen cooled camera detection (CCD) system, frontally illuminated, were used. The excitation source was either the 514.5 nm line of an Ar ion laser or the 532 nm line of a frequency doubled Nd:YAG laser. The estimated spectral resolution was about 3 cm^{-1}.

The micro-Raman spectra were measured using a 10X, 50X or 100X objective on an Olympus microscope. Power on the sample was monitored and always kept below 1 mW in the micro-Raman configuration to avoid sample degradation.

No degradation was observed in the films studied in this thesis using the macro configuration, where 5-10 mW on the sample were used. Sample degradation of the carbon films was checked by monitoring the changes in the graphitic features of the Raman spectra while increasing the laser power on the samples.

It was possible to perform measurements in vacuum or in a controlled atmosphere (e.g. nitrogen) using an Oxford Instruments Optistat DN-V thermocryostat, where the temperature can be controlled from 80 K up to about 800 K. The vacuum, pumped by a rotary-turbomolecular pump system, can reach 10^{-6} Torr.

The triple grating spectrometer is composed of three holographic gratings (1800 lines/mm) to disperse and recombine light, as shown in fig. 3.1. The laser beam, after incidence onto the sample, passes through a slit and is then dispersed by the first grating. A second slit allows only a range of frequencies to be recombined by the second grating, before entering the final grating, which is the true spectrometer. After

the last stage the light is collected by the CCD matrix. It is possible to cover the spectral range 0-6000 cm^{-1}.

In a typical Raman spectrum, only the Stokes part, which is the most intense, is reproduced.

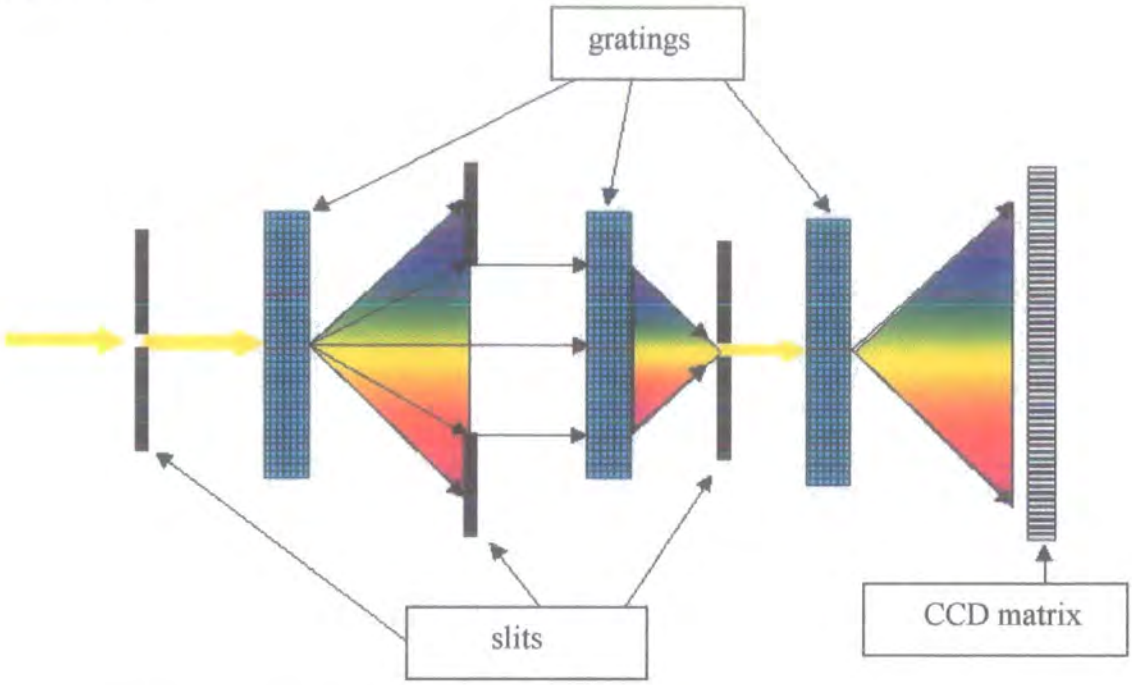

Fig. 3.1: Schematic view of the triple grating Raman spectrometer.

3.1.2 In-situ Raman scattering

The design and building of an apparatus for in-situ deposition and characterisation of cluster-assembled carbon films has been part of the work carried out in the last year. This instrument will enable Raman scattering to be recorded during the deposition of cluster-assembled carbon films by a portable source, CLARA (CLuster Assembling Roaming Apparatus), in ultra-high vacuum conditions. A schematic view of the apparatus is shown in fig. 3.2. It consists of a spherical chamber with a sample holder handled by a micromanipulator and equipped with flanges for connection with the portable source and the pumping apparatus. An optical quartz window allows entrance and collection of the laser light for the Raman measurements.

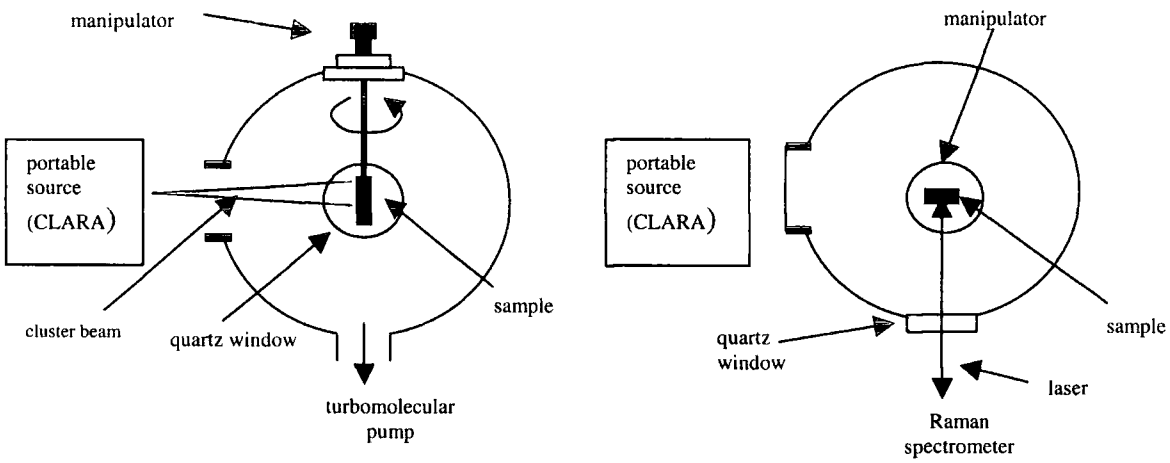

SIDE VIEW **TOP VIEW**

Fig. 3.2: Schematic view of the chamber for in-situ ultra-high vacuum Raman measurements during deposition of cluster-assembled carbon films.

3.2 Brillouin scattering

3.2.1 Experimental apparatus

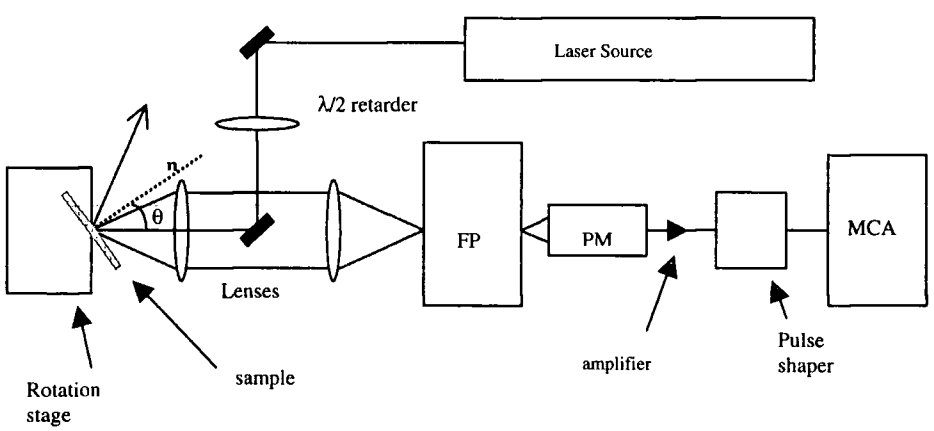

Fig. 3.3: Schematic view of the experimental apparatus for Brillouin scattering measurements.

Brillouin spectroscopy measurements were performed in the Materials Laboratory at Politecnico di Milano. The experimental apparatus for Brillouin measurements is shown in fig. 3.3. The key elements are the scattering geometry, the laser source and the high-contrast spectrometer. For the configuration adopted in our experiments we

used a backscattering geometry after reflection from a surface, suitable for opaque or semiopaque materials.

The major requirement for the laser source is a stable continuous wave operation in a single longitudinal cavity mode. We used a cw Ar^+ laser (Coherent Innova 300, wavelength 514.5 nm), where single longitudinal-mode oscillation is achieved by means of an etalon inserted into the laser cavity. A $\lambda/2$ retarder was used to select the incident polarization. The incident laser beam was directed by a small prism onto the sample surface, and was focused by a 50 mm objective lens, which was also used to collect the scattered light from the sample and direct it to the pin-hole at the entrance of the interferometer. The incident angle could be varied by a rotation of the sample in the range 0°-90°. If polarization of scattered light had to be analysed, a dichroic polarizer was inserted before the spectrograph. The laser power usually employed varied from tens to hundreds of mW.

Also for Brillouin scattering experiments it is possible to perform measurements in vacuum at different temperatures by using the Oxford Instruments Thermocryostat described in section 3.1.

The spectrometer consists of two plane parallel Fabry-Perot interferometers [2] mounted in tandem multipass configuration. Given the low intensity of Brillouin signals, single-photon counting is necessary for the detection system. We used a room temperature operated photomultiplier tube (Hamamatsu R-464 S) having less than one dark count per second. Standard electronics follow (amplifier, pulse shaper, Multi Channel Analyser).

As explained in Chapter 2, frequency shifts in a Brillouin scattering experiment are very small with respect to the laser frequency (about 1 part in 10^5). For this reason a high-resolution, high-contrast interferometer is needed. The Sandercock spectrometer is based on the use of two Fabry-Perot (FP) interferometers in a particular configuration. A FP interferometer consists of two partially reflecting plane mirrors parallel to each other at a variable distance L. For normal incidence the instrument transmits light of wavelength λ only if $L = m\lambda/2$, with m integer. Neighbouring orders of interference are separated in frequency by an amount $\Delta\nu = c/2L = 150/L$ GHz mm^{-1}. The interorder spacing is called *Free Spectral Range* (FSR).

If we take into account multiple reflections inside the interferometer cavity, the transmitted intensity is given by the Airy function [2]

$$T(L/\lambda) = \frac{T_0}{1+\left(\frac{4F^2}{\pi^2}\right)\sin^2(2\pi L/\lambda)} \qquad (3.1)$$

where T_0 is the maximum transmission and F is the *finesse* of the interferometer, which depends on the flatness and reflectivity of the mirrors and determines the width of the fringes. The resolving power of the interferometer is defined as the FWHM of the Airy function, and is

$$\delta\nu_{FWHM} = FSR/F. \qquad (3.2)$$

In our experiments $F \approx 40$. When the mirror spacing is scanned, the interferometer transmission can be tuned to analyse spectral components of the incident signal. The scanning stage [3] is mounted on top of an active vibration-isolating table. As the distance between the mirrors is scanned, these must remain parallel; a retroacted electronic system proposed by Sandercock [4], and using piezoelectric transducers, is employed for this purpose.

The contrast C of the interferometer can be defined as the ratio between maximum and minimum transmission of the Airy function: $C = 1 + (2F/\pi)^2$. F cannot be higher than 100, and so C cannot be higher than 10^4. In a multiple pass configuration

$$C_n = [1+(2F/\pi)^2]^n \qquad (3.3)$$

which can be 10^8-10^9. We used a 3+3 multipass configuration.

The use of two FP in a tandem configuration [5] enables the FSR to be increased (also the spectral resolution slightly improves, the effective finesse is >100 in our interferometer). If we choose, for the two pairs of mirrors, different distances L_1 and L_2, the transmission function is the product of the single interferometer transmission functions. The transmitted signal is a maximum only for the chosen wavelength, as the neighbouring orders are stopped by one of the two interferometers.

Brillouin spectra were usually recorded at room temperature in backscattering geometry and in *p*-depolarized polarization conditions (incident light *p*-polarized, scattered light collected without polarization analysis), unless specified differently; at several incidence angles θ_i with respect to the surface normal, in the range 10°-70°. When the substrate was Si (001), the [100] phonon propagation direction was examined, for which the analysis of the mode propagation is simpler.

By changing the distance between the mirrors, different spectral ranges from 30 GHz to 300 GHz have been adopted. The Brillouin signals on the carbon films were so low as to prevent the use of a narrow slit to limit the collection angle and increase the

resolution, except for the samples deposited on Al substrates, where a 3 mm wide slit was placed in front of the samples. The same slit was used for the measurements of the Sn nanoparticle films.

In the above θ_i range, surface phonons with wavevector (parallel to the surface) $q_{//} = \frac{4\pi}{\lambda}\sin\theta_i$ can be detected. In every spectrum a central peak, whose width is of the order of some GHz, is always present, and corresponds to the elastically scattered light.

3.2.2 Analysis software

In the Material Laboratory at Politecnico di Milano a software program has been developed [6] in order to calculate the theoretical Brillouin cross-section for a system consisting of a substrate and an arbitrary number of layers in the film. The software can compute the properties of acoustic waves travelling in the assigned geometry (dispersion relations, propagation, polarization). Provided that the density, the elasto-optic constants and the refractive index are known for all the materials, the elasto-optic and the ripple part of the resulting Brillouin scattering cross-section can be obtained. In addition to this the software also calculates the Layer Projected Phonon Density of States (LPPDS), which is the phonon density of states as a function of depth from the film surface [7]. This helps understanding the nature of the acoustic modes.

Another piece of software [8] has been developed which allows, given the dispersion relations of the surface modes (i.e. the position of the surface peaks as a function of the laser incidence angle), for a statistical estimate of the elastic constants of a thin film. It thus solves the so-called "inverse problem". The solution is statistical in the sense that it provides the most probable values for the elastic constants compatible with the measured dispersion relations.

3.3 X-ray scattering

3.3.1 Experimental setups

The x-ray data have been acquired using different x-ray scattering instruments, both in laboratory and at synchrotron radiation sources (SRS, Synchrotron Radiation

Source, at Daresbury, UK; and ESRF, European Synchrotron Radiation Facility, at Grenoble, France). The instruments employed were the Bede Scientific laboratory Grazing Incidence X-ray Reflectometer (GXR1) at the Department of Physics, University of Durham [9, 10], for x-ray reflectivity measurements; beamline 2.3 at the SRS in Daresbury [11, 12, 13] for WAXS, SAXS and x-ray diffraction; and beamline 16 (BM16) at the ESRF in Grenoble for x-ray diffraction [14].

XRR measures the intensity reflected in the specular direction ($\theta_i = \theta_r$) as a function of the grazing incidence angle. The XRR curves were measured on a Bede Scientific reflectometer (GXR1), with a Bede EDRa scintillation detector. The source was a copper target x-ray tube operated at 40 kV and 40 mA, monochromatized to the Cu K_β (λ=1.3926 Å). The specular reflectivity curves were measured as a function of incidence angle using a $\theta/2\theta$ scan, with the detector stepped at twice the step of the specimen. Specular and off-specular reflectivity curves were measured for each sample, with θ_i usually varying in the range 0-10000 arcseconds, with a step of 20 arcseconds. A -0.1^0 offset of the sample angle was used for the off-specular measurements. The true specular reflectivity curves were obtained by subtracting the off-specular measurement from the specular, to remove the forward diffuse scatter.

XRR probes a macroscopic area of sample. The XRR curves of laterally inhomogeneous films are a convolution of different periods (i.e. the fringes are less marked). The x-ray beam is 1-5 mm wide and 100 μm high (as defined by beam defining slits), with a divergence of about 20''. At very small angles of incidence, the footprint on the sample is 1-5 mm by 1-2 cm. This is particularly significant when comparing roughness from XRR to atomic force microscopy (AFM) or scanning tunnelling microscopy (STM), where the area probed is typically only 0.1-1 μm^2. A more detailed description of the GXR1 can be found elsewhere [9, 10]. Since several references exist concerning the alignment and experimental requirements for x-ray reflectivity (including Ph.D. theses from this University), the reader is referred to them. Some references in particular [9, 10, 15, 16] provide a description of the alignment and experimental procedures for the GXR1 and synchrotron beamlines. The same references give a description of the mechanisms of generation of the x-rays and of beam conditioning techniques (see also [17]).

A typical x-ray scattering experimental set-up is shown schematically in fig. 3.4. The slit sizes shown are typical for reflectivity experiments.

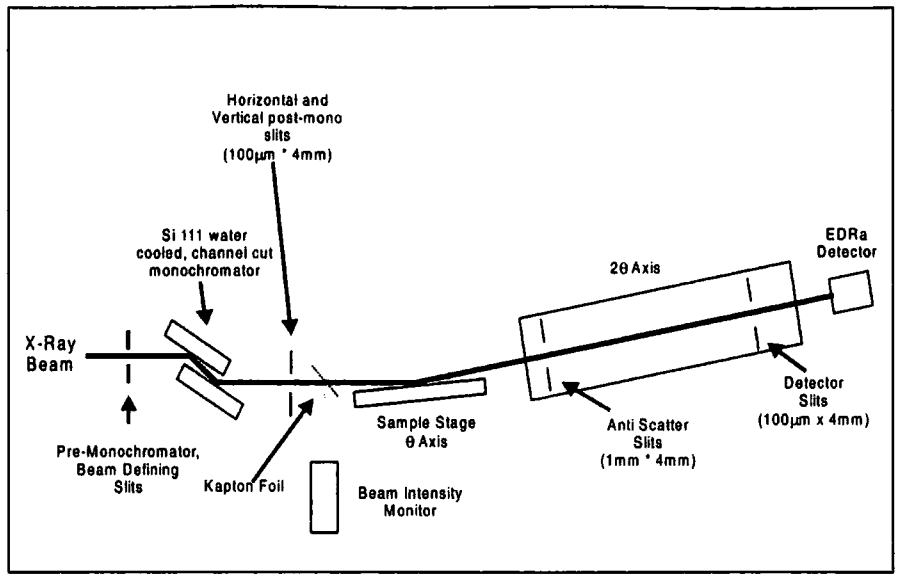

Fig. 3.4: Schematic of a typical two-circle x-ray scattering experiment (Station 2.3 at SRS, Daresbury).

The x-ray scattering experiments presented in this thesis rely on this basic scheme, although the exact nature of each component can vary from instrument to instrument.

X-ray diffraction, SAXS (Small Angle X-ray Scattering) and WAXS (Wide Angle X-ray Scattering) were performed at synchrotron sources. Synchrotron radiation is produced when charged particles undergo a relativistic acceleration process [18, 19]. In a typical synchrotron radiation source, electrons are accelerated in a linear accelerator before being injected into a booster ring where they are further accelerated. When they have reached the required energy they are injected into the storage ring, which forms the major part of the source. At Daresbury SRS the energy of the electrons is 2 GeV and the ring has a circumference of 96 m; at the ESRF the energy of the electrons is 6 GeV and the ring has circumference of 750 m. The moving particles are guided round the storage ring by means of a series of steering magnets, while their energy is supplied by means of radio frequency cavities. As the charged particles accelerate round the storage ring they emit x-rays (Brehmsstralung or braking radiation) which are delivered to an experimental hutch via beamlines. In addition to x-rays produced at the bending magnets in the ring, insertion devices, such as wigglers and undulators, can also be used to generate different spectra of x-rays [18, 19]. For example, BM16, situated 56m away from a bending magnet, allows access to energies in the range 5-40 keV (λ = 2.6-0.32 Å). At SRS 2.3 wavelengths in the range 0.5-2.5 Å

are available. The major advantages of synchrotron x-ray radiation are the very high photon flux, the collimation and thus low divergence of the beam, and the frequency spectrum of the emitted x-rays, allowing a wide range of wavelengths to be selected (i.e. energy dependent experiments can be performed on a single beamline).

For experimental purposes, a monochromatic, low divergent beam is required before the generated x-ray beam reaches the sample. Due to the relativistic nature of the electrons, this low divergence is achieved inherently at a synchrotron (i.e. approximately 200'' vertical divergence at SRS beamline 2.3). The wavelength can then be selected by using a monochromating crystal (e.g. a water-cooled Si (111) monochromator at SRS 2.3; after monochromation the angular divergence of the incident beam, at this station, is about 10''). At BM16 [14] the monochromator consists of two Si (111) crystals. The first is flat whilst the second can be bent to focus sagittally the beam. A horizontal focusing system is adopted with the source to crystal distance being equal to the sample distance. Such sagittal focusing does not affect the vertical collimation of the beam. Use of a further mirror placed directly down-stream of the monochromator allows the beam to be focused vertically, thus increasing the incident flux. In contrast to SRS 2.3, all the optics at the ESRF are housed in a separate hutch, resulting in a much lower experimental background noise. A layout of the beamline is shown in fig. 3.5.

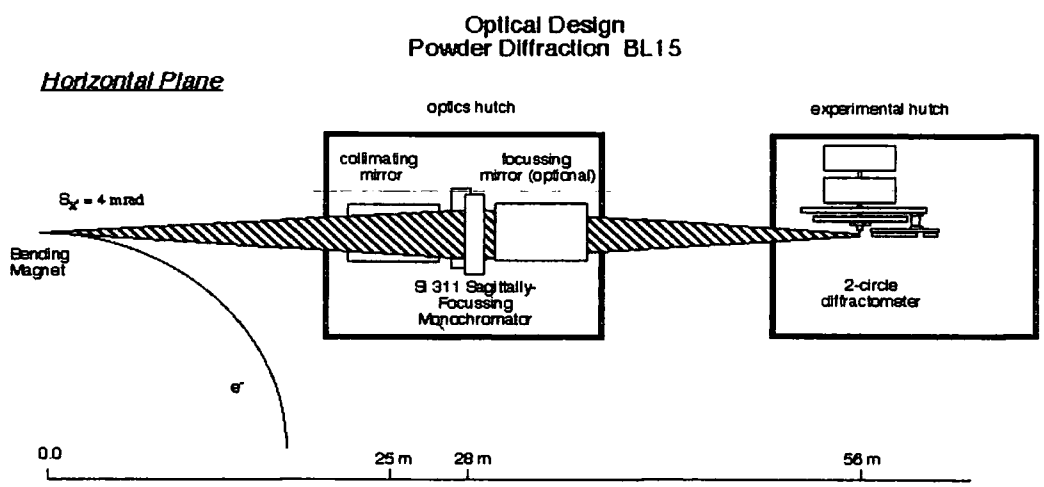

Fig. 3.5: Schematic of the layout of BM16, ESRF.

For all the instruments, the conditioned beam passes through a set of beam defining slits. These can be varied in height and width to give the required beam size and energy bandpass on the sample.

The detection of x-rays is of course critically important. In a typical reflectivity experiment the detector must be able to detect a totally reflected beam and then be accurate enough to handle the low intensity of the diffuse scatter. The difference in intensity can be of many orders of magnitude. The detector used in all the experiments was the Bede EDRa [20]. This high dynamic range detector has a minimum count rate of about 0.15 counts per second and was found to be non-linear for count rates greater than $4 \cdot 10^5$ counts per second. The dead time of the detector was calculated to be 350 ns.

In order to define the resolution of the experiment, a series of slits are placed immediately in front of the detector, as shown in fig. 3.4, the height of the slits being the same as that of the incident beam. In addition, anti-scatter slits are placed on the detector arm close to the sample, in order to reduce the noise at the detector by eliminating extraneous scatter. In order to reduce further the absorption, the air path from the sample to the detector is typically evacuated at synchrotron beamlines. It is also possible to use Soller slits. Soller slits are a set of parallel thin foil sheets that absorb nearly all of the x-rays not travelling parallel to the metal sheets.

The availability of high intensity, highly collimated beams of x-rays from synchrotron radiation sources has led to the widespread use of the parallel beam geometry for powder diffraction [21-24]. While Soller slit collimation of the detector is used for moderate resolution, use of a single crystal analyser not only increases the resolution, but also permits the possibility of parallel data collection in a a multidetector array [14]. The two circle diffraction instrument at station BM16 at the ESRF, which consists of two high-precision, heavy-duty rotary tables aligned coaxially on a base plate, has a nine channel array of 111 oriented Ge crystals each in front of a scintillation detector. Each channel is separated by 2°. At BM16 there is the option of using this set of analyser crystals in preference to the slits geometry. This analyser set-up was used to obtain the high angle diffraction data discussed in chapter 6. Another detector used for experiments at BM16 was a CCD camera for the collection of 2-dimensional diffraction patterns. This device has the advantage of collecting the whole diffraction pattern in a few seconds, which is useful for example in measurements where the experimental conditions change very rapidly (e.g. temperature, pressure, chemical reactions); the disadvantage is in the need of a careful calibration to obtain quantitative data. Soller slits were used for x-ray diffraction measurements at SRS beamline 2.3.

A furnace for high-temperature powder diffraction measurements at temperatures up to 1600 °C has been recently commissioned at BM16 and used for the study of melting of the tin nanoparticles. A similar furnace has also been used at station 2.3 at the SRS.

3.3.2 Analysis software

Structural data of the films studied with x-ray reflectivity were extracted by fitting to the experimental curve a simulated reflectivity curve, using the Bede REFS-MERCURY software package. This uses Parrat's recursive formalism of the Fresnel equations to calculate the reflected wave amplitude and thus the reflected intensity. A genetic algorithm is used to minimise the logarithm of the difference in the absolute intensity between the simulated and experimental curve as the model parameters are adjusted by the computer.

References for Chapter 3:

[1] P. Bruesch, "Phonons: Theory and Experiments II", Springer-Verlag (1986)

[2] J.M.Vaughan, "The Fabry-Perot Interferometer" Adam Hilger, Bristol (1989)

[3] S.E. Gustaffson, M.N. Khan, J. van Eijk, J. Phys. E **12**, 1100 (1979)

[4] J.R. Sandercock, J. Phys. E **9**, 566 (1976)

[5] J.R. Sandercock, US Patent 4,225,236 (1980)

[6] A. Amici, M.G. Beghi, C.E. Bottani, Computational Material Science **17**, 404 (2000)

[7] M. Beghi, C.E. Bottani, P.M. Ossi, T. Lafford, B.K. Tanner, J. Appl. Phys. **81**, 672 (1997)

[8] R. Pastorelli, Ph.D. Thesis, Politecnico di Milano (2000)

[9] I. Pape, Ph.D. thesis, University of Durham (1997)

[10] J. M. Hudson, Ph.D. thesis, University of Durham (1994)

[11] R.J. Cernik, P.K. Murray, P. Pattison, A.N. Fitch, J. Appl. Cryst. **23**, 292 (1990)

[12] S.P. Collins, R.J. Cernik, P. Pattison, A.M.T. Bell and A.N. Fitch, Rev. Sci. Instrum. **63**, 1013 (1992)

[13] C.C.Tang, S.P.Collins, B.M.Murphy, N.D.Telling, R.A Wogelius, S.J.Teat. Rev. Sci. Instr. **69**, 1224 (1998)

[14] A.N. Fitch, Materials Science Forum **228**, 219 (1996)

[15] B.D. Fulthorpe, Ph.D. thesis, University of Durham (1999)

[16] T.P.A. Hase, Ph.D. thesis, University of Durham (1998)

[17] "X-Ray Science and Technology", ed. A. G. Michette and C. J. Buckley, IOP Publishing (1993)

[18] "Neutron and Synchrotron Radiation for Condensed Matter Studies" Vol.1, Eds. J. Baruchel, J.-L.Hodeau, M.S. Lehmann, J.R. Ragnard, C. Schlenker, Springer-Verlag (1993)

[19] G.Margaritondo, Journal of Synchrotron Radiation **2**, 148 (1995)

[20] S. Cockerton, B.K. Tanner, Advances in X-Ray Analysis **38**, 371 (1995)

[21] W. Parrish, M. Hart, T.C. Huang, J. Appl. Cryst. **19,** 92 (1986)

[22] W. Parrish, M. Hart, Z. fur Kristall. **179,** 161 (1987)

[23] M. Hart, R.J. Cernik, W. Parrish, H. Toraya, J. Appl. Cryst. **23,** 286 (1990)

[24] T.C. Huang, M. Hart, W. Parrish, N. Masciocchi, J. Appl. Phys. **61,** 2813 (1987)

Chapter 4

X-ray reflectivity from amorphous carbon films

4.1 Introduction

Carbon shows a variety greater than any other element in the types of chemical bonds it can form, both with itself and with other elements. In most chemical environments it forms electronic states that are close to the sp^3, sp^2 or sp^1 hybridizations, and in the crystalline state sp^3 and sp^2 hybridizations occur as diamond and graphite, respectively. In the amorphous state (for a good review see [1-4]), the possibility of intermediate hybridization states arises because some atoms in the network are in highly strained configurations. The symbol a-C is generally used to refer to a predominantly sp^2 bonded carbon and the symbol ta-C (tetrahedral amorphous carbon) to a predominantly sp^3 bonded network. Amorphous carbons containing significant hydrogen levels are denoted by the symbols a-C:H or ta-C:H. Amorphous carbons with a high value of sp^3 content, density and hardness are also referred to as diamond-like carbon (DLC). Most of the literature refers to amorphous carbon in the form of a thin film.

Hard amorphous diamond-like carbon (DLC) coatings exhibit mechanical, thermal and optical properties close to that of diamond. They can be deposited over a wide range of thickness by different deposition processes, on a variety of substrates at or near room temperature. Friction and wear properties of some DLC coatings can be very attractive for tribological applications.

The first documented report of a dense amorphous carbon was made by Aisenberg and Chabot (1971) [5], while Aksenov and co-workers [6] were the first to use a cathodic arc in vacuum to generate a plasma. Since then many deposition techniques have been developed: high pressure and high temperature treatment of precursors, cathodic arc, laser ablation, plasma-enhanced chemical vapour deposition, electron cyclotron resonance chemical vapour deposition, ion beam deposition, sputtering, ion beam damage of glassy carbon or diamond, cluster beam deposition (see

chapter 5), etc. The properties of the films strongly depend on the average ion (or atom) energy used for deposition.

The most important application of DLC films is in the field of tribological applications, e.g. for hard protective coatings. Their unique properties include high hardness and wear resistance, chemical inertness, lack of magnetic response, and an optical band gap ranging from zero to a few eV. The high hardness, good friction and wear properties, versatility in deposition and substrates and no requirement of post-finishing make them very attractive in particular as overcoats for magnetic media and heads for magnetic storage devices.

Carbon films are also being studied for optical and electronic applications, for example in heterojunction devices, field effect devices, field emission devices (e.g. for flat panel displays).

The key structural parameters that determine the properties of amorphous carbons are the density, the sp^3 fraction, the clustering of the sp^2 phase and the hydrogen (or nitrogen) content. Electron Energy Loss Spectroscopy (EELS) is presently the method of choice to obtain the sp^3 content (from the size of the π^* peak in the carbon K edge absorption spectrum), and the mass density (deduced from the valence plasmon energy in the low energy loss spectrum). EELS suffers from the main drawback that it is destructive and time consuming. It requires accurate procedures for data collection and analysis, which have not always been followed in published works. Indeed, to translate the valence plasmon energy into mass density, an appropriate choice of an electron "effective mass" is necessary, which is complicated by the presence of hydrogen or nitrogen. Furthermore, standard EELS analysis does not give any information about the possible layering within the films, unless using cross sectional EELS, which again implies a complex and careful sample preparation [7].

In this chapter it will be shown how grazing incidence X-Ray Reflectivity (XRR) can be successfully applied to several different kinds of amorphous carbons in order to determine the density, roughness and cross sectional layering without any sample preparation or damage [8]. XRR gives information about the total electron density, which can be directly translated into mass density without any assumption of the value of the electron effective mass.

Different authors have made different choices of the effective electron mass from which they have derived the mass density from the valence electron density [9, 10]. Three other methods are mainly used to determine the mass density of carbon films and

to benchmark the density derived from the plasmon energy, i.e. flotation, weight gain, and Rutherford Back Scattering (RBS). These independent density determinations never fully agreed with EELS [9-11]. There is a reasonable agreement for denser materials such as ta-C, even though with broad data scattering [9-11]. However, weight gain gives lower values than flotation and plasmon energy for porous materials because the latter measure the microscopic density [11]. Moreover, RBS is usually combined with profilometry, resulting in wide error-bars.

XRR provides a probe of the near surface total electron density, whilst EELS is a probe of the valence electron density. Thus, the combination of XRR and EELS can be used to fit directly an effective electron mass. It will be shown how an appropriate choice of the effective mass gives a good agreement with the XRR mean densities, thus validating the use of the "quasi free" electron model to analyse the low loss spectrum. Indeed, a unique effective mass for all amorphous carbons and diamond is obtained [8] and the correct general relation between density and coordination for carbons is therefore presented. For samples containing nitrogen, the comparison of XRR and EELS, for samples of known composition, can provide a way to assess the number of nitrogen valence electrons to be considered in the plasma oscillations.

XRR is also a powerful tool to check the cross sectional layering of films. When analysing a wide variety of films grown under different conditions it was found that extremely uniform or layered films can result from different preparation conditions within the same deposition system. In particular, we show that heavy layering is not a fundamental property of tetrahedral amorphous carbon (ta-C) films, but is linked instead to the functioning of the deposition apparatus.

Hydrogen content is usually measured by Elastic Recoil Detection Analysis (ERDA) or nuclear reaction analysis. A combination of EELS and XRR can also provide a way to quantify the hydrogen content, even though the EELS measurement errors hinders this as a precise quantitative method. On the other hand, a combination of XRR and H effusion analysis is a precise and efficient way to obtain the hydrogen content.

4.2 Samples

Measurements were undertaken on tetrahedral amorphous carbon (ta-C), hydrogenated ta-C (ta-C:H), nitrogen-containing ta-C (ta-C:N) and ta-C:H (ta-C:N:H),

amorphous carbons (hydrogenated) a-C:(H), and nanostructured a-C films, all deposited on Si substrates (see Tables 4.1 and 4.2).

Most of the samples were deposited by the Electronic Devices and Materials group in the Engineering Department at the University of Cambridge (UK). PLD (Pulsed Laser Deposition) films were deposited at the University of Trento (Italy) and nanostructured carbon films were deposited in the Nanoaggregates Laboratory of Milan (LAMiNa) in the Department of Physics at the University of Milan (Italy).

Five sets of ta-C films, grown with different sources and under different deposition conditions, were analysed:

- the first set was deposited using a single bend Filtered Cathodic Vacuum Arc (FCVA) system [10] with different substrate biases: -290V, -200V, -80 V, +10 V and with a floating potential (the bias determines the energy of the deposited ions);
- the second set was deposited using a double S-Bend FCVA [12] at biases of -20V, -100V and -300V;
- the third set was deposited using a single bend FCVA at a fixed bias voltage of -80V and for increasing deposition times (20, 30, 45, 60 and 90 seconds);
- the fourth set was deposited at a floating potential with increasing deposition times (25, 50 and 75 seconds) using the defocused beam of an S-bend FCVA in order to achieve a very low deposition rate (~1.5 Å/s) and thus ultrathin films;
- the fifth set was deposited by Pulsed Laser Deposition (PLD) at a laser fluence of 1, 9, 20 and 31 J/cm^2 [13] (the laser fluence controls the ion energy).

Three series of ta-C:H samples were obtained using two Electron Cyclotron Wave Resonance (ECWR) sources (one slightly capacitively coupled) with an acetylene plasma and an ion energy ranging from 80 to 170 eV [14]. A value of approximately 30% for the hydrogen atomic content was derived by Elastic Recoil Detection Analysis (ERDA) for all the films [14]. One of the series consisted of two ultrathin (thickness less than 10 nm) ta-C:H films.

One ta-C:H film was deposited from methane with a Plasma Beam Source (PBS) [15] and ERDA analysis gave a value of ~40% at. H.

Three ta-C:H:N films were deposited by an ECWR source from N_2/C_2H_2 gas mixtures, with known C/N and C/H ratios (measured by a combination of ERDA and XPS [16]).

Two ta-C:N films were deposited by a combination of a carbon plasma, given by an FCVA, and a nitrogen plasma, given by an ECWR [17].

Two a-C:H films were deposited from methane using a Plasma Enhanced Chemical Vapour Deposition reactor (PECVD), with an estimated H content ~30-40% at., and one polymeric a-C:H film was deposited with an estimated H content of ~40-50% at.

An a-C sample was deposited by DC magnetron sputtering [18].

Two nanostructured a-C films were produced by deposition of supersonic carbon cluster beams of different average cluster size generated by a Pulsed Microplasma Cluster Source (PMCS) [19] (see chapter 5).

We thus analysed a wide variety of different samples covering the full range of materials usually considered in the literature.

4.3 Experiment

4.3.1 EELS

The EELS experiments were carried out by V. Stolojan and L.M. Brown at the Cavendish Laboratory (Cambridge, UK) on a dedicated VG 501 Scanning Transmission Electron Microscope (STEM) equipped with a spectrometer with a McMullan parallel EELS detection system [20]. The data analysis was performed by V. Stolojan and A.C. Ferrari, of the Department of Electronic Engineering (University of Cambridge). For each sample, forty spectra of the carbon K edge were collected, as well as the low-loss spectrum containing the plasmon and the zero-loss electrons. Both spectra were Fourier log ratio deconvoluted with the spectra of the electron beam going through vacuum [21]. The background was then removed from the carbon K-edge, followed by the removal of multiple scattering by deconvolution with the low-loss data by Stephan's method [21]. The π^* peak at 285 eV of the carbon K-edge was modelled with a gaussian line-shape, and its area was normalised to the area of the σ^* edge in the window 284-310 eV. Referencing this to the equivalent area for graphite, the sp^2 content was obtained [10, 22]. The plasmon energy is derived by fitting the energy loss function to the single plasmon peak (see next subsection). All spectra were collected at a convergence angle of 7.4 mrad and an acceptance angle of 7 mrad, for 100 keV electrons. This particular choice of angles ensures that, at the energy of the carbon K-edge, all directions in the sample are equally probed. The results are thus independent of any anisotropy within the films [23-25].

4.3.1.1 Plasmon energy

The low energy loss spectrum in EELS is related to the valence plasmon excitations and is proportional to the energy loss function, Im(-1/ε); ε is the complex dielectric function. In the free-electron limit, ε is given by the Drude model [21]

$$\varepsilon(\mathrm{E}) = 1 - \frac{E_p^{\,2}}{E^2 + iE\Gamma} \tag{4.1}$$

and so the energy loss function is

$$\mathrm{Im}\left(-\frac{1}{\varepsilon(E)}\right) = \frac{E_p^{\,2} E\Gamma}{(E^2 - E_p^{\,2})^2 + (E\Gamma)^2} \tag{4.2}$$

where E_p is the plasmon energy and Γ is the FWHM of the energy loss function. The plasmon energy is defined as:

$$E_p = \hbar\left(\frac{n_e e^2}{\varepsilon_0 m^*}\right)^{\frac{1}{2}} \tag{4.3}$$

where e is the electron charge, ε_0 is the dielectric permittivity of vacuum, n_e is the valence electron density and m^* is the electron "effective mass" (m_e being the free electron mass). The energy loss function reaches a maximum at:

$$E_{max} = [E_p^{\,2} - (\Gamma/2)^2]^{1/2} \tag{4.4}$$

In order to derive the mass density of amorphous carbons from the valence electron density n_e, it is assumed that C contributes with 4 electrons, N with 5 (though some groups suggest 3 valence electrons for N), and H with 1, thus obtaining:

$$n_e = 12\frac{\rho N_A}{M_C}\left(\frac{3X_C + 4X_N + 1}{11X_C + 13X_N + 1}\right) \tag{4.5}$$

where ρ is the mass density, N_A is the Avogadro number, M_C is the atomic carbon mass and $X_H = 1 - X_C - X_N$ (X_j is the atomic fraction of element j). Thus, the mass density becomes:

$$\rho = \frac{\varepsilon_0}{12\hbar^2 N_A e^2} M_C m^* E_P^{\,2}\left(\frac{11X_C + 13X_N + 1}{3X_C + 4X_N + 1}\right) \tag{4.6}$$

The usual approach has so far been to derive m^* in Eq. (4.6) in order that the density of diamond (3.515 g/cm^3) would correspond to its measured plasmon energy of 33.8 eV [10]. This results in $m^* \sim 0.85 m_e$. Further scatter in the m^* comes from different

values of the diamond plasmon energy found in the literature (33.3 eV [21], 34 eV [10], 33 eV [9]). Moreover, some groups proposed that given the high plasmon energy with respect to the typical band gap, the electrons should be considered totally free, thus assuming $m^*=m_e$ [26]. This introduces a further 15% difference in the derived densities, which must be taken into account when comparing data from different sources.

Finally, whilst the fitting procedure to get the critical angle from XRR measurements (see below) is quite standard, in the literature Eq. (4.2) is not always used to fit the plasmon energy and some groups use E_{max} instead of E_P in Eq. (4.3). Since a typical plasmon energy of a ta-C is ~30 eV, whilst its FWHM is ~15 eV, using E_{max} instead of E_P introduces a difference of ~1 eV between E_p and E_{max}. This results in a further 5-10 % difference in the densities, i.e. 0.2-0.3 g/cm^3 for a typical 3 g/cm^3 density. In this work Eq. (4.2) was always applied to fit the measured plasmon energy.

4.3.2 X-Ray Reflectivity

Several papers about x-ray reflectivity measurements of pure and hydrogenated carbon films can be found in the literature [27-42], and most of them are devoted to density determination (mainly as a function of deposition parameters). Few are devoted to thickness or roughness determination. Lucas *et al.* [34] and J. Martinez-Miranda *et al.* [41] used XRR to follow the density evolution during annealing of sputtered amorphous carbon and PLD ta-C, respectively. The latter reported the presence of a feature attributed to a Bragg peak, due to a quasi-periodic array of scattering sites created by thermal annealing within the amorphous phase, without giving any explanation for it. Some studies were performed using neutron reflectivity (e.g. [35]) and Findeisen *et al.* [36] combined neutron and x-ray reflectivity to determine at the same time the density and the H content of the films. Logothetidis *et al.* [30-33] studied the relationship between roughness and thickness in r.f. magnetron sputtered a-C films. Zhang *et al.* [39, 40] conducted a thorough investigation of the effects of bias voltage and deposition pressure on hydrogenated amorphous carbons. Lucas *et al.* [34] first reported a multilayer structure for DC magnetron sputtered a-C films, with a C/Si interface of ~1.5 nm and density ~1.7 g/cm^3, a bulk carbon layer of density ~2.25 g/cm^3 and a surface layer of ~1 nm and density ~1.2 g/cm^3. Martinez-Miranda *et al.* [41] indicated the possibility of a multilayer structure in PLD ta-C films. Siegal *et al.* [43,

44] showed the presence of at least 3 layers in the structure of PLD ta-C films, by combining High Resolution Transmission Electron Microscopy (HRTEM), Rutherford Back Scattering (RBS) and XRR. They also observed an evolution in thickness and density of the layers as a function of the PLD energy density. Siegal *et al.* [45] recently used HRTEM to observe a similar behaviour in a set of films grown with a single bend FCVA, proposing a physical mechanism, the backscattering subplantation, as being responsible for layering in carbon films [43].

Reflectivity curves as a function of the incidence angle were measured on the Bede Scientific GXR1 reflectometer (λ=1.3926 Å). Specular and off-specular reflectivity curves were measured for each sample, with the grazing incidence angle usually varying in the range 0-10000 arcseconds, with a step size of 20 arcseconds. A -0.1° offset of the sample angle was used for the off-specular measurements.

Films laterally inhomogeneous in thickness give a convolution of different periods in the reflectivity curve, and thus the interference fringes are less marked. The x-ray beam width, defined by the slit width was in the range 1-5 mm, and the beam height was 100 μm. At very small angles of incidence the footprint on the sample was (1-5 mm) x (1-2 cm). Thus XRR probed a macroscopic area of the sample.

By fitting the x-ray reflectivity data to simulated curves, obtained using the Bede REFS-MERCURY software package, more detailed information on the parameters of interest could be obtained, especially in the case of layered films.

4.3.2.1 Density determination

In amorphous carbons we have in general to consider three elements, carbon, hydrogen and nitrogen. From Eq. (2.44) the critical angle θ_c is given by

$$\theta_c = \lambda\sqrt{\frac{N_A r_0}{\pi}\rho\frac{[X_C(Z_C + f_C') + X_H(Z_H + f_H') + X_N(Z_N + f_N')]}{(X_C M_C + X_H M_H + X_N M_N)}} \qquad (4.7)$$

where λ is the x-ray wavelength, ρ is the overall mass density and X_j is the atomic fraction of element j, M_j is the mass number of element j, Z_j is the atomic number of element j, $r_0 = e^2/4\pi\varepsilon_0 m_e c^2$ is the electron classical radius, N_A is the Avogadro number. At λ=1.3926 Å we have $f_j' \approx 10^{-2}$ (electron units) [46], i.e. the dispersion corrections are very small. Thus letting $f_j' = 0$ we obtain, with $X_H = 1 - X_C - X_N$:

$$\rho = \frac{\pi^2 c^2 \varepsilon_0}{3\lambda^2 N_A e^2} M_C m_e \theta_c^{\,2} \frac{11X_C + 13X_N + 1}{5X_C + 6X_N + 1} \qquad (4.8)$$

where e is the electron charge, m_e is the electron mass, ε_0 is the dielectric permittivity of vacuum. We note that the dependence on the H content is quite small in the usual range X_H = 10-50 % (e.g. for $X_N = 0$, if θ_c = 720" at λ=1.3926 Å, ρ is 2.3 g/cm^3 when $X_H = 0.1$ and 2.16 g/cm^3 when $X_H = 0.5$).

The structure of Eqs. (4.8) and (4.6), giving the mass density via XRR and EELS, can be directly compared. In Eq. (4.8) the unknowns are the critical angle θ_c, the carbon fraction X_C and the nitrogen fraction X_N. In Eq. (4.6) the unknown are the plasmon energy E_P, the carbon fraction X_C, the nitrogen fraction X_N and the effective electron mass m^*. It is assumed that N contributes with 5 valence electrons. Eq. (4.8) has a weaker dependence on the H content with respect to Eq. (4.6) ($5X_C$ and $6X_N$, instead of $3X_C$ and $4X_N$, at the denominator), so the XRR density is less affected by any error in the determination of the H content. The approximations used in the derivation of Eq. (4.6) are weaker than the ones in Eq. (4.8). The weak point of Eq. (4.6) is the unknown electron effective mass which naturally arises from the assumption of a "quasi free" electron model.

Some films such as ta-C:H films have a density (and therefore a critical angle) which is similar to or just smaller than the Si substrate density (2.33 g/cm^3), so that the Si critical angle is often seen, and not that of the film. The presence of the film only acts as a perturbation on the shape of the critical angle (see fig. 4.1) and a simulation of the reflectivity curve is needed to extract the density information. In the case of films with very low density (e.g. cluster-assembled carbon films, or less markedly, in the case of a-C:H and a-C films) a double critical angle is distinguishable (fig.4.1), thus allowing a better determination of the density. In fact, if the layer density is lower than the substrate, X-rays start to penetrate when the incidence angle θ_i becomes greater than the film critical angle and the reflected intensity falls sharply due to absorption in the film, subsequently undergoing total external reflection at the film-substrate interface. When the incidence angle becomes greater than the substrate critical angle, x-rays penetrate into the substrate and a second intensity fall is seen in the reflectivity curve beyond the substrate critical angle (see fig. 4.1).

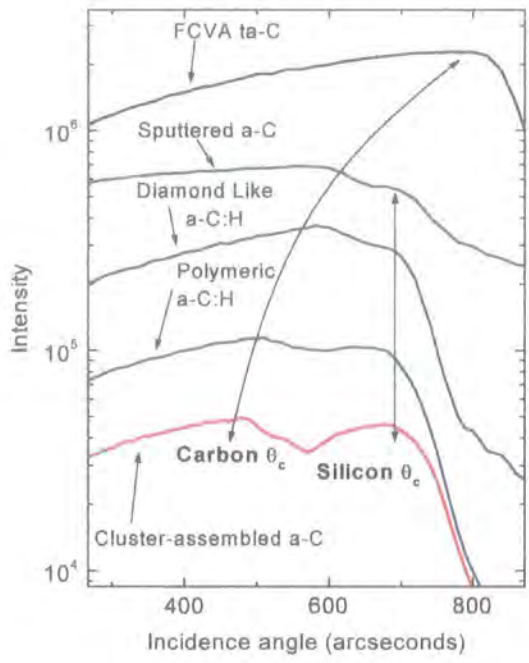

Fig. 4.1: Experimental X-ray reflectivity spectra for diamond-like a-C:H, polymeric a-C:H and cluster-assembled a-C films. Their electron density is lower than in the silicon substrate, so they show a double critical angle, as indicated. The top line is the reflectivity curve of a ta-C FCVA film, whose density is greater than in Si; in this case a single critical angle is detected.

In general, if the film is made of a bulk, dense layer with a top and a bottom layer that are less dense, the critical angle (and the density that one can obtain from it) is that of the bulk layer. This means that what we get from the analysis of the critical angle is the density of the densest layer and not the average film density, which requires a fit of the multilayer structure. This is typically the case for ta-C films (see below). On the other hand, EELS provides an average of the density over the whole film thickness.

The penetration depth for incidence angles θ_i greater than the critical angle is [44, 47, 48]:

$$D = \frac{\lambda}{2\pi q}, \tag{4.9}$$

where

$$q = \sqrt{\frac{(\theta_c^2 - \theta_i^2) + \sqrt{(\theta_c^2 - \theta_i^2)^2 + 4\beta^2}}{2}} \tag{4.10}$$

and (see Eq. (2.43))

$$\beta = \frac{\lambda\mu}{4\pi} \tag{4.11}$$

Here, μ is the linear absorption coefficient, given by the product of the wavelength-dependent mass attenuation coefficient and the density (for carbon $\mu = 2.8 \cdot \rho$ cm^{-1} when $\lambda = 1.3926$ Å [46]).

Indeed, the penetration depth just beyond the critical angle (D_c) of x-rays as a function of carbon mass density and absorption coefficient is

$$D_c = \sqrt{\frac{\lambda}{\pi\mu}}, \tag{4.12}$$

and its value is about $4 \cdot 10^2 \sqrt{\frac{1}{\rho[g/cm^3]}}$ nm for carbon at $\lambda = 1.3926$ Å.

The penetration depth increases as the incidence angle increases, and D_c is smaller for larger densities. For a density $\rho \sim 3$ g/cm^3 D_c is ~200-250 nm. If the surface layer is thicker than D_c, we would directly see, in the specular scan, the critical angle corresponding to the density of the first D_c of this surface layer. In our case, the surface layer is usually less than 10 nm and so the x-rays penetrate without giving a "surface" critical angle. We thus directly see the density of the bulk layer (of its upper part, limited by the penetration depth at this density). If the surface region has a density gradient, or if the distinction between the bulk and the surface layer is not sharp, the critical angle may be smoothed and refers to an average density of a surface region whose thickness is defined by the penetration depth. Thus, for layered films, the whole reflectivity curve must be simulated to obtain the density of the other layers and thus the total average density. Note that our definition of D_c gives values roughly 5 times bigger than the D_c derived by Siegal *et al.* [44], but in agreement with simulations of critical angles in structures composed of high and low density layers of various thickness. This difference stems from a different definition of the characteristic penetration depth at the critical angle, given the large gradient of D around θ_c. However, Eq. (4.12) accounts better for the measured critical angles.

Table 4.1: Density, cross sectional structure, roughness (from XRR) and sp^3 content (from EELS) for different sets of films analysed in this chapter. In the column "density" we report the density of the thickest layer, for layered films. Details on interface and surface layer densities and thickness are reported in the third column, if good simulations could be achieved.

Sample	Density (g/cm^3)	Thickness (nm) and Layering	Roughness (±1 Å)	sp^3 (%)
ta-C single bend FCVA -290 V	2.86±0.02 (bulk)	Layered	7	76
ta-C single bend FCVA -250 V	3.12±0.02 (bulk)	2 (interf.) + 64 (bulk) + 4 (surf, 2.3 g/cm^3)	10	
ta-C single bend FCVA -200 V	3.03±0.02 (bulk)	Layered (Fig. 4.5)	6	81
ta-C single bend FCVA -80 V	3.24±0.02 (bulk)	1.5 (interf.) + 63.5 (bulk) + 7 (surf, 2.7 g/cm^3), Fig. 4.4	6.5	87
ta-C single bend FCVA floating	2.91±0.02 (bulk)	Layered	8	78
ta-C single bend FCVA +10 V	2.71±0.02 (bulk)	Layered (Fig. 4.5), see modelled structure in Table 4.3	5	73
ta-C S-bend FCVA –300 V	3.17±0.03	3 (interf.) + 70 (bulk) + 2 (surf, 1.6-1.8 g/cm^3)	4	85
ta-C S-bend FCVA –100 V	3.26±0.03	2.5 (interf.) + 76 (bulk) + 1 (surf. 2.0-2.2 g/cm^3), Fig. 4.3	8	88
Ta-C S-bend FCVA -20 V	3.13±0.03	2 (interf.) + 84 (bulk) + 1 (surf, 1.8-2.0 g/cm^3)	7	86
ta-C PLD 9 J/cm^2	2.88±0.02 (bulk)	6 (interf. 2.5 g/cm^3)+ 58.5 (bulk) + 30.5 (surf., 2.75 g/cm^3), Fig. 4.6	8	
ta-C PLD 20 J/cm^2	3.0 ±0.02(bulk)	Layered		
ta-C:N FCVA+ECWR (14% N)	2.75 (bulk)	4(interf. 2.4 g/cm^3)+28.5(bulk)+2(surf, 2 g/cm^3), Fig. 4.3	6	64
ta-C:N FCVA+ECWR (20% N)	2.53(bulk)	3(interf. 2 g/cm^3)+29.5(bulk)+2(surf, 1.75 g/cm^3)	6	57
ta-C:H ECWR (25% H)	2.39±0.03	82		70
ta-C:H ECWR (30% H)	2.13±0.03	95.5, Fig. 4.3	5.5	70
ta-C:H PBS (40% H)	1.6±0.035			65
ta-C:H:N ECWR (29% H, 16% N)	1.94±0.03	2.5 (interf.) + 91 (bulk) + 2 (surf. 1.5-1.7 g/cm3), Fig. 4.3	6	

Continue

Table 4.1 (continued)

a-C:H PECVD Diamond-Like	1.63±0.035 Fig. 4.1	240	5	58
a-C:H PECVD polymeric	1.3±0.04 (bulk, fig. 4.1)	3.5(interf.) + 255(bulk) + 5.8 (surf, 0.9 g/cm^3), Fig. 4.4		
a-C Magnetron Sputtering	1.72±0.035 Fig. 4.1	Layered, Fig. 4.4	5	<20
a-C Cluster-Assembled	0.9-1.4 Fig. 4.1	---	---	~10

Table 4.2: Density, cross sectional structure and roughness from XRR for a series of ta-C films grown with a single bend FCVA for increasing deposition times and for two series of ultrathin ta-C and ta-C:H films grown with the S-bend FCVA and the ECWR sources. The column 'density' gives the density of the thickest layer. Details on interface and surface layer densities and thickness are reported in the third column.

Sample **Increasing deposition time (sec)**	**Density (g/cm^3)**	**Thickness (nm) and Layering**	**Roughness (±1 Å)**
Ta-C single bend FCVA –80V		(surf. layer < 1nm)	
20	3.20±0.02	2.3(interface, 2.75 g/cm^3)+12.7 (bulk)	4.5
30	3.20±0.02	1.4 (interface, 2.35 g/cm^3)+ 25.2 (bulk)	5
45	3.20±0.02	2 (interface, 2.7 g/cm^3) + 44 (bulk)	5.5
60	3.20±0.02	3.1(interface, 2.6 g/cm^3)+57.8 (bulk)	9.5
90	3.20±0.02	2.2(interface, 2.9 g/cm^3)+ 71.5 (bulk)	10
Ultrathin S-bend FCVA, floating			
25	3.05-3.10	0.5-0.8 (interface, 2-2.2 g/cm^3)+ 3-3.5+0.5-0.8 (surf. 2-2.5 g/cm^3), Fig. 4.7	5-10
50	3-3.2	0.5-1.5 (interface, 2-2.2 g/cm^3)+4.5+0.5 (surf.)	5-10
75	3-3.2	1.5 (interface, 2.5 g/cm^3)+4.8+1.7-1.8 (surf. 2.2-2.4 g/cm^3)	4
Ultathin ta-C:H ECWR			
7	2.1	2-3 (interface, 2-2.1 g/cm^3)+2.3-3.2+2 (surf. 1.5 g/cm^3) , Fig. 4.7	5

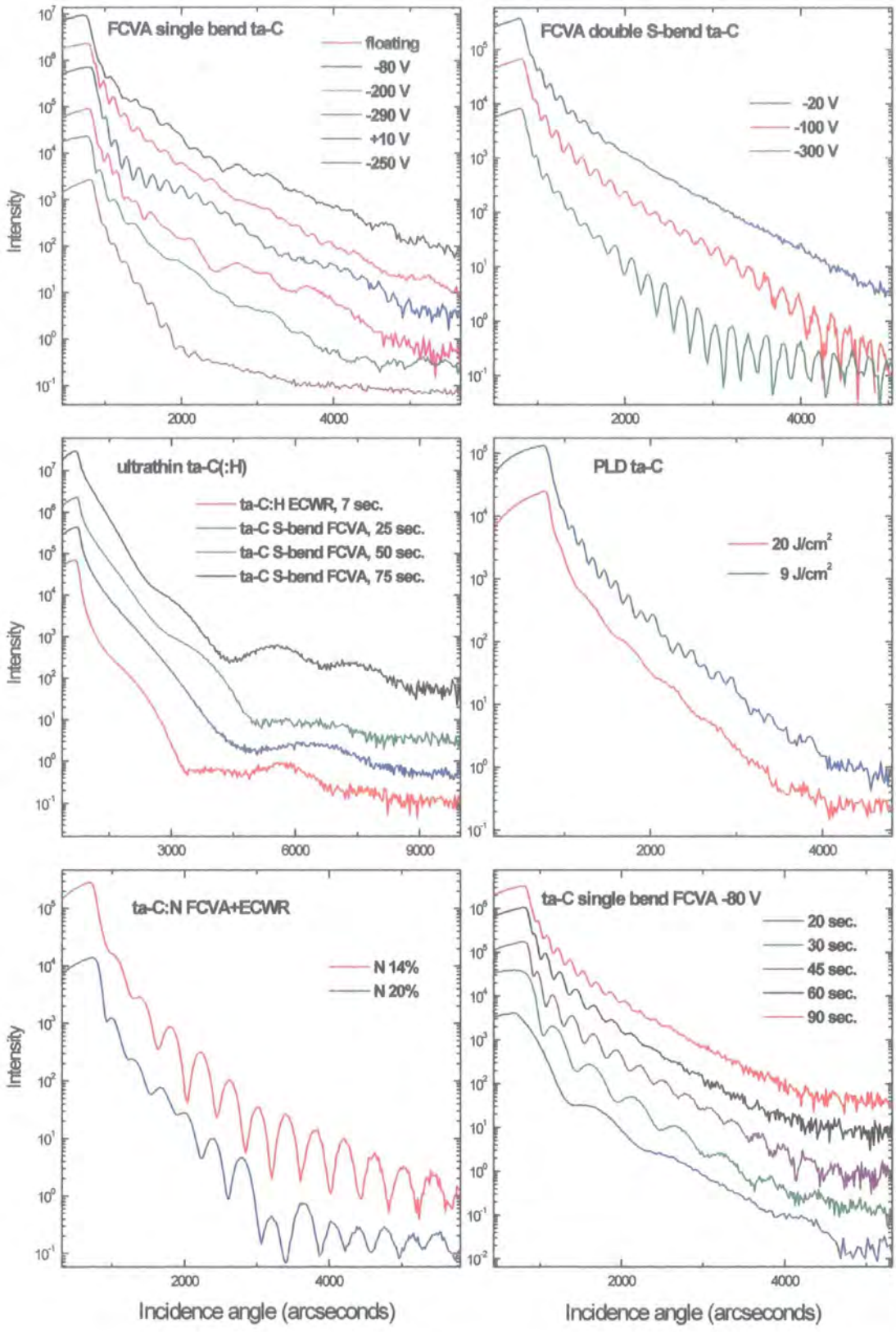

Fig. 4.2: Experimental x-ray reflectivity curves for most of the samples reported in Tables 4.1, 4.2, 4.4 and discussed in this chapter **(continues)**.

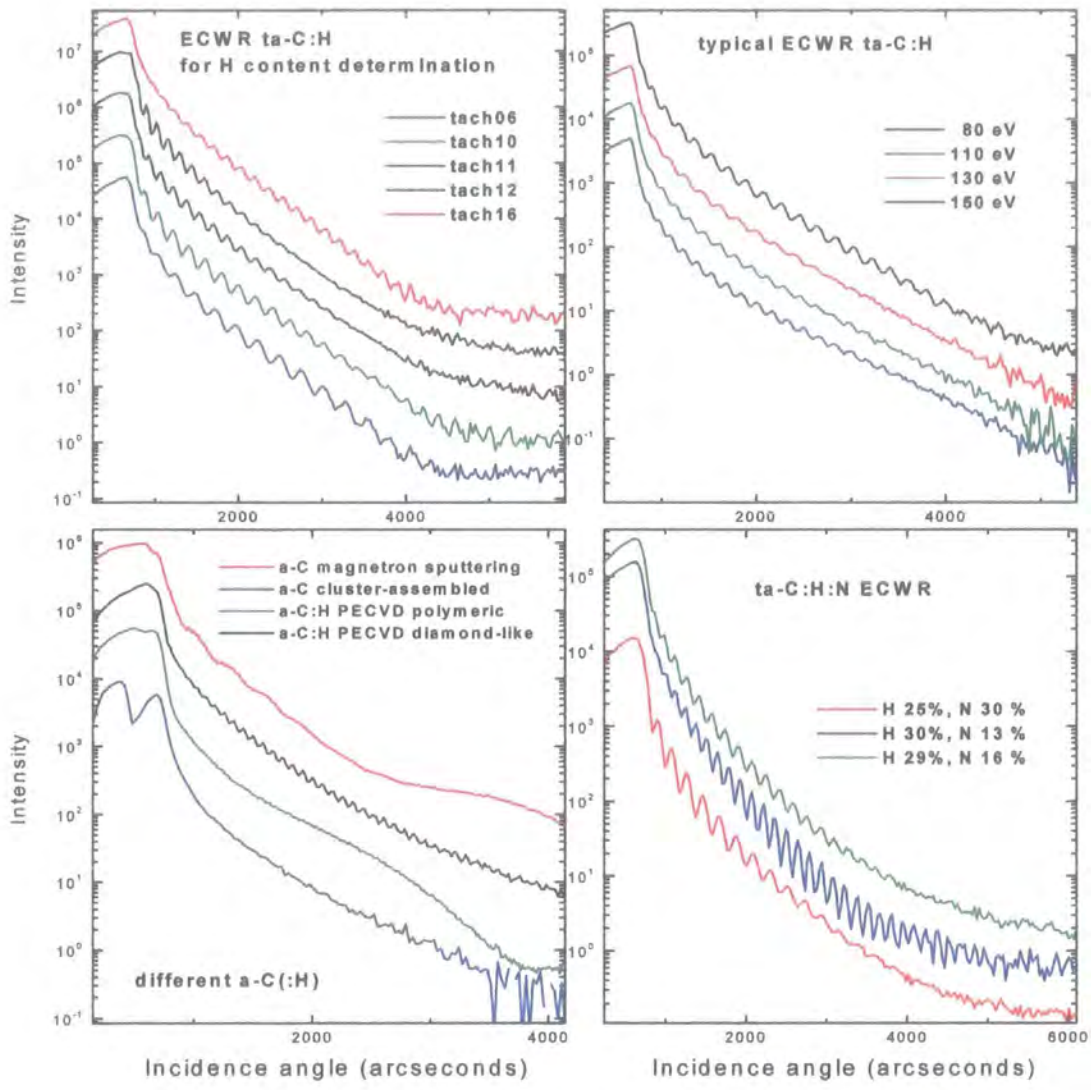

Fig. 4.2 (continued): Experimental x-ray reflectivity curves for most of the samples reported in Tables 4.1, 4.2, 4.4 and discussed in this chapter.

4.4 Results

4.4.1 X-ray reflectivity

Fig. 4.2 shows the experimental x-ray reflectivity curves for most of the films reported in Tables 4.1, 4.2 and 4.4 (see below) and discussed in this chapter. In the following some of these data will be replotted, when convenient, to illustrate the discussion of the most important results.

4.4.1.1 Density and layering

Fig. 4.3 shows a typical XRR curve for a ta-C:H film. Only one fringe period can be seen, showing that these films consist of a single layer. The interference fringe period gives direct information on the film thickness. Very good simulations of the measured curves were obtained for all ta-C:H films. The presence of a 1-2 nm layer of different (lower) density (possibly composed of Si, C and O [7, 34]) at the film-substrate interface, and sometimes of an approximately 1 nm thick layer at the film surface, gives an even better fit of the data. Ta-C:H films from the more capacitively coupled ECWR have a density in the range 2.3-2.4 g/cm^3, whilst the others have densities in the range 2.1-2.23 g/cm^3 (see Table 4.1).

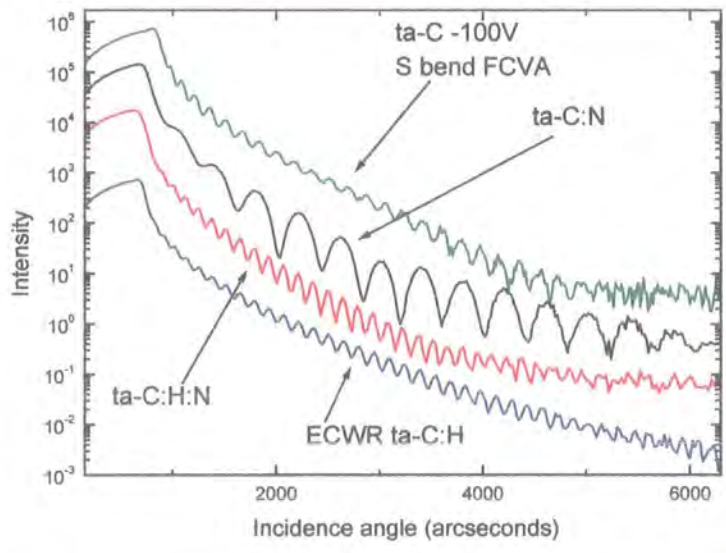

Fig. 4.3: X-ray reflectivity curves for tetrahedral amorphous carbon films.

A similar behaviour was found for ta-C:H:N and ta-C:N films, with a small surface layer (1-2 nm) and an interface layer sometimes thicker than in ta-C:H films (up to 4 nm in the ta-C:N shown in fig. 4.3). The thickness of these films was respectively in the range 80-100 nm (ta-C:H:N) and 30-40 nm (ta-C:N). Fig. 4.3 shows the reflectivity curve for a film with 29% H and 16% N content and of a ta-C:N film with 14% N content. The measured densities are reported in Table 4.1.

Similar results (substantial cross-sectional uniformity) were obtained also for the a-C:H films, with the main difference being a clear double critical angle structure (see fig. 4.1). From this we deduced a density of 1.64-1.74 g/cm^3 for the diamond-like a-C:H films and 1.2 g/cm^3 for the polymeric film. The fit of the latter film required the presence of 2 layers of 3.5 nm and 5.8 nm of lower density (0.85 g/cm^3 and 0.9 g/cm^3) at the Si/C and C/air interface, respectively (see XRR curve in fig. 4.4). The thickness of these a-C:H films was in the range 160-250 nm (Table 4.1).

The magnetron sputtered a-C film showed a double critical angle, corresponding to a density of 1.7 g/cm^3. The XRR curve (fig. 4.4) presents 3 different periodicities, corresponding to 360 nm (total thickness), 40 nm and 5 nm (surface layers); the simulation gives a density varying from 1.7 g/cm^3 (in the bottom layer) to 1.15 g/cm^3 (in the surface layer).

A double critical angle structure was also detected for the nanostructured a-C films (fig. 4.1). The density varied from 0.8 to 1.4 g/cm^3 depending on the cluster size (see chapter 5). Films grown with smaller average cluster size have a higher density [19].

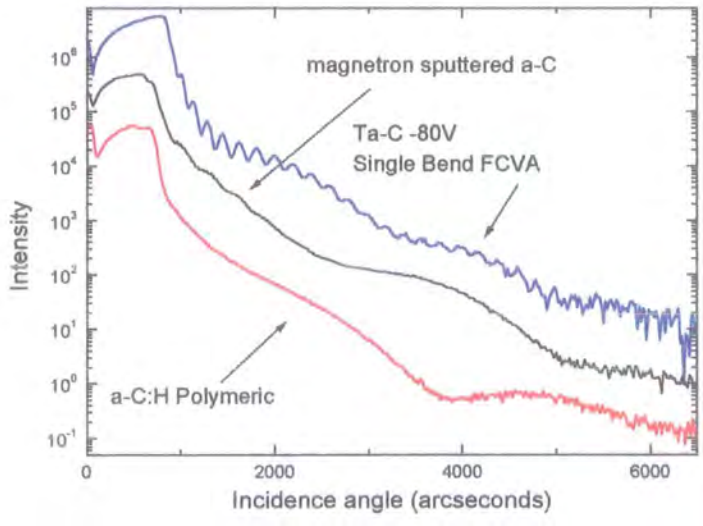

Fig. 4.4: X-ray reflectivity curves of various carbon films showing a surface layer.

For the ta-C films, it is easier to determine the film density from the single critical angle, as this is greater than the substrate critical angle, and as the film composition is well known. The uncertainty of the obtained density value is therefore smaller than in the hydrogenated films (Table 4.1). Densities up to 3.26 g/cm^3 were obtained for an ~88% sp^3 film from the S-bend FCVA (bias –100V). However, for the single bend FCVA films, the reflectivity curves show multiple periodicity (fig. 4.4 and fig. 4.5), which indicates significant internal layering (not just 1-2 nm at the surface or at the substrate interface). They can be simulated taking into account three, or more, layers with different densities. This is supported by cross-sectional HRTEM measurements on the same films [45] and is similar to the findings of Siegal *et al.* [43, 44] on PLD ta-C. Thus the density deduced from the critical angle is that of the bulk, densest layer (and not an average film density) as explained before when discussing the x-ray penetration depth. The density of the other layers can be estimated with less accuracy from the fit parameters, but it is usually smaller, in the range 1.5-2.5 g/cm^3.

Fig. 4.4 shows the reflectivity curve of a single bend FCVA ta-C film grown at –80V bias. We can see a short period due to the overall film thickness and a long period due to a less dense 7 nm surface layer, as confirmed by simulation of the XRR data. Other films show more complex curves (fig. 4.5). The number of layers, their density, thickness, and roughness are all variable and the density of the top and bottom layers (and possibly of the bulk) is probably not constant (e.g. the interfaces are not sharp), whilst the sp^3 content does not vary so much with bias (Table 4.1). Simulation of such a structure is difficult.

Fig. 4.5 shows a simulation in which a three-layer model gives a reasonable account for the measured reflectivity in the case of the +10 V bias FCVA film. The model is reported in Table 4.3. However, only qualitative agreement with the measured data could be found.

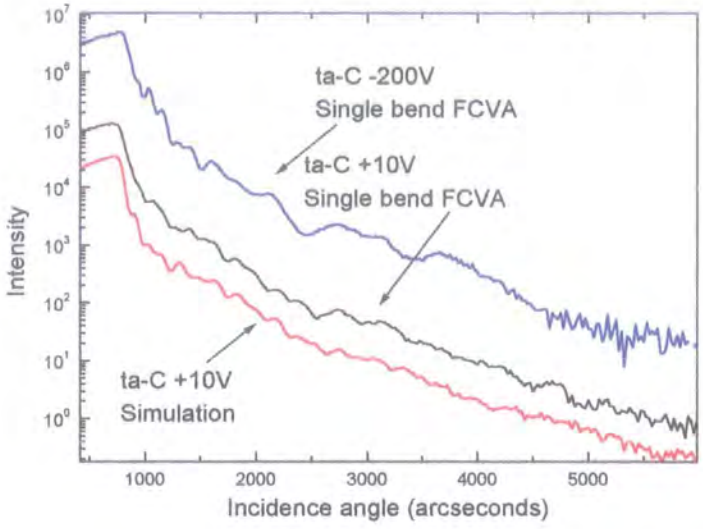

Fig. 4.5: X-ray reflectivity of FCVA ta-C films showing internal layering. One reflectivity curve is compared to the simulated reflectivity.

Table 4.3: Simulated model structure for the +10 V FCVA ta-C film, from substrate to top layer.

	Density (g/cm^3)	thickness (Å)	roughness (Å)
Si			10
C	2.56	275	8
C	2.72	370	8
C	2.43	90	5

The sharp uniform layer approach fails for the first series of single bend FCVA films grown at higher energies, for which the density is probably not constant inside each layer. The total thickness of this series of films was between 50 and 70 nm. XRR cannot give a complete quantitative description of very complex films (such as ta-C grown away from the optimum conditions). Coupling of XRR with cross sectional HRTEM, giving information about the structure of the films, could be a better starting point for fitting reflectivity curves, leading to a better determination of the density of the layers. The evolution of layering with bias was confirmed by HRTEM measurements of Siegal *et al.*, that directly imaged the non-uniform structure [45]. Single bend FCVA films at -80V have always been considered ideal films, having the highest density and sp^3 content, due to the optimum kinetic energy of the deposited atoms. These results would suggest that they are also the most uniform, with the thickest bulk layer and thinnest interfaces. A similar layered structure was found for the PLD ta-C films; fig. 4.6 shows the measured and simulated reflectivity curves for the sample grown at 9 J/cm^2, resulting in 3 layers (see structure model in Table 4.1).

Layering in PLD ta-C was found also by Siegal *et al.* [43, 44]. They also reported the presence of a Bragg scattering peak attributed to quasi-periodical nm-sized regions of localised strain fields. However we never detected such a peak in any of the films we examined.

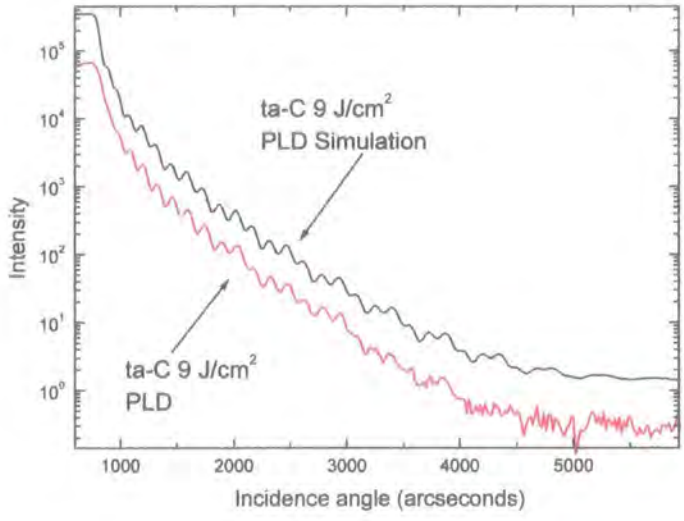

Fig. 4.6: X-ray reflectivity of a PLD ta-C film showing internal layering, compared to the simulated reflectivity.

On the other hand, the series of samples grown with the S-Bend FCVA shows a much higher uniformity (fig. 4.3) and only a weak dependence of density and layering on the substrate bias (Table 4.1). Surface layers never exceed 1-2 nm, and the film-substrate interface layer never exceeds 3 nm. The thickest surface layer, 2 nm, was detected for the film grown at –300V bias. The highest bulk density was 3.26 g/cm^3 (corresponding to 88% sp^3 content, at -100V bias). The high uniformity in these films was confirmed by Brillouin scattering measurements, since an optimum fit of the experimental data was obtained by considering the film as a single layer [49]. On the other hand, it was not possible to fit the Brillouin measurements of –80V films from the single bend FCVA if a single layer was assumed [49].

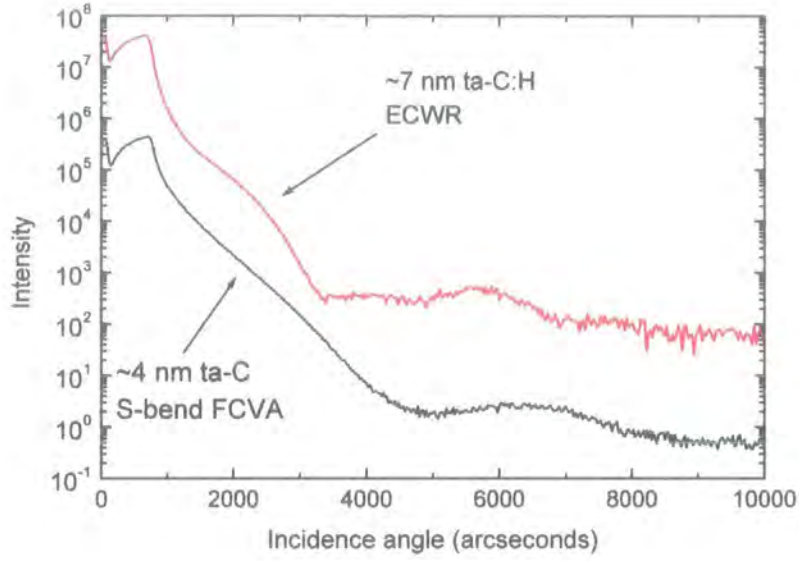

Fig. 4.7: X-ray reflectivity of ultrathin ta-C and ta-C:H films.

Fig. 4.7 shows XRR data on ultrathin ta-C and ta-C:H films, indicating the ease of XRR to measure films in the nm range. In particular, the structure of the thinnest ta-C, deposited at floating potential, consisted of 3-3.5 nm of 3.05-3.1 g/cm^3 density with a 0.5-0.8 nm surface layer of 2-2.5 g/cm^3 density and a 0.5-1 nm interface layer (see Table 4.2).

In Fig. 4.8, reflectivity curves from some of the films previously discussed are shown together with the simulated curves, obtained by using the Bede REFS-MERCURY simulation software package. The quality of the fits is affected mainly by parameters such as the bulk density, the total thickness, the surface and interface layer thickness, the surface roughness. On the other hand, the reflectivity curve (and thus the fitting procedure) is less sensitive to the density of the surface and interface layers and the roughness or grading between the layers, so that the error in the evaluation of these parameters is larger.

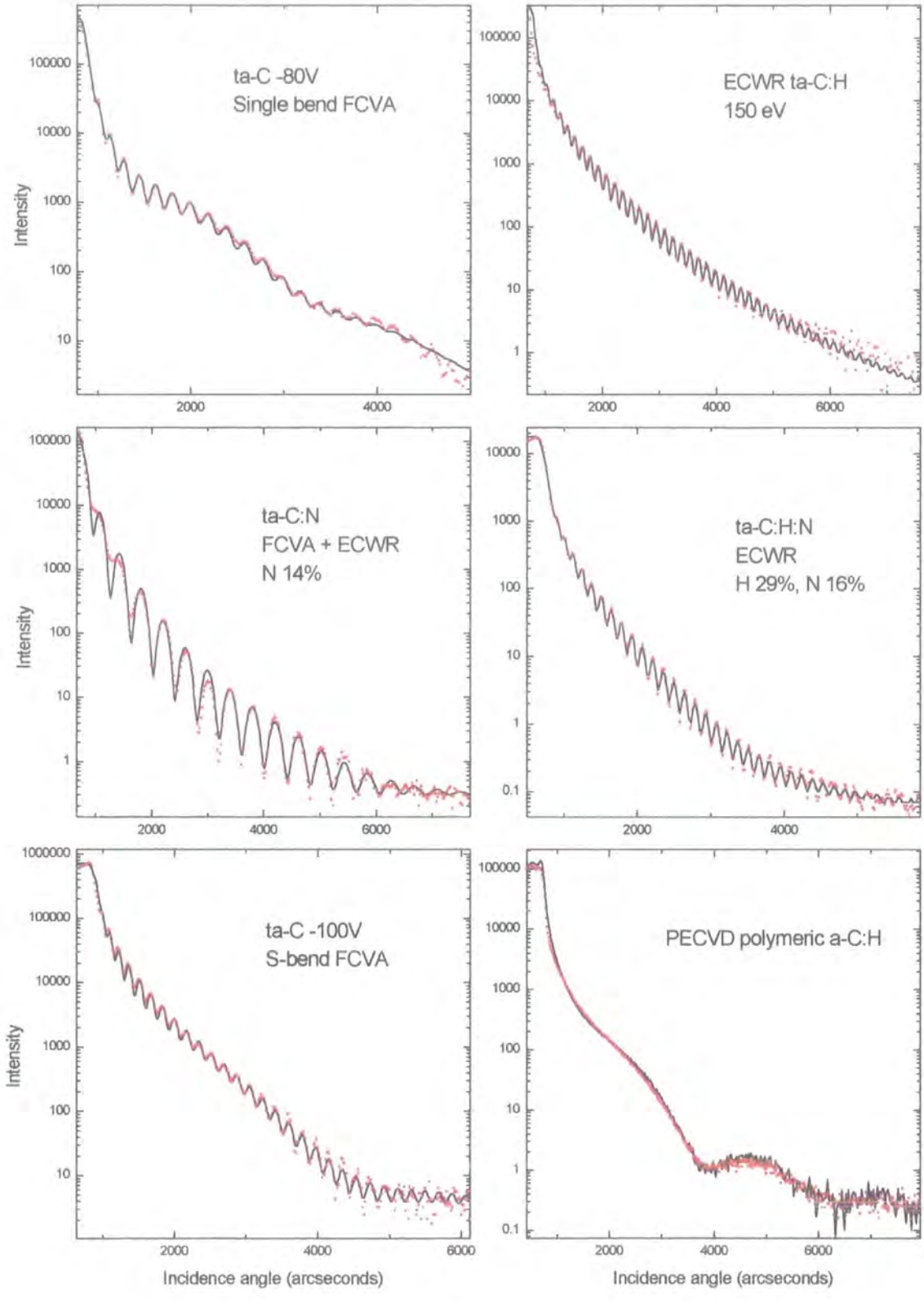

Fig. 4.8: Experimental (red dots) and simulated (black lines) reflectivity curves for some of the films discussed in section 4.4.1.1.

4.4.1.2 Etching

XRR was also used to study the effect of etching on ta-C films grown with the S-bend FCVA deposition system (bias -100 V, fig. 4.9). Etching has previously been tentatively used to remove small density surface layers, but we show that instead of removing them, new layering is produced. Two different types of etching were performed on the same film (in different regions of the deposition): with H_2 ions and with O_2 ions. Before etching the film was 76 nm thick, with a density of 3.26 g/cm^3 (determined by XRR); a small surface layer approximately 1 nm thick was probably present, with a lower density ($\cong$ 2 g/cm^3).

After O_2 etching, the thickness was measured to be 62 nm, with only a small surface layer 1.5 nm thick and 2.0 g/cm^3 dense. H_2 etching resulted in a film still 76 nm thick, but with a surface layer of 3.5 nm thickness, whose density was about 1.7 g/cm^3 (revealed by the strong modulation in the reflected intensity, see fig. 4.9).

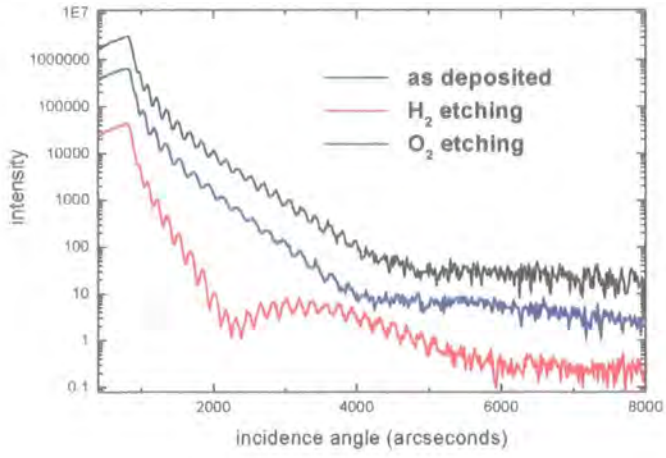

Fig. 4.9: Reflectivity curves from a ta-C S-bend FCAV film, as deposited and after H_2 and O_2 etching. The modulation in intensity in the H_2 etched film is due to a small density, 3.5 nm thick surface layer.

4.4.1.3 Roughness

XRR was used to measure atomic scale roughness. By combining specular and diffuse scatter, genuine surface roughness could be separated from compositional grading (i.e. smooth variations of density along the direction normal to the interface) [50], using Eq. (2.48):

$$\frac{I_{diff}}{I_{spec}} = \exp(q_z^2\sigma^2) - 1 \qquad (4.13)$$

Thus by measuring the integrated intensity of the diffuse and specular scatter in a transverse scan (fig. 4.10) the roughness of the surface could be deduced. Simulations show that in our films this method is sensitive mainly to the surface roughness, due to the small differences in electron density across internal interfaces.

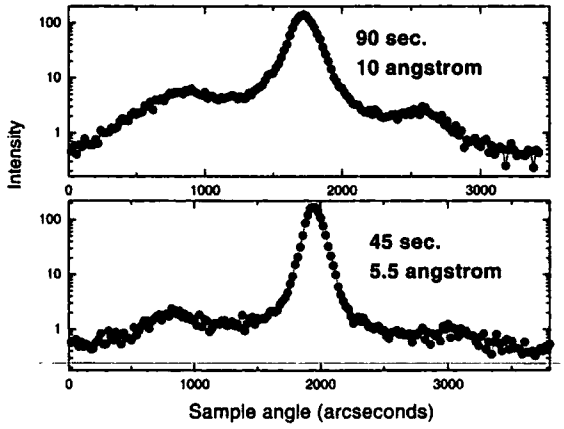

Fig. 4.10: Transverse diffuse scattering curves from two ta-C films grown with different deposition times. The detector angle (i.e. the scattering angle) is fixed, while the sample is rocked around the specular condition. The maximum correspond to specular reflection. It is possible to note that the diffuse scattered intensity increases in the thicker film, where the roughness is higher.

The top surface r.m.s. roughness was found to be in the range 5-10 Å for all the films (Tables 4.1, 4.2 and 4.4 below), and no relationship between the roughness and the deposition parameters could be found. The roughness of the nanostructured carbon film was too large (several tens of nm [19, 51]) to be determined quantitatively from Eq. (4.13) or within the distorted Born wave approximation.

To study the evolution of roughness as a function of thickness a series of films with increasing deposition times, from 20 s to 90 s, was prepared, using the single bend FCVA with -80 V bias. The r.m.s roughness increased with thickness, reaching a maximum at about 1 nm (Table 4.2).

4.4.1.4 Comparison of film uniformity

The hydrogenated DLC films consist mainly of a bulk layer with the possible presence of very thin Si/C and C/air interfaces. The cross sectional structure shows a

small dependence on the ion energy. Zhang *et al.* [40] reported the increase of surface and interface roughness (from 0.5 to 1.5 nm) and interface layer thickness (from 3 to 5 nm) for a-C:H deposited with increasing ion energy. On the other hand we found a difference in the cross sectional nanostructure of the two ta-C series grown with single bend and double bend FCVA (see figs. 4.2, 4.3, 4.4 and 4.5).

The films of the first series always consist of at least three layers of different densities, with a Si/C and C/air layers a few nanometers thick (up to 15 and 25 nm, according to HRTEM measurements by Siegal *et al.* [45] on a 55 nm film grown at –300V). Furthermore, the cross sectional structure is strongly dependent on the ion energy. FCVA films at -80V have always been considered ideal films, being the most dense and most highly sp^3 ones [10]. They are also the most uniform, consisting of the biggest bulk layer and of the smallest interfaces. Moving from -80V the sp^3 content does not change as drastically as the layering. Moreover the reflectivity curves of films deposited away from the optimum energy cannot be fitted satisfactorily only assuming different layers of fixed density, thus suggesting smooth interfaces with densities grading over a few nanometers inside each layer (as confirmed by HRTEM). Similar structures depending on ion energy are also revealed in ta-C films deposited with a completely different technique such as pulsed laser deposition [43, 44]. In this case, up to 4 layers with a "superdense" central layer were detected [43].

On the other hand double S-bend FCVA ta-C films showed a more uniform structure consisting of a high density bulk layer and two very small interface and surface layers, similarly to ta-C:H and a-C:H films. Finally, a significant surface layer was also found in the sputtered a-C film grown at much lower ion energy than ta-C.

These data indicate that it is possible to grow very uniform ta-C and that heavy layering does not necessarily occur but it is dependent on the particular deposition conditions employed. The S-bend FCVA apparatus works on the same principle as the single bend FCVA, the S bend only providing a better filtering of the macroparticles [12]. There is no fundamental physical reason why one machine should produce uniform films and the other extremely layered ones. Indeed, the layering dependence on deposition energy is not predicted by the simple subplantation theory [52, 53]. Siegal *et al.* [43] proposed the backscattering of C atoms from the Si substrate as responsible for the development of the bulk dense layer and of the interface layer, predicting the scaling of the interface layer with increasing ion energy. However, this mechanism cannot be a proper physical explanation for development of layers well

over 1 nm thick, which is the range of C ions at the usual 10-400 eV deposition energies [52]. The range is clearly even smaller for C atoms back-scattered at the Si substrate. This cannot also explain layers in sputtered a-C, grown at very low deposition energy. They also proposed that the less dense surface layer should originate to counteract the stress energy resulting from the growth process. However, layered and uniform ta-C films have comparable stresses of ~ 10 GPa, thus showing that no stress releasing induced layering is present. Note also that the structure of the ultrathin S-bend ta-C films (Table 4.2) resembles that of the thicker S bend films, with a scaling of the bulk layer, but not of the surface and interface layers (that are ~1 nm in both thick and thin films).

A hint towards an understanding of the real origin of the layering comes by considering the plasma in a FCVA or in an ECWR source. An ECWR plasma can be kept running with extreme stability for hours. A FCVA plasma is intrinsically less stable. Depositions in one run for more than 3-4 minutes cannot be done and the spot on the cathode moves during the deposition, sometimes requiring repositioning in the centre and re-striking the plasma. This results in plasma fluctuations. A first check was made on the possible influence of the triggering of the arc during ta-C deposition, by producing a film in one single strike or in more than one. As reported in [7], the structure was unchanged, suggesting that triggering in itself has a negligible role on the growth process. However, plasma instabilities and transients in ion energy and current density during the deposition could be responsible for the layering. A series of films was thus produced with increasing deposition times, from 20 s to 90 s, at –80V, using the single bend FCVA. A new cathode was used and extreme care in the positioning of the striker was taken during the deposition. As shown in table 4.2, no surface layer (<1 nm) was detected and only a ~2 nm interface layer was produced. We then grew another film at –250V; we still found a 4 nm thick top layer, but the layering was much smaller (Table 4.1) than in films previously grown at similar bias (single bend FCVA –200V, -290V). Furthermore Davis *et al.* [7] analysed, by cross sectional high resolution EELS, samples prepared at –300V with the same single bend FCVA and very uniform films were obtained (with 5 nm interface and 1 nm surface layers). McKenzie *et al.* also reported layering in their FCVA ta-C films, and they attributed it to plasma instabilities during growth [54].

Thus, we think that heavy layering is not an intrinsic property of ta-C and extremely uniform ta-C films can be grown at various bias voltages. There is no

physical mechanism that can explain less dense layers of the order of 10 nm at the surface or interface, if the ion energy and current densities are kept constant. Backscattering from Si could contribute only in the first 1-2 nm. Further work has to be devoted to better investigate the relation between layering and plasma instabilities and a feedback system should be required to minimise them. It is clear that a similar overall density and sp^3 content but different cross sectional nanostructure could give different tribological, mechanical, electrical and electronic behaviour. It is also clear that care should be taken whenever surface sensitive methods are compared to bulk methods.

4.4.2 Comparison with EELS

XRR should be the method of choice to measure the mass density in amorphous carbon films (at least for films that are not heavy layered). Not only it is superior to the plasmon energy approach, but also to other methods such as floatation measurements and RBS + profilometry, given the errors in these destructive and time-consuming measurements. Yet, EELS is still the standard choice for measurement of the sp^3 fraction, providing the plasmon energy at the same time. EELS gives also the X_C/X_N ratio that can be used in Eqs. (4.8) and (4.6) [16, 21].

Since XRR gives the total electron density and EELS the valence electron density, we can directly fit an average effective electron mass m^* for carbons, from our measured data. We did so for nitrogen free samples, to avoid the further problem of the number of valence electrons for N. Using the independent mass determination from XRR we thus obtain an effective electron mass that can be used to get a rough estimation of the density from the plasmon energy of all amorphous carbons. Considering X_N=0, we plotted the reduced density from XRR, $R = \rho_{XRR}(3X_C + 1)(11X_C + 1)^{-1}$, against the reduced density from EELS, $P = M_C \varepsilon_0 (12\hbar^2 N_A)^{-1} E_P^2$. If a unique m^* exists, then $R=(m^*/m_e)P$. We could fit the data in fig. 4.11 with a straight line with slope m^*/m_e=0.87.

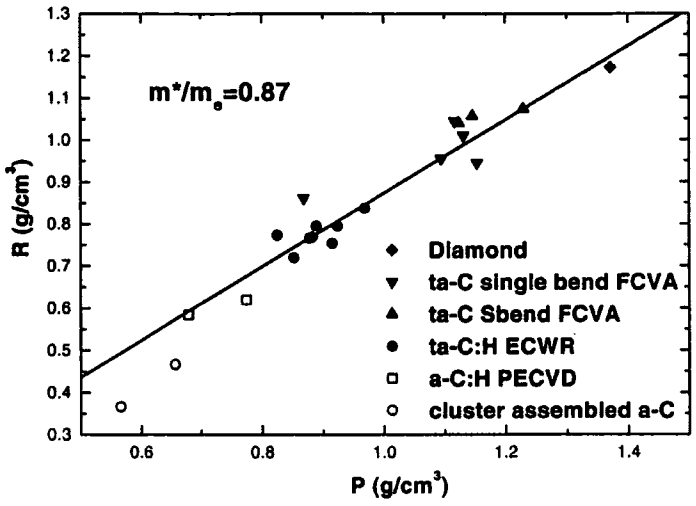

Fig. 4.11: Plot of reduced density of carbon films, from the valence plasmon energy and from XRR. The linear correlation allows an interband effective mass of $m^*=0.87m$ to be derived.

This is the first direct evidence of the existence of a common electron effective mass for diamond and all amorphous carbons. Indeed, our fitted effective mass gives E_P(diamond)~33.4 eV, in agreement with the measured value, within the 0.5 eV experimental error. The single effective mass thus permits density determinations via EELS. For ta-C:H:N samples a good agreement with XRR was obtained using the fitted m^* and 5 valence electrons, confirming in this case the assumption for Eq. (4.6). Corrections to the value of m^* only become important for high hydrogen contents, such as in polymeric a-C:H, where m^* is probably lower, about $0.7m_e$ (see [24]).

We can now give a relationship between sp^3 fraction and density, as shown in fig. 4.12, where our data, together with those of Weiler and Fallon [10, 55-57], are plotted, scaled with our fitted m^*. The H content of ta-C:H films is almost constant, between 25 and 30 at. %. Note that there is no common sp^3 density relationship for ta-C and ta-C:H, differently from what proposed by Weiler. The increase of the density and sp^3 fraction for a fixed H content is the main difference between ta-C:H and a-C:H, where the increase in sp^3 fraction is obtained through an increase in H content and, thus, a decrease in the density. Ta-C:H with higher H content will define lines parallel to the one in fig. 4.12. A series of a-C:H will give a line with an opposite slope with respect to ta-C or ta-C:H. A linear fit of the H free data gives:

$$\rho_x\ [\mathrm{g/cm^3}] = 1.92 + 1.37 \cdot x \qquad (4.14)$$

where x is the sp^3 fraction. Eq. (4.14) would give a lower density than diamond for 100% sp^3 content (3.3 g/cm^3), consistent with a random distribution of sp^3 bonds and the lower extrapolated elastic constants for the hypothetical 100% sp^3 ta-C [49].

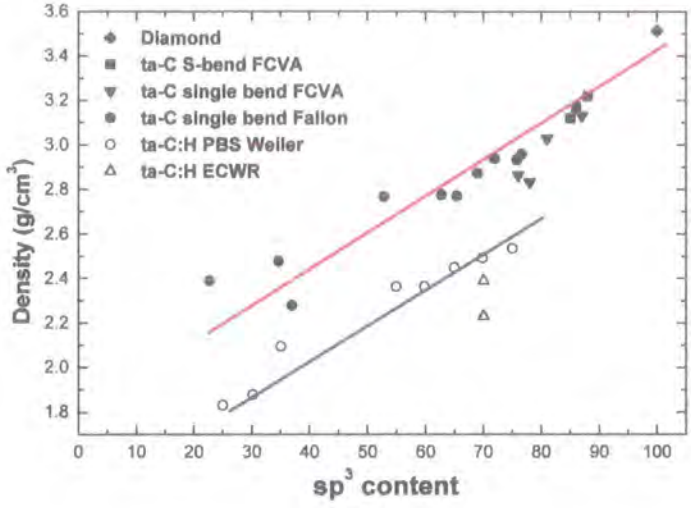

Fig. 4.12: Correlation of the density and sp^3 fraction for various amorphous carbon films, showing a nearly linear dependence for the two classes of films, ta-C and ta-C:H.

4.4.3 Hydrogen content

Combination of Eqs. (4.8) and (4.6) suggests a way to determine the H content, once the critical angle and plasmon energy are known. If we consider a N free sample, from Eqs. (4.8) and (4.6) we obtain:

$$X_H = \frac{4\delta\frac{\theta_C^2}{E_P^2} - 6}{3\delta\frac{\theta_C^2}{E_P^2} - 5} \tag{4.15}$$

with $\delta = \frac{4\pi^2 c^2 \hbar^2}{\lambda^2} \cdot \frac{m_e}{m^*}$. Using our fitted m^*/m_e we get $\delta \sim 9.0767 \cdot 10^7$ eV^2.

For a typical ta-C:H film, we found $\theta_c = 3.42 \cdot 10^{-3} \pm 2.5 \cdot 10^{-5}$ rad and $E_p = 27.12 \pm 0.5$ eV. This gives $X_H = 33^{+25}_{-50}$ at. %. The reason for the large error bars is clear. XRR is very insensitive to the H content. EELS is more sensitive, but the plasmon energy is determined with a much bigger experimental error than the XRR critical angle. Thus the information about the H content lies in the less precise technique. Moreover, the error bars connected with the m^*/m_e fit introduce further scatter in the data. Eq. (4.15)

can thus be used to obtain a qualitative estimate of H content but it cannot give quantitative information.

An alternative way to ERDA (Electron Recoil Detection Analysis) could be the coupling of XRR and Hydrogen effusion analysis. In fact, H effusion gives the total number of H atoms/cm^2 [58]. XRR gives density and thickness. From Eq. (4.8) we get:

$$X_H = \frac{6\frac{N_H}{t}}{\frac{\pi^2 c^2 \varepsilon_0}{3\lambda^2 e^2} M_C m_e \theta_c^2 + 5\frac{N_H}{t}} \qquad (4.16)$$

where N_H [H atoms/cm^2] is derived from H effusion, and t is the film thickness from XRR.

H effusion measurements were performed at the University of Cambridge on a series of ta-C:H ECWR films grown at different ion energies. We applied Eq. (4.16) and the results are shown Table 4.4.

Table 4.4: Critical angle, density, thickness, H content and roughness of the films mesured by H effusion and XRR.

Sample	Critical angle (arcseconds)	Density (g/cm^3)	Thickness (Å)	H content (%)	r.m.s. surface roughness (±1 Å)
ta-C:H 06	705±10	2.15±0.06	540	32	5
ta-C:H 16	710±10	2.20±0.06	810	25	6
ta-C:H 10	598±7	1.53±0.035	700	38	5
ta-C:H 11	607±7	1.57±0.035	820	39	5
ta-C:H 12	602±7	1.55±0.035	890	39	6

4.5 Conclusions

A wide variety of pure, hydrogen- and nitrogen-containing amorphous carbon films have been analysed via x-ray reflectivity. XRR was shown to be the method of choice to measure their density and cross-sectional nanostructure. We were able to correlate most of these properties with the source configuration adopted. By comparing XRR and EELS data we have been able to fit a common effective mass for all amorphous carbons and diamond, validating the Jellium approach to density from plasmon energy. We have thus shown the correct general relationship between sp^3 content and mass density for ta-C and ta-C:H films.

The cross-sectional structure of hydrogenated films was found to be quite uniform, with the presence of less than 1-2 nm interface and eventually surface layers. On the other hand, ta-C films can possess a heavily layered structure depending on the deposition conditions. However, layering is not intrinsic, but it is due to plasma instabilities in the arc, and uniform films can be grown.

The S-bend FCVA deposition system was found to produce the most uniform ta-C films. Plasmon energy measurement is convenient to get the average density of heavily layered films when fitting of the XRR data is difficult.

XRR was also used to study the structure of ultra-thin carbon films, the effect of etching and the evolution of surface roughness as a function of thickness.

Although the combination EELS+XRR could be used to get the H content, the error bars in determining the plasmon energy and in fitting the effective mass do not allow a reliable quantitative evaluation. On the other hand, a combination of XRR and H effusion provides a precise measure of the H content.

The fast, non-destructive and simple structural characterisation allowed by the use of this technique is of great value. In our particular case, information provided by XRR is being used to analyse and model Brillouin scattering experiments for the determination of the film elastic constants [49, 59]. We believe that the thorough investigation here presented can open the possibility of a standard use of this technique in carbon film characterisation.

References for Chapter 4:

[1] B. Bhushan, Diam. Rel Mat. **8**, 1985 (1999)

[2] J. Robertson, Adv. Phys. **35**, 317 (1986); J. Robertson, Prog. Solid State Chem. **21**, 199 (1991)

[3] J. Robertson, Current Opinion in Solid State & Materials Science **4**, 557 (1996)

[4] D.R. McKenzie, Rep. Prog. Phys. **59**, 1611 (1996)

[5] S. Aisenberg, R. Chabot, J. Appl. Phys. **42**, 2953 (1971)

[6] I.I. Aksenov, V.A. Belous, V.G. Padalka, V.M. Khoroshikh, Sov. J. Plasma Phys. **4**, 425 (1978)

[7] C.A. Davis, K.M. Knowles, G. A. J. Amaratunga, Surf. Coat Tech, **76-77**, 316 (1995); Phys. Rev. Lett. **80**, 3280 (1998)

[8] A. Libassi, A. C. Ferrari, V. Stolojan, B. K. Tanner, J. Robertson, Diamond Relat. Mater. **9**, 771 (2000)

[9] D.R. McKenzie, D. Muller, B.A. Pailthorpe, Phys. Rev. Lett **67**, 773 (1991)

[10] P.J. Fallon, V.S. Veerasamy, C.A. Davis, J. Robertson, G.A.J. Amaratunga, W.I. Milne, J. Koskinen, Phys. Rev. B **48**, 4777 (1993)

[11] J. Schwan, S. Ulrich, T. Theel, H. Roth, H. Ehrhardt, P. Beker, S.R.P. Silva, J. Appl. Phys. **82**, 6024 (1997)

[12] M.C. Polo, J.L. Andujar, A. Hart, J. Robertson, W.I. Milne, Diamond Relat. Mater. **9**, 663 (2000).

[13] M. Bonelli, A.C. Ferrari, A.P. Fioravanti, A. Miotello, P.M. Ossi, Mat. Res. Soc. Symp. Proc. **593** (2000)

[14] N.A. Morrison, S.E. Rodil, A.C. Ferrari, J. Robertson, W.I. Milne, Thin Solid Films, **337**, 71 (1999)

[15] N.M.J. Conway, A. Ilie, J. Robertson, W.I. Milne, A. Tagliaferro, Appl. Phys. Lett. **73**, 2456 (1998)

[16] S.E. Rodil, N.A. Morrison, J. Robertson and W.I. Milne, Phys. Stat. Sol. A, **174**, 25 (1999)

[17] S.E. Rodil, W.I. Milne, J. Robertson, L.M. Brown, submitted to Appl. Phys. Lett. (2000)

[18] X.L. Peng, T.W. Clyne, Thin Solid Films **312**, 207 (1998)

[19] E. Barborini, P. Piseri, A. Libassi, A.C. Ferrari, C.E. Bottani, P. Milani, Chem. Phys. Lett. **300**, 633 (1999)

[20] D. McMullan, P.J. Fallon, J. Ito, A.J. McGibbon, "Electron Microscopy", vol 1, EUREM 92, Granada, Spain (1992), p.103

[21] R. F. Egerton, "Electron Energy Loss Spectroscopy in the Electron Microscope", Plenum, New York (1986)

[22] S.D. Berger, D.R. McKenzie, P.J. Martin, Phil. Mag. Lett. **57**, 285 (1988)

[23] N.K. Menon, J. Yuan, Ultramicroscopy **74**, 83 (1998); N.K. Menon, Ph.D. Thesis, Cambridge University (1998)

[24] A.C. Ferrari, A. Libassi, B.K. Tanner, V. Stolojan, J. Yuan, L. M. Brown, S. E. Rodil, B. Kleinsorge, J. Robertson, Phys. Rev. B **62**, 11089 (2000)

[25] V. Stolojan, L.M. Brown, A.C. Ferrari, J. Robertson, A. Li Bassi, B.K. Tanner, Institute Of Physics Conference Series **161**, 361 (1999)

[26] D.G. McCulloch, E.G. Gernstner, D.R. McKenzie, S. Prawer, R. Kalish, Phys. Rev. B, 52 850 (1995)

[27] E. Kondrashov, I.S. Smirnov, E.G. Novoselova, S.Y. Yablokov, A.M. Baranov, Diamond Relat. Mater. 6, 1784 (1997)

[28] A.M. Baranov, Surf. Coat. Techn. 102, 154 (1998)

[29] A.M. Baranov, I.F. Mikhailov, Thin Solid Films 324, 539 (1998)

[30] S. Logothetidis, G. Stergioudis, Appl. Phys. Lett. 71, 2463 (1997)

[31] S. Logothetidis, M. Gioti, C. Lioutas, Carbon 36, 539 (1998)

[32] M. Gioti, S. Logothetidis, C. Charitidis, Appl. Phys. Lett. 73, 184 (1998)

[33] S. Logothetidis, G. Stergioudis, N. Vouroutzis, Surf. Coat. Techn. **101**, 486 (1998)

[34] A. Lucas, T.D. Nguyen, J.B. Kortright, Appl. Phys. Lett. **59**, 2100 (1991)

[35] M.J. Grundy, R.M. Richardson, J. Roser, G. Beamson, W.J. Brennan, J. Howard, M. O'Neil, J. Penfold, C. Shackleton, C. Ward, Thin Solid Films **172**, 269 (1989)

[36] E. Findeisen, R. Feidenhans'l, M.E. Vigild, K.N. Clausen, J. Bindslev Hansen, M.D. Bentzon, J.P. Goff, J. Appl. Phys. **76**, 4636 (1994)

[37] F. Toney, S. Brennan, J. Appl. Phys. **66**, 1861 (1989)

[38] Y. Huai, M. Chaker, J.N. Broughton, E. Gat, H. Pepin, T. Gu, X. Bian, M. Sutton, Appl. Phys. Lett. **65**, 830 (1994)

[39] Q. Zhang, S.F. Yoon, Rusli, J. Ahn, H. Yang, D. Bahr, J. Appl. Phys. **84**, 5538 (1998)

[40] Q. Zhang, S.F. Yoon, Rusli, J. Ahn, H. Yang, D. Bahr, J. Appl. Phys. **86**, 289 (1999)

[41] J. Martinez-Miranda, J.P. Sullivan, T.A. Friedmann, M.P. Siegal, N.J. DiNardo, Mat. Res. Soc. Symp. Proc. **498**, 55 (1998)

[42] B.K. Tay, X. Shi, S.P. Lau, Q. Zhang, H.C. Chua, J.R. Shi, E.C. Lim, H.Y. Lee, Int. J. Mod. Phys. B 14, 181 (2000)

[43] M.P. Siegal, J.C. Barbour, P.N. Provencio, D.R. Tallant, T.A. Friedmann, Appl. Phys. Lett., **73**, 759 (1998)

[44] M.P. Siegal, D.R. Tallant, L.J. Martinez-Miranda, J.C. Barbour, R.L. Simpson, D.L. Overmyer, Phys. Rev. B, **61**, 10451 (2000)

[45] M.P. Siegal, P.N. Provencio, D.R. Tallant, R.L. Simpson, B. Kleinsorge, W.I. Milne, Appl. Phys. Lett., **76**, 2047 (2000)

[46] B.L. Henke, E.M. Gullikson, J.C. Davis, "X-ray interactions: photoabsorption, scattering, transmission, and reflection at E=50-30000 eV, Z=1-92", Atomic Data and Nuclear Data Tables **54**, 181 (1993)

[47] G.H. Vineyard, Phys. Rev. B **26**, 4146 (1982)

[48] R.J. Rigden, R.J. Newport, G. Bushnell-Wye, J. Mater. Res. **12**, 264 (1997)

[49] A.C. Ferrari, J. Robertson, M.G. Beghi, C.E. Bottani, R. Ferulano, R. Pastorelli, Appl. Phys. Lett. **75**, 1893 (1999)

[50] D.E. Savage, J. Kleiner, N. Schimke, Y.H. Phang, T. Jankowsky, J. Jacobs, R. Kariotis, M.G. Legally, J. Appl. Phys. **69**, 1411 (1991)

[51] R. Buzio, E. Gnecco, C. Boragno, U. Valbusa, P. Piseri, E. Barborini, P. Milani, Surface Science **444**, L1 (2000)

[52] Y. Lifshitz, S.R. Kasi, J.W. Rabalais, W. Eckstein, Phys. Rev. B **41**, 10468 (1990)

[53] J. Robertson, Diamond. Relat. Mater. **2**, 984 (1993)

[54] D.R. McKenzie, E.G. Gernstner, D.G. McCulloch, A.R. Marchant, in "Amorphous Carbon: State of the Art", ed. by S.R.P. Silva, J. Robertson, W.I. Milne and G.A.J. Amaratunga, Word Scientific, Singapore (1998), p. 1

[55] M. Weiler, S. Sattel, T. Giessen, K. Jung, H. Ehrhardt, V.S. Veerasamy, J. Robertson, Phys. Rev. B **53**, 1594 (1996)

[56] M. Weiler, R. Kleber, S. Sattel, K. Jung, H. Ehrhardt, G. Jungnickel, S. Deutschmann, U. Stephan, P. Blaudeck, T. Frauenheim, Diamond Relat. Mater. **3**, 245 (1994)

[57] M. Weiler, PhD Thesis, Universitat Kaiserslautern (1994)

[58] J. Ristein, R.T. Stief, L. Ley, W. Beyer, J. Appl. Phys. **84**, 3836 (1998)

[59] R. Pastorelli, A.C. Ferrari, M.G. Beghi, C.E. Bottani, J. Robertson, Diam. Rel. Mater. **9**, 825 (2000)

Chapter 5

Raman and Brillouin scattering from cluster-assembled carbon films

5.1 Introduction

As a consequence of their peculiar structural, electronic, and mechanical properties [1], nanostructured materials are the subject of an increasing interest (see chapter 1). Among many methods of production of nanostructured materials [2] the assembling of clusters is very attractive, particularly for thin film synthesis. This is due to the possibility of correlating the final product with the properties of the precursors and so building a material with the required characteristics (for example nanostructured thin films where the original cluster structure is partially preserved after the deposition [3-6]).

Several authors have proposed deposition by cluster beams as a tool for the synthesis of nanostructured thin films [6-10]. Intense and stable beams must be obtained with a good control of cluster mass and kinetic energy distribution. These characteristics can be obtained with the use of beams produced by supersonic expansion. Clusters produced in the gas phase are accelerated in a supersonic beam and then deposited on a substrate.

As pointed out in chapter 1, the deposition of carbon clusters for thin film synthesis is very promising, due to the extreme versatility of carbon and to the possibility of controlling its properties by tuning the cluster size and kinetic energy distributions, in order to deposit materials with tailored properties.

In the Nanoaggregates Laboratory at the University of Milan (LaMiNA) a novel plasma cluster source (PMCS: Pulsed Microplasma Cluster Source) has been designed and characterised in the past few years [5, 6, 10-14]. This source can produce cluster beams of any refractory material. In particular, by using pulsed supersonic carbon cluster beams, thin carbon films can be grown at high deposition rates. Due to inertial separation effects, typical of supersonic seeded beams, the cluster mass distribution can be varied to deposit films with a controlled nanostructure. The deposited carbon films

have been characterised by a number of different techniques [5, 10, 11, 15-25], such as scanning electron microscopy (SEM), atomic force microscopy (AFM), Raman and Brillouin spectroscopy, optical reflectance and ellipsometry, Near-Edge X-ray Absorption Spectroscopy (NEXAFS), X-ray Photoelectron Spectroscopy (XPS), Electron Energy Loss Spectroscopy (EELS) and X-Ray Reflectivity (XRR). The analysis of the carbon films shows that, in the deposition energy range used, they have a nanoporous/ball-assembled structure, with an essentially sp^2 character to the bonds. This structure has also been predicted by theoretical studies [26]. NEXAFS and XPS measurements have shown that the sp^2 content is always higher than 60%, and that the sp^3 fraction, if present, does not exceed 20%. The high surface roughness has been studied by AFM [17], and found to be increasing with thickness (20-200 nm for thickness in the range 100-1000 nm). The source performance and the cluster beam prior to deposition have also been characterised carefully.

Possible applications of these films have been investigated. Nanostructured forms of carbon possess field emission properties ([25] and references therein), which can render the material suitable for application in flat panel display devices. Moreover, the high degree of roughness and the nanoporous character mean that the specific area is huge. This could open the possibility of using this material for hydrogen storage or even as the building material for electrodes in supercapacitor devices [18].

In this chapter it is demonstrated how Raman scattering and Brillouin scattering can be used to study the deposited films and understand the correlation between the cluster size distribution and the beam characteristics on one side and the deposited material on the other.

5.2 Sample deposition apparatus

A supersonic beam can be schematically described as a gas stream expanding very rapidly from a high-pressure region source to a low-pressure region through a nozzle. The characteristics of the beam are mainly determined by the size and shape of the nozzle orifice and by the pressure difference between the two regions [27]. Compared to effusive beams used in Molecular Beam Epitaxy, supersonic beams provide higher intensity and directionality allowing the deposition of films with very high growth rates [28, 29].

A schematic view of the deposition apparatus is shown in fig. 5.1. It consists of three differentially evacuated chambers and operates in the high-vacuum regime.

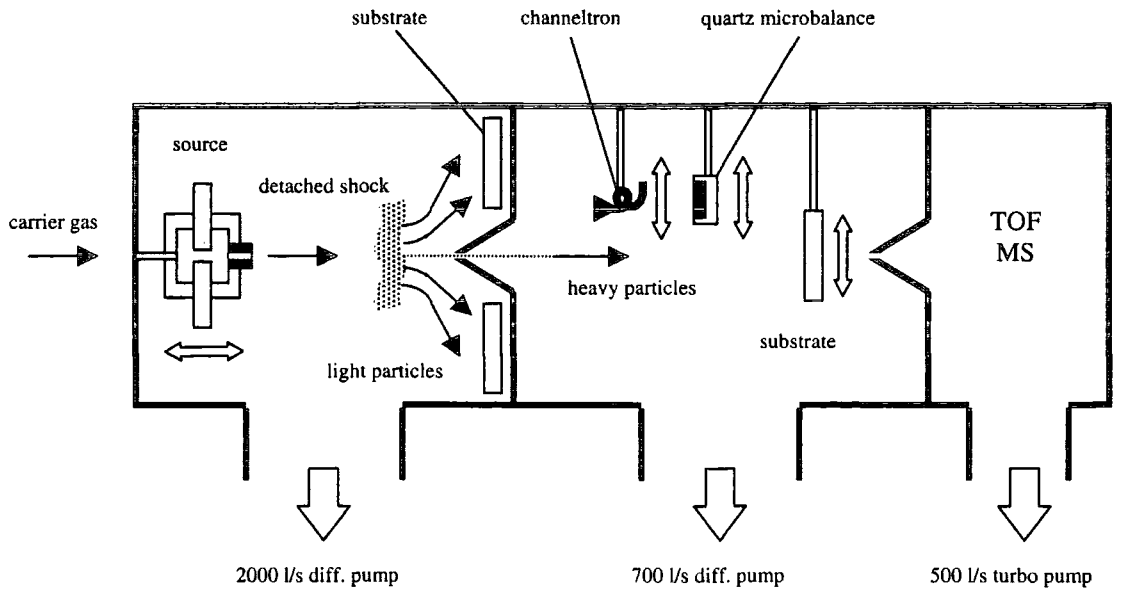

Fig. 5.1: Scheme of the cluster-assembled carbon film deposition apparatus. The source is in the first chamber; deposition takes place in the second chamber. The third chamber hosts a TOF Mass Spectrometer for beam characterisation.

The cluster source is placed in the first chamber, where the typical base pressure is about 10^{-7} torr; during source operation the average pressure is in the range $1 \cdot 10^{-5}$ – $3 \cdot 10^{-5}$ torr. The supersonic cluster beam then enters the second chamber through an electroformed skimmer of 2 mm diameter. The second chamber is equipped with a sample holder that can intersect the beam, a quartz microbalance for beam intensity monitoring, and can alternatively host a beam-chopper or a Fast Ionization Gauge for time-of-flight measurements of the velocity distribution of particles in the beam. During deposition the background pressure in this chamber is about 10^{-7} torr. The third chamber hosts a linear time-of-flight mass-spectrometer (TOF/MS), collinear to the beam axis [14]. The detector of the TOF/MS is sensitive to high-speed neutral clusters as well as to ions [13].

The cluster source is a PMCS (Pulsed Microplasma Cluster Source), a modified version of the Pulsed Arc Cluster aggregation Ion Source (PACIS) [30]) and it works on the principle of vaporising the material used for cluster production with a pulsed electric discharge. A schematic cross-section of the source is sketched in fig. 5.2. Two graphite electrodes are facing each other in a small cavity inside the ceramic body of the source. A pulsed valve injects a buffer gas (helium) in the cavity just before an

electric discharge takes place between the electrodes. The discharge, driven by a high voltage (between 500 and 1500 V), is very intense (1000 A) and lasts a few tens of microseconds, producing the ablation of the cathode material. This is quenched by He and condenses in clusters, which are carried out of the source in a seeded supersonic expansion through a nozzle of 2 mm diameter and 8 mm length. The presence of the gas favours thermalization in the cavity and cluster aggregation. During typical operation the average pressure inside the cavity is several hundred Torr and the source body reaches a temperature of about 400 K. The temperature of the carrier gas evolves rapidly down to about 100 K as expansion takes place and the source empties. The velocity of the carrier gas is about 2000 m/s when the first clusters come out of the nozzle, but slows down to about 1000 m/s towards the end of the cluster pulse. A velocity slip of the clusters with respect to the carrier gas is also present but is of some relevance only for clusters exiting late from the source, when the stagnation pressure is reduced. The use of a cavity, where cluster aggregation occurs (the residence time is a few ms), is beneficial for several reasons [10, 31]. The erosion of the cathode does not affect significantly the dynamics of the gas during the expansion; moreover the presence of the cavity itself decouples the cathode sputtering from the cluster formation process. The stability of the source is substantially improved and electrode erosion affects mainly the intensity but not the mass distribution of the clusters. During the residence time further growing takes place (e.g. cluster-cluster coalescence), so that large particles with complicated shapes may be formed.

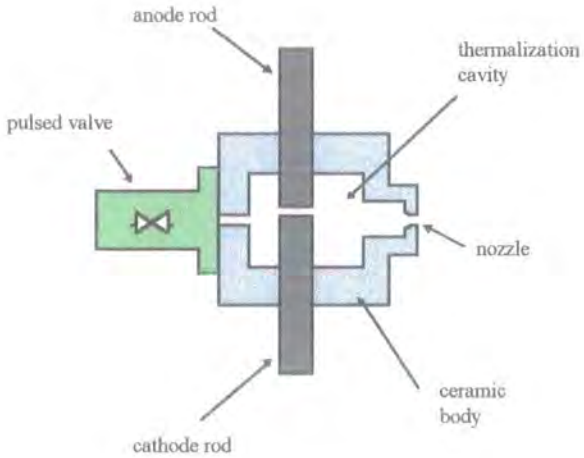

Fig.5.2: Schematic cross-section of the cluster source.

The characterisation of the cluster mass distribution and charge states in the beam has been performed with a linear time-of-flight (TOF) mass spectrometer [14], while cluster fluxes have been characterised with the quartz microbalance and with a Faraday cup. With typical discharge conditions, a lognormal cluster mass distribution in the range of 0–2500 atoms/clusters is obtained, with its maximum at about 400-500 atoms/cluster and average size at about 900-1000 atoms/cluster (fig. 5.3). The centre of mass of the size distribution and the charge state are strongly influenced by the presence of the thermalization cavity; mass distribution and energy are influenced by the residence time of the clusters in the cavity, which in turn depends on parameters such as the maximum pressure reached in the cavity, its volume, and the conductance of the nozzle. The mass distribution of cluster ions (cations) is substantially different from that of neutrals, and it is in the range 0-1200 atoms/cluster (with a mass distribution centred at 350 atoms/clusters). This is probably due to a trade off between cluster growth and charge neutralisation; the growth of large clusters requires long residence times inside the source, but this increases the chance of being neutralised.

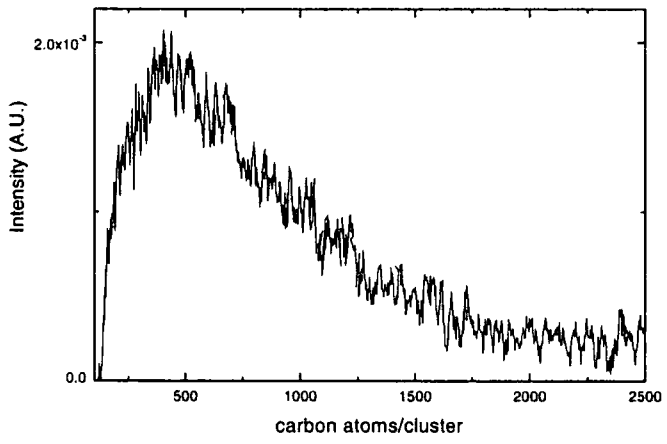

Fig. 5.3: Typical mass distribution of carbon clusters used as precursors of thin films.

By growth rate measurements, performed with the quartz microbalance, the overall beam intensity has been estimated to be in the range of $\approx 3 \cdot 10^{14}$-$1 \cdot 10^{15}$ particles s^{-1} sr^{-1} (depending on the source parameters such as the discharge voltage). A fraction of about 10% of the total average flux is due to anions, while cations are about 2%. The typical kinetic energy of an average-size cluster is thus about 0.3 keV. This means a typical value of energy per atom lower than 0.2 eV/atom, well below the binding energy of carbons in the cluster. At cluster impact on the substrate surface there is thus

no substantial fragmentation of the aggregates. Of course coalescence and aggregation processes take place during deposition, nevertheless the deposited films may keep a memory of the structure which the clusters had in the gas phase [3-6]. The source–skimmer distance D_{sk} and the background pressure strongly affect the expansion. Depending upon D_{sk} a shock wave can be produced in front of the skimmer, causing mass separation effects and changing the final characteristics of the beam [27, 32]. In usual experiments, the nozzle–skimmer distance has been varied from 40 to 16 mm. With D_{sk} = 40 mm deposition rates of 5 nm/min are routinely obtained on a substrate placed at 300 mm from the source (even rates up to 50 nm/min can be achieved with the help of a particular device called a "focuser", see below). Circular films with 1 cm radius and uniform thickness can be deposited in the second chamber of the apparatus. By intersecting the beam in the first chamber with a larger substrate, films with an area of several cm^2 can be prepared with an approximately gaussian thickness profile.

In fig. 5.4 we show SEM micrographs of the cluster-assembled films. Micrographs of the films were taken with a Cambridge Stereoscan 360 scanning electron microscope with a 5 kV SEM acceleration and a 150 pA probe current by the LaMiNA group.

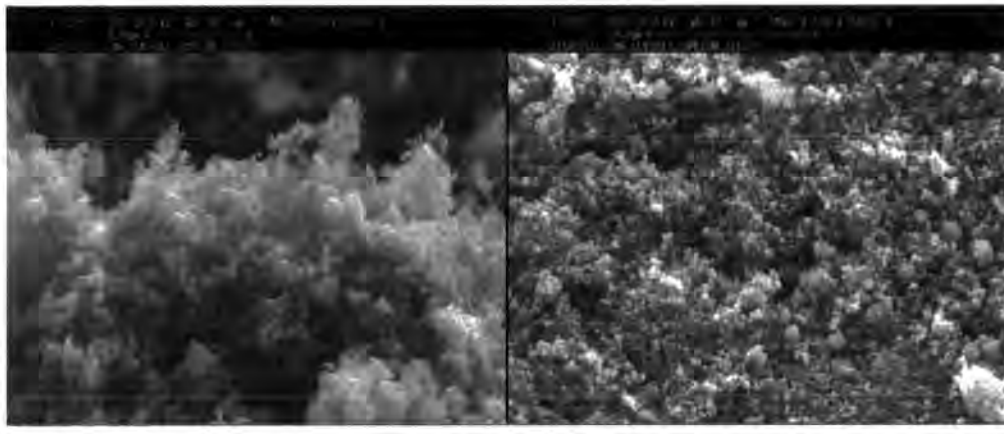

Fig.5.4: SEM micrograph of the surface of typical cluster-assembled carbon films, at different magnification (courtesy Emanuele Barborini, LaMiNA, Milano).

An AFM picture (fig. 5.5) shows the granular structure based on clumps of spherical aggregates with typical diameter of few tens of nanometers.

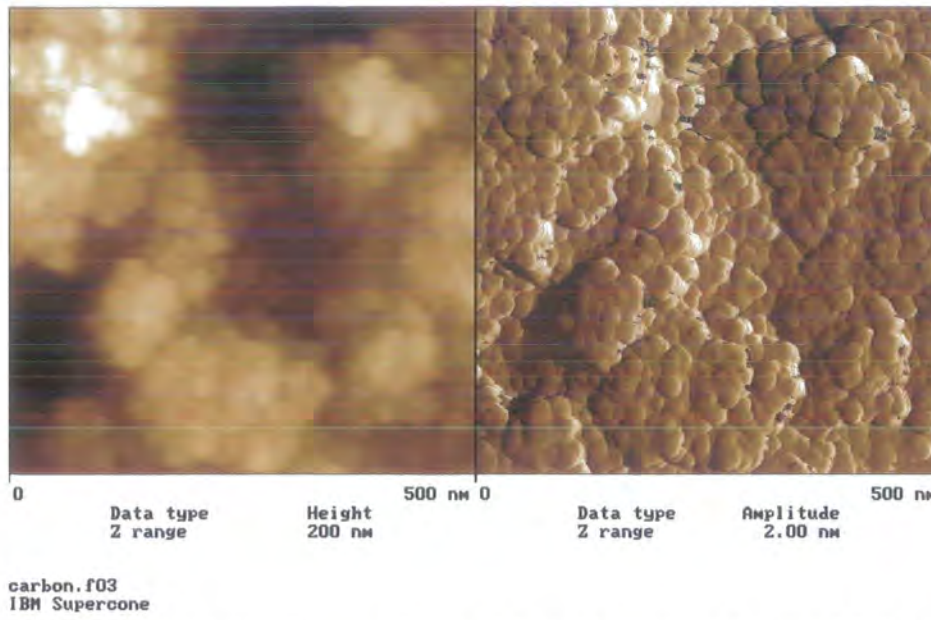

Fig. 5.5: AFM image (left) and contrast image (right) of the surface of a typical film (courtesy Alessandro Podesta', LaMiNA).

It has been reported that if species with different weights are present in the gas to be expanded, the heavier constituents concentrate along the core of the beam [27, 33-36]. We shall call this effect inertial separation or focusing. Different mechanisms have been proposed to account for this effect. Waterman and Stern have suggested that the flux of lighter species diverges radially more rapidly after the nozzle due to the greater thermal velocity component [35]. Reis and Fenn [33] have shown that mass separation can be obtained by exploiting the interaction of the beam with the shock wave detached from the skimmer. In particular, due to their different inertia, light species follow diverging streamlines after the shock front, while heavy species are not diverted and can follow straight trajectories through the skimmer (see fig. 5.1). Due to this effect large clusters are concentrated in the central portion of the beam, whereas the lighter ones are at the periphery.

Thin film deposition has been performed by intersecting the cluster beam with the substrate placed on a 3-axis micromanipulator. The temperature of the substrate (Si, Al, Ag) can be controlled from 77 to 600 K. A mechanism has been designed in order to tilt the source axis with respect to the skimmer axis, so that only selected portions of the beam can enter the second chamber. Thus, clusters with a more uniform size distribution (bigger sizes from the centre of the beam or smaller sizes from the

periphery of the beam) can selectively be deposited with uniform thickness over an area of some cm^2. Selection of the cluster size distribution can also be achieved by changing some operational parameters in the source (e.g. gas pressure and nozzle diameter, and thus residence time in the cavity).

Finally, a device, called a "focuser", has been designed and built in order to achieve a filtering effect (e.g. a selection of only the very small clusters), and a low divergence of the beam at the exit of the ceramic body of the source [37]. The device is based on a particular design of the source nozzle and very narrow, low-divergence beams can be obtained (the angular divergence is less than 1°, compared to a divergence of about 12° for non-focused beams). The effect of this device is to enormously increase the inertial separation effect, normally occurring in molecular beams, by forcing the clusters through particular trajectories inside the nozzle, thus selecting only the very small clusters along the axis of the beam. Thus, very high deposition rates can be achieved (up to ten times with respect to the non-focused beam), and compact, close packed films can be deposited. These turned out to be much smoother than films grown in standard conditions. Moreover, not only space focusing, but also an "energy focusing" effect is obtained, i.e. a more effective cooling of the particles in the beam (their transverse velocity with respect to the axis of the beam is lower and this contributes to the compactness of the films). Thus, not only the bonding topology, but also the mesoscopic structure and the surface morphology can be varied by tuning the source deposition setting.

In the following sections Raman scattering characterisation of cluster-assembled films is presented, in order to correlate the bonding topology in the films with the size of the clusters, in relation to the study of the inertial separation effect. Raman scattering has also been employed to study the products of the arc discharge between the electrodes, in order to clarify some aspects of the ablation process. It is then shown how Brillouin scattering can be used to study the elastic properties of the films and to evidence the differences in the films produced with and without the "focusing" device. Confined, non-propagating vibrational modes due to the disordered, discontinuous nature of the films were detected. X-ray scattering techniques have also been used (XRR to study the density of the films, WAXS to test their amorphous nature, SAXS to verify their possible fractal nature).

5.3 Raman scattering from cluster-assembled carbon films

Raman scattering is widely employed as a standard tool for amorphous carbon characterisation. The principal features detected in amorphous carbon Raman spectra and their interpretation will be discussed in the next subsection. In this section it will be shown how Raman scattering has been used to characterise, at a nanometer scale, the different types of carbon films that the cluster beam source is able to produce due to a selection of the deposited clusters. Raman spectroscopy has also been useful in the characterisation of the source operation, of the cluster growth mechanisms and of the beam structure. It has been possible to:

- show that the clusters in the beam have a different size and nature depending on their distance from the axis of the beam (inertial separation or focusing);
- deposit films with different local bonding properties by selecting the precursor clusters and so demonstrate a memory effect in the deposition of cluster-assembled carbon films (i.e. the film bonding topology follows the cluster size);
- show that the "focusing" device produces beams which are uniform in terms of cluster composition;
- characterise the plasma products inside the thermalization chamber. This has helped to understand the electrode ablation processes.

Moreover, Raman measurements have been performed on all the deposited films for a standard and fast characterisation of the produced material, a sort of fingerprint of the film. Power density on the sample has always been kept under 10 W/cm^2 to avoid damage or graphitization. For this reason spectra were acquired without use of microscope objectives. The spectral region from 300 cm^{-1} up to 3400 cm^{-1} has usually been recorded.

5.3.1 Raman scattering from carbon and fitting of carbon spectra

Raman spectroscopy is a standard non-destructive tool for the characterisation of crystalline, nanocrystalline and amorphous carbons (for a complete discussion refer to [38-61]). The Raman spectrum of diamond consists of the T_{2g} 1332 cm^{-1} zone centre

mode. The Raman spectrum of disordered graphite shows two rather sharp modes, the so-called G (from Graphite) peak at about 1580-1600 cm^{-1} and the D (from Disorder) peak around 1350 cm^{-1}. They are usually assigned to the zone centre phonons of E_{2g} symmetry and to the K-point phonons of A_{1g} symmetry (activated due to disorder-induced relaxation of the $\mathbf{q} \approx \mathbf{0}$ selection rule), respectively. These features also dominate the Raman spectra of nanocrystalline and amorphous carbons. In amorphous carbon, the Shuker and Gammon formula [62] applies (Eq. (2.14)). The Raman spectrum is thus directly related to the vibrational or phonon density of states (PDOS) of the material. The PDOS of an amorphous carbon is different from that of graphite, so it is not correct to say that the G and D peak come from maxima in the graphite PDOS. Visible Raman spectroscopy is about 200 times more sensitive to sp^2 sites, since visible photons preferentially excite their π states, while uv Raman excites both π and σ states and thus can probe both the sp^2 and the sp^3 sites, allowing a direct measurement of the sp^3 fraction, which is not possible with visible Raman spectroscopy. So visible Raman spectroscopy is sensitive mainly to the sp^2 phase present in the material, and to its PDOS as modified by the degree of disorder.

The G peak origin lies in the stretching vibration of two neighbouring sp^2 bonded atoms. It is thus visible also in carbons where 6-fold graphitic rings are not present. Recent studies have explained the origin of the D peak and its dispersive nature. Its origin is from the phonons around the K point, corresponding to breathing modes of aromatic 6-fold rings. These modes are resonantly excited when the laser photon energy matches an electronic excitation of an aromatic cluster [38].

Other features can be observed in a typical spectrum (see e.g fig. 5.7 in the next section). In the low frequency range we observe a broad hump extending from roughly 650 cm^{-1} to 800 cm^{-1}; this broad peak has been reported also for sputtered a-C and related to a peak in the PDOS of graphite. The region between 1000 and 1800 cm^{-1} presents sometimes, in addition to the D and G peaks, weak features at about 1100 cm^{-1} and 1450 cm^{-1}. The region between 2000 and 3400 cm^{-1} presents features due to second order Raman scattering. The main contribution in this region is a broad structured feature between 2400 and 3400 cm^{-1}, with maxima at about 2700 and 2900 cm^{-1}; the origin of these features lies in the corresponding second-order peaks of the disordered graphite, but broadened due to the amorphous nature of the samples. A peak sometimes appearing at about 2150 cm^{-1} is believed to be the fingerprint of acetylenic triple carbon bonding ($C \equiv C$) [63, 64].

Different parameters can be identified to classify the various carbons according to their degree of disorder (see e.g. [38, 40, 42, 43, 45]). Most of the information on amorphous carbon comes from the 1000-1800 cm^{-1} region, and in particular from G and D peak positions, widths and intensity ratio. The two most important parameters are the G peak position and the I_D/I_G intensity ratio. The values of these parameters follow a particular trend during a so-called "amorphization trajectory" [38] from graphite to nanocrystalline graphite and then to amorphous or even tetrahedral (high sp^3 content) amorphous carbon. In the range of amorphization degree of our materials, the G peak tends to downshift and broaden with increasing disorder.

In the case of disordered graphite, Tuinstra and Koenig [40] found a relationship (TK) between the D/G intensity ratio (I_D/I_G) and the size L of the graphitic crystallites still present in the material:

$$L \cong \frac{44}{I_D / I_G} \quad [\text{Å}] \qquad (5.1)$$

This relationship was verified using x-ray diffraction. Cuesta *et al.* [60] performed a test of the TK relation for a wide range of carbons. They found that Raman spectroscopy tends to underestimate the size of the crystalline grains due to the dominant effect of small crystallites. For amorphous carbons (and this is the case of interest for the films studied in this thesis) Eq. (5.1) does not hold any longer: when the number of 6-fold graphitic rings starts to decrease, I_D decreases as well. Thus in amorphous carbon a higher I_D/I_G value indicates a higher degree of ordering.

As explained before, the Raman spectrum of carbon materials is mainly sensitive to in-plane modes (sp^2) providing information on the behaviour of the sp^2 bonded component (e.g. disordering). No direct information on the sp^3 hybridized atoms can be obtained (although some correlation has been found between Raman features and sp^3 content, and calibrations obtained to calculate the sp^3 content in carbon films grown with the same deposition technique).

In order to compare Raman spectra from different carbons, fitting of the D and G peak region is often performed. The simplest fit consists of two Lorentzian functions (often used for crystals or microcrystals, arising from finite lifetime broadening) or two Gaussian functions (expected for a random distribution of phonon lifetimes in disordered materials). It is sometimes not sufficient to fit the data with only two gaussians corresponding to the D and G peak respectively. It is necessary to use three or four gaussians to simulate the PDOS intensity rising between the D and G peaks (i.e.

the G peak asymmetry). This kind of fit, however, presents problems of stability and existence of a single solution. Many valid examples can be found in the literature of fits with a Lorentzian function for the D peak and a Breit-Wigner-Fano (BWF) function for the G peak [56-59, 61], since the asymmetry of the BWF takes into account the intensity at ≈1100 cm^{-1} and ≈1450 cm^{-1} due to the PDOS. This fitting procedure was used for the data presented in this chapter.

The analytical lineshape of the BWF is:

$$I(\nu) = \frac{I_0(1+2\frac{\nu-\nu_0}{q\Gamma})^2}{1+(2\frac{\nu-\nu_0}{\Gamma})^2} \tag{5.2}$$

where $q < -1$ is called the coupling coefficient. Γ / q is called the coupling parameter. A Lorentzian lineshape is obtained when $q^{-1} \to 0$. The Full Width at Half Maximum (FWHM) is given by

$$FWHM = \Gamma\frac{q^2+1}{q^2-1} \tag{5.3}$$

The curve maximum is slightly shifted from ν_0 and is located at

$$\nu_{max} = \nu_0 + \frac{\Gamma}{2q} \tag{5.4}$$

While $|q|$ is decreasing, the BWF lineshape changes from Lorentzian to a more and more asymmetrical one. Elman *et al.* [61] showed dependence between the coupling parameter Γ / q and the graphitization process induced by thermal annealing in graphite samples amorphized by ionic implantation (i.e. decreasing $-\Gamma / q$ with increasing annealing temperature). Further analysis of this relationship can be found in the works by McCulloch *et al.* [56, 57].

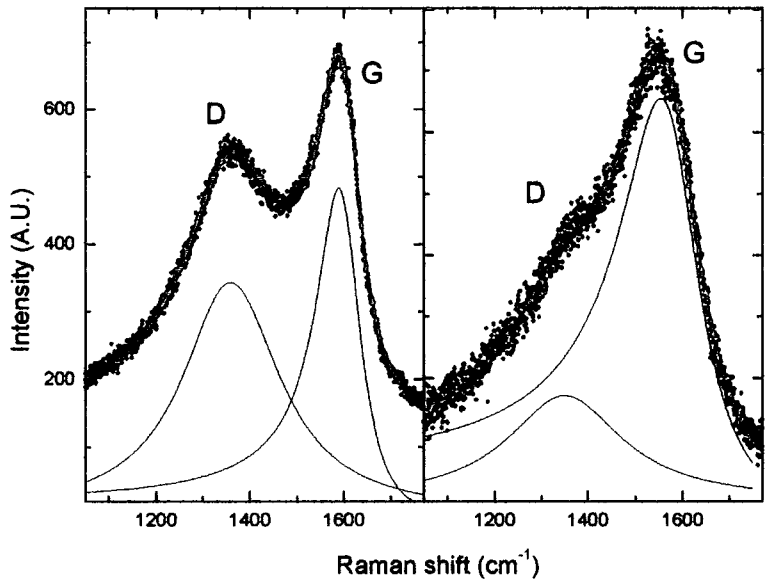

Fig. 5.6: Fitting of two different Raman spectra with lorentzian (D peak) and Breit-Wigner-Fano (G peak) wavefunctions.

In fig. 5.6 it is possible to see a Lorentzian+BWF fit of Raman spectra for two different cluster-assembled carbon film. An important difference with respect to the 2-gaussian fit is that with a gaussian fit the D peak position is always overestimated and falls above 1400 cm^{-1}; this is because the D peak fitting function must take into account the high intensity between 1400 and 1500 cm^{-1}. The kind of fit adopted, having no particular physical meaning, is not really important. When one is interested in comparing the Raman spectra of different samples (i.e. when one or more deposition parameters are varied), it is important to use the same fitting procedure for all the samples. In this way one is able to use relative indices such as I_D/I_G, D and G peak positions, peak widths, and also the BWF q value to compare the different materials.

5.3.2 Amorphous character of the cluster-assembled carbon films

In fig. 5.7 a Raman spectrum from a typical film produced with the cluster source is shown. We can recognise in the spectrum all the features typical of a very amorphous form of carbon. In the low frequency range we observe the broad hump extending from roughly 650 cm^{-1} to 800 cm^{-1} related to a peak in the PDOS (Phonon Density Of States)

of graphite. The region between 1000 and 1800 cm^{-1} shows the G and D bands typical of amorphous carbon. The region between 2400 and 3400 cm^{-1} presents features due to second order Raman scattering, with broad maxima at about 2700 and 2900 cm^{-1}. A peak appearing at about 2150 cm^{-1} in the cluster-assembled films was sometimes found. We believe it to be the fingerprint of triple carbon bonding ($C \equiv C$ stretching) [63, 64].

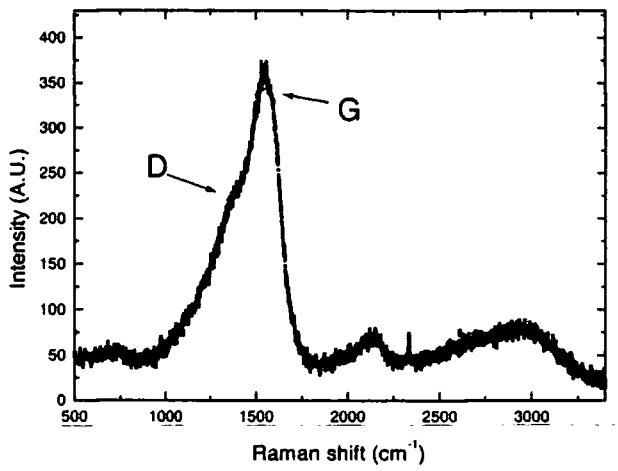

Fig.5.7: Raman spectrum of a cluster-assembled film grown with typical deposition conditions. The small peak at about 2330 cm^{-1} comes from a vibration of the N_2 molecule in the air path.

For all the samples the recorded spectra are typical of an amorphous carbon with a prevalent degree of sp^2 carbon coordination. They present the usual D and G band, whose shape, relative intensity and width are typical of sp^2 disordered carbon films (the bands are broadened and asymmetric with a high degree of overlap). It means that the Raman spectrum is closely related to the Phonon Density Of States (PDOS) of the material, according to the Shuker and Gammon formula [62]. The PDOS of this material is different from the PDOS of graphite because of the presence of a high degree of disorder (bond angle and length defects, presence of different coordination with respect to graphitic sp^2). The degree of disorder is so high that for this material the intensity ratio I_D/I_G is not in the range where the Tuinstra-Koenig relationship [40] is applicable. This means that ordered graphitic domains, if present, do not exceed 10-15 Å in size (i.e. a few 6-fold rings, probably rich in bond length and angle defects; also 5-fold and 7-fold rings are possibly present, according to theoretical studies [65, 66]).

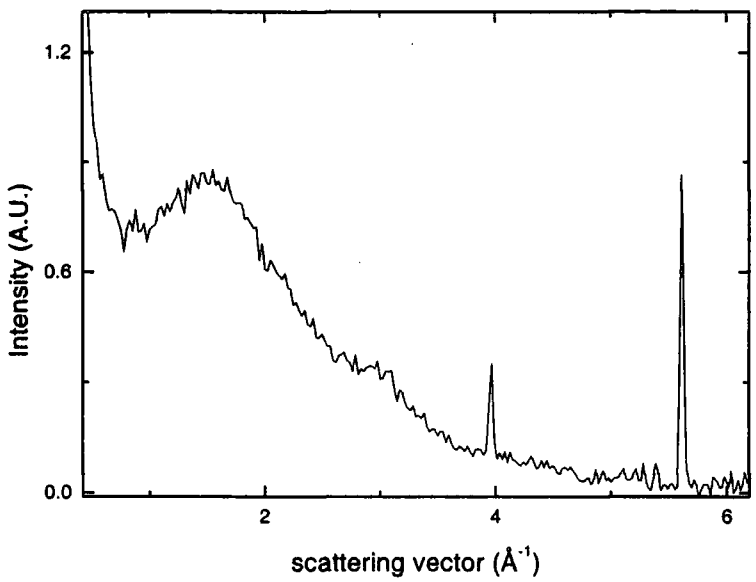

Fig. 5.8: Diffraction pattern (λ = 1.3 Å) of a cluster-assembled carbon film (after subtraction of background). No particular differences were found between films grown in different conditions. The two sharp peaks correspond to (311) and (430) reflections from the silicon substrate.

The completely amorphous nature of the films was confirmed by wide angle x-ray scattering measurements (fig. 5.8), at SRS beamline 2.3, in a grazing incidence geometry. The incidence angle was set to be close to the film critical angle (see section 5.4 below), in order to investigate the film and minimise the probing of the Si substrate. Only two very broad features with maxima at a wavevector value q = 1.55 Å^{-1} and q = 2.9 Å^{-1}, respectively, were observed (with a width of about 10 degrees at λ = 1.3 Å). These features are reminiscent of the (002) peak at q=1.8-1.9 Å^{-1} and of the so-called (10) band [67] at q=3.0-3.1 Å^{-1} in turbostratic graphite [68], and are indicative of average interatomic distances of about 4.05±0.1 Å and 2.15±0.1 Å respectively (the width coming predominantly from the distribution of atomic distances in the amorphous material rather than from confinement effects). This diffraction pattern is characteristic of sp^2 hybridized and very amorphous carbon, in particular of carbon black or amorphous carbons obtained by high temperature annealing [68-72]. The detected signal was very low and noisy, especially at high scattering angles, even at the Synchrotron Radiation Source (SRS) beamline 16.3. This did not allow an accurate calculation of the radial distribution function.

5.3.3 Characterisation of carbon materials produced in the arc discharge

A schematic view of the source has already been presented in fig. 5.2. The graphite rods face each other in a cavity whose volume is about 2 cm^3, and the nozzle of the pulsed valve for the helium injection faces the surface of the cathode. The pulse duration is typically a few hundred microseconds, and just before the valve closes, a voltage is applied between the electrodes. A plasma is produced, which is confined in the region between the valve nozzle and the cathode. The ablation occurs from a small region where the helium plasma strikes the cathode surface removing atoms via sputtering. The cathode is constantly rotated along its axis and this allows constant ablation rates (and thus constant beam intensities) over long periods. A feedback mechanism controls the valve opening time in order to maintain the optimum pressure conditions for the ablation process. The process is different from what happens in typical fullerene DC discharges [73-76]: the cathode, and not the anode, is eroded and the ablated material does not preferentially accumulate on the other electrode (in this case the anode), but rather resides in the cavity and is then expanded into vacuum.

Raman spectroscopy has been performed on the inner core of the carbon material deposited on different anodes during the operation of the deposition apparatus. Al, Cu, C, Ag, Ni anodes were employed to investigate possible differences in the ablation process. Raman spectroscopy was also performed on the external surface of these deposits, and on the eroded region of the corresponding cathode.

A reference graphite spectrum (fig. 5.9) was taken on the undamaged lateral surface of a graphite cathode. This shows as main features the D peak at 1354 cm^{-1}, the G peak at 1585 cm^{-1} and a quite sharp (FWHM about 70 cm^{-1}) second order peak at 2715 cm^{-1}. The G peak is more intense than the D peak (I_D/I_G = 0.45), giving the graphitic domains a linear dimension L of 100 Å according to the Tuinstra-Koenig formula. The D and G peaks have respectively a FWHM of 53 cm^{-1} and 24 cm^{-1}.

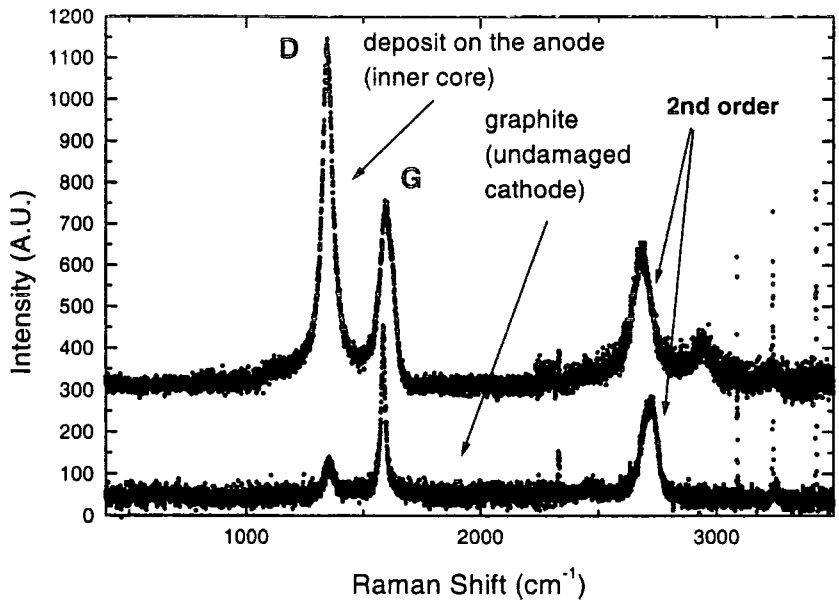

Fig. 5.9: Raman spectra of the graphite composing the cathode and of the materials produced during ablation and deposited on the anode.

The inner core of the material deposited on the anode shows, on microscopic investigation, a columnar structure, with filaments in it. Its Raman spectrum (fig. 5.9) is typical of a graphitic material, with D and G peaks clearly separated. Nevertheless, some differences are evident with respect to the undamaged graphite of the cathode, irrespective of the anode material used for the discharge:

- the D peak is more intense than the G peak ($I_D/I_G = 1.3$);
- the G peak is blue-shifted at 1589 cm^{-1} and shows a structured shape with a shoulder at about 1622 cm^{-1};
- the D peak and the second order peak are red-shifted, respectively at 1340 cm^{-1} and 2683 cm^{-1};
- the G peak FWHM is greater than in the reference graphite spectrum (50 cm^{-1});
- a new peak appears at 2930-2940 cm^{-1}.

The inner core has been analysed also for the deposits obtained using different anodes (Cu, C and Ni). The reason for using metallic anodes lies in the possibility of catalysing the formation of nanotubes, as reported in the literature [73]. The spectra were very similar to the ones described above.

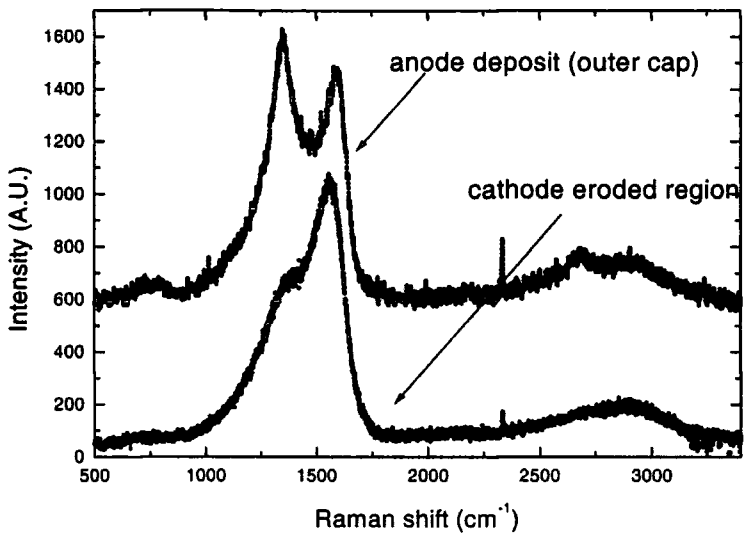

Fig. 5.10: Raman spectra of the external part of the material deposited on the anode and of the region on the cathode where sputtering occurred.

For comparison, a very similar spectrum has been measured from the cathodic (and not anodic) deposit produced by a DC discharge between two graphite electrodes in a helium atmosphere for fullerene production, where nanotubes are believed to form [73, 74].

The outer surface of the anode deposit has also been analysed for different deposits corresponding to the different anode materials. The resulting spectra (fig. 5.10) reflect the typical Raman fingerprint of a carbon material at the first stages of amorphization (probably mixed with a graphitic phase, still in the range of validity of the Tuinstra-Koenig relation), with the D and G peaks still distinct but partially overlapping (G and D peak at 1342 and 1593 cm^{-1}, second order peak, very broad, at 2700 cm^{-1}).

The eroded region on the cathode has also been analysed. Here carbon more amorphous in nature than that forming the outer surface of the anode deposit is present. Different degrees of amorphization for the eroded region were found, and they are very similar to what was found in the deposited films.

The spectra of the inner core of the deposit cannot be assigned with absolute reliability to nanotubes. They indicate a graphitic, rather ordered form of carbon. This material is less ordered than the undamaged graphite of the cathode. It has a greater I_D/I_G ratio, corresponding (if the Tuinstra-Koenig is still valid also for nanoparticle

carbon) to a size L of about 30 Å. The G peak is broader and with the 1620 cm^{-1} shoulder, and a new feature appears at 2930 cm^{-1}. However, the systematic red-shift of the D peak and of the second order peak at about 2700 cm^{-1} is typical of curved nanoparticles of carbon [73-88] (onion-like carbon, fullerenic nanoparticles and nanotubes), perhaps mixed with an amorphous carbon phase (distorted bonds between these ordered objects). These statements are supported by the TEM images of the material, showing the presence of a nanoparticle kind of carbon. Moreover, the fact that the Raman spectrum of this material is very similar to that of the deposit obtained in a DC discharge, in which nanotubes are formed, suggests the presence of a fraction of nanotubes in it.

The discharge generates an amorphous carbon phase on the cathode, while the materials deposited on the anode possess a high degree of order. Corresponding to particular discharge conditions, in which a bulk deposit is formed, this bulk material is terminated with a cap made of a different, more amorphous kind of carbon. A structural difference between the inner and the outer material is already evident from the SEM pictures of other deposits. The absence of relevant differences when using anodes of different materials supports the idea that the carbon plasma formation process is independent from the arc discharge, and due to sputtering of the cathode by the He plasma.

5.3.4 Raman scattering study of the inertial separation effect

The inertial separation effect in the cluster beam is interesting, due to the possibility of tuning the mass of the deposited clusters by simply selecting the inner or the outer region of the cluster beam in the deposition chamber with a tailored skimmer. To analyse this phenomenon a sample was grown by placing a large area substrate directly in front of the source, before the skimmer, in order to intercept the whole section of the cluster beam leaving the source nozzle. A deposition with a diameter of about 3 cm was obtained. This sample is called BEAM. Its thickness ranges from roughly 10 nm at the periphery to roughly 1000 nm in the centre, as measured by a laser interferometry technique [89].

Since clusters maintain, at least partially, their original structure [23], the films should be reminiscent of the precursor clusters and present different coordination and local order. Experimental and theoretical investigations have shown that small carbon

clusters roughly below 40 atoms have chain or ring structures whereas larger clusters have the tendency to form three-dimensional cage-like structures characterised by sp^2 coordination [90-92]. Separation effects in front of the skimmer should enrich the periphery of the beam of small chain-like clusters, leaving large fullerene-like clusters in the beam centre. Films grown using the periphery of the beam are therefore expected to show a very disordered structure; on the other hand, films grown with the central region of the beam should be characterised by a disordered graphitic structure reminiscent of the fullerene-like character of the clusters.

Raman spectra were measured in points at different radial distances from the centre of the deposition (corresponding to the cluster beam axis).

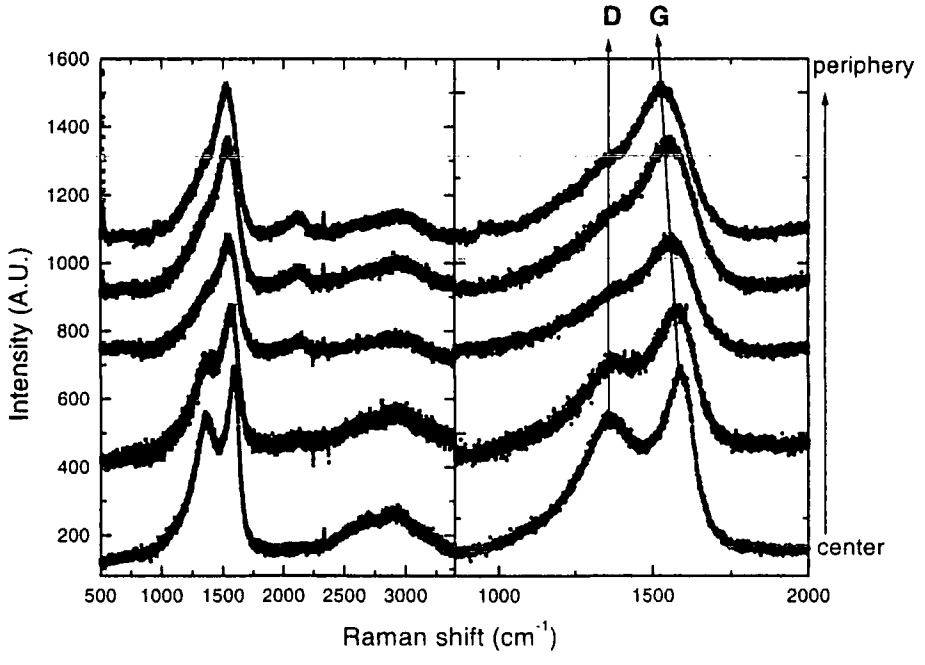

Fig. 5.11: Raman spectra from sample BEAM measured in different points, from the periphery (top) to the centre (bottom). The red arrow indicates the softening of the G peak; the blue arrow the position of the D band.

These spectra are shown in fig. 5.11, with intensities shifted for clarity. The shape and the shift of the G band are typical of amorphous sp^2 carbon. The D peak is present as a broad shoulder on the left of the G band. The peak at 2150 cm^{-1} is quite unusual for disordered carbon produced by depositing carbon atoms or ions (though a similar peak is found in amorphous CN films and assigned to the C≡N stretching vibration [93]). As already stated, it can be attributed to the presence of carbon chains characterised by *sp* acetylenic bonding [63, 64]. The evolution from the inner to the outer region of the

deposition is evident: the spectra corresponding to the outer region are clearly indicative of a more amorphous and disordered sample, with an intense 2150 cm^{-1} peak developing. In fact smaller clusters are believed to have chain-like configurations, with C≡C bonds. These spectra are compatible with higher sp^3 content, even if Raman spectroscopy cannot prove it. The spectra of the region close to the deposition centre are indicative of a more graphitic carbon; this could be due to the fact that bigger clusters have an average hybridization similar to graphitic sp^2.

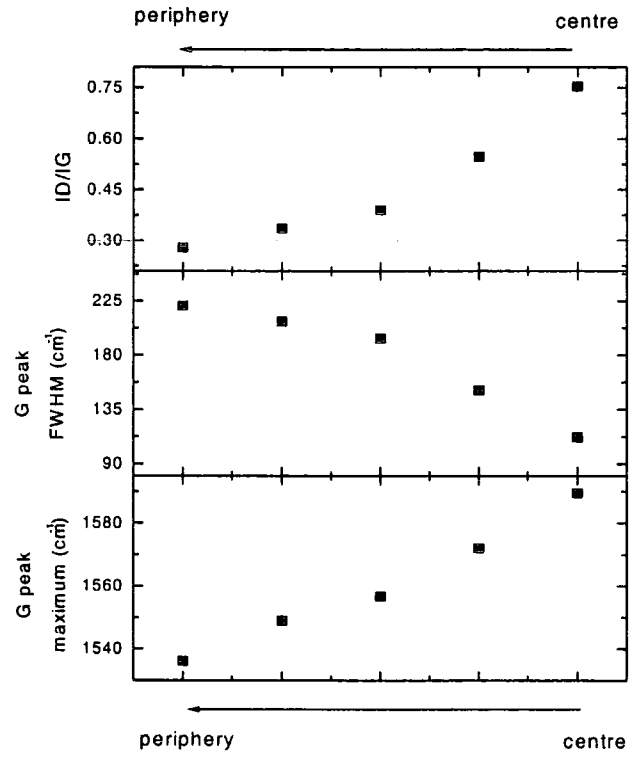

Fig. 5.12: Evolution of Raman parameters from the centre of the deposition towards the periphery in sample BEAM.

Very good fits of the data were obtained using a BWF + Lorentzian fit in the region 1000-1800 cm^{-1}. A clear evolution of the most indicative fitting parameters, such as G peak position and FWHM, I_D/I_G, BWF coupling parameter, was obtained, indicating a transition to a more amorphous and disordered carbon (see fig. 5.12).

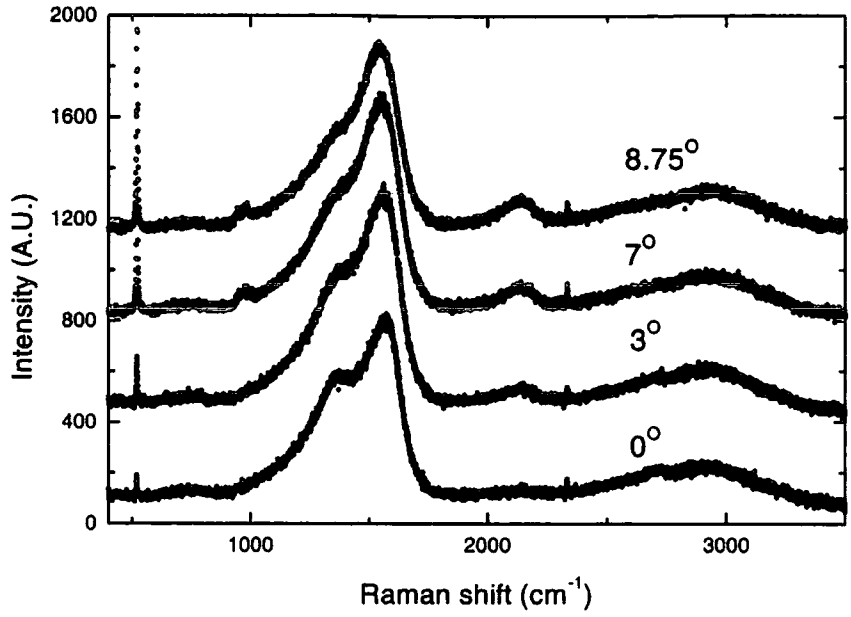

Fig. 5.13: Raman spectra of films deposited using different tilts of the source axis with respect to the skimmer axis. The peak at 521 cm^{-1} is the first order Raman scattering from the Si substrate.

We have exploited separation effects to deposit thin films with different cluster mass distributions also by using the tilt mechanism for the source described in section 5.2. This permits the deposition of films with different characteristics, but which are uniform over an area of 1-2 cm^2. The top spectrum in fig. 5.13 corresponds to a source tilt of 8.75°, i.e. selection of a region rich in small clusters (periphery of the beam). Going from the top to the bottom spectrum in fig. 5.13, one can follow the evolution from an amorphous carbon towards a disordered graphitic structure by shifting from the periphery of the beam towards the central region large clusters (smaller tilts). This evolution is confirmed by a hardening of the G peak, the appearance of a well-defined D band and by the narrowing of the two lines. All these parameters are in agreement with a graphitization of the sample. Raman spectra of films with increasing thickness, but deposited using the same source tilt (i.e. same cluster size distribution), were practically identical. This confirms that thickness does not affect the local bonding topology of carbon atoms (on the other hand, thickness-related structural effects are evident at a mesoscopic scale, as shown in the next section). The effect of cluster size on Raman spectra was also confirmed by studying films in which the size distribution was varied by adjusting the source operational parameters (e.g. pressure).

Separation effects in the beam offer the possibility of producing films characterised by different nanostructures and coordination. This technique does not require the use of mechanical filters and it works with neutral particles. It is well known that gas-phase synthesis of carbon clusters can efficiently produce acetylenic species [94]; our experiments suggest that they can be deposited and that they can survive. Further investigations in order to identify the 2150 cm^{-1} peak have involved the study of the peak evolution as a function of temperature. This was done in vacuum, using the Oxford Instruments thermocryostat described in section 3.1.1. We observed a progressive graphitization of the film material, and the acetylenic peak disappeared at about 600 K, in agreement with previous studies on the thermal stability of the C≡C triple bond [95].

5.3.5 Deposition of films by focused beams

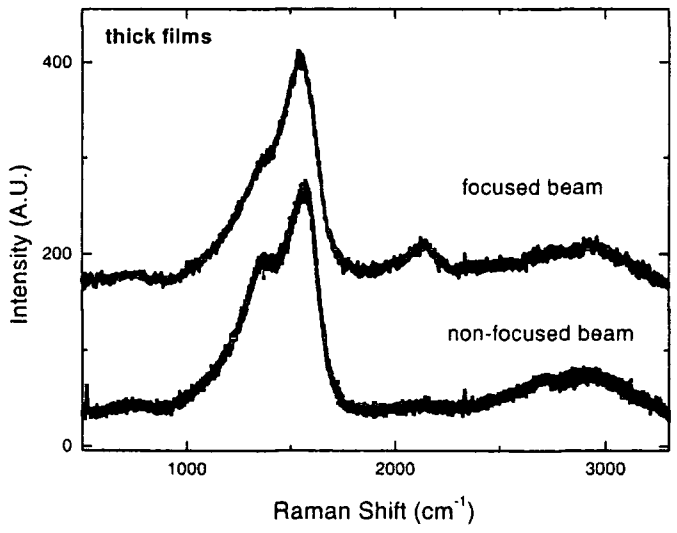

Fig. 5.14: Raman spectra of thick films deposited using a focused beam and a non-focused beam, respectively. They correspond to the thick films studied with Brillouin spectroscopy in section 5.5.

The use of the low-divergence, high-intensity focused beams (as explained in section 5.2) permits the deposition of compact and smooth films, from clusters with smaller sizes than those obtained, on an average, with unfocused beams. Raman spectroscopy (fig. 5.14) has shown that the bonding in these films reflects the nature of the precursor clusters, similar to what is observed in the very amorphous films deposited with high source tilts (i.e. from the periphery of beam). On the other hand,

films deposited in the same deposition chamber with a standard source configuration, without beam focusing or source tilting, are less amorphous in nature (fig. 5.14). Moreover, Raman spectroscopy confirmed that films deposited by focused beams are uniform, in terms of local bonding, over the whole deposition area.

5.3.6 Possible presence of large graphitic particles in the centre of the beam

Raman spectroscopy has proved very useful also for the detection of problems in the source functioning and in the deposition process. Since the cluster beam composition is strongly affected by the pressure conditions in the source, and thus by the valve pressure and opening time, valve opening-arc discharge delay, etc., optimum conditions have been analysed and identified. For example, under particular circumstances (non-optimum pressure conditions), uniform films but with a darker region at the centre were deposited. Raman spectra corresponding to the central and external region are shown in fig. 5.15.

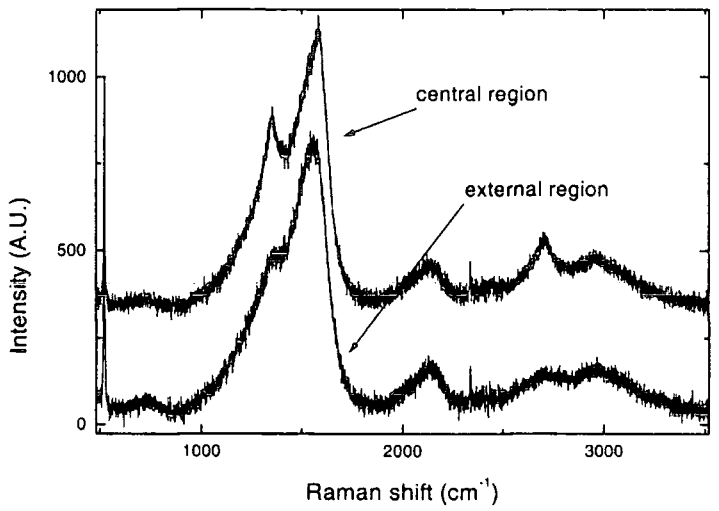

Fig. 5.15: Raman spectra of a film deposited in non-optimum deposition (pressure) conditions: center of deposition (top) and external region (bottom).

The spectra look similar, and the G peak position, the second order features and the peak at 2150 cm^{-1} are typical of a very amorphous carbon, like that produced in the periphery of the beam under normal operation conditions. Nevertheless, the central

region shows anomalous sharp features superimposed on the D and G bands and on the second order at about 2700 cm^{-1}. The first guess was that this was a composite material, with an amorphous component and a graphitic component.

Indeed, by subtracting the two spectra, a spectrum corresponding to nanocrystalline graphite was found (fig. 5.16). The Tuinstra-Koenig relationship gives a value of about 50 Å for the size of the graphitic domains. A subsequent analysis of the cluster beam composition revealed the presence of huge graphitic particles, formed under these particular source conditions. Of course the advantage of using Raman spectroscopy is that it is a fast and non-destructive method and it does not require accurate time-of-flight characterisation of the beam population.

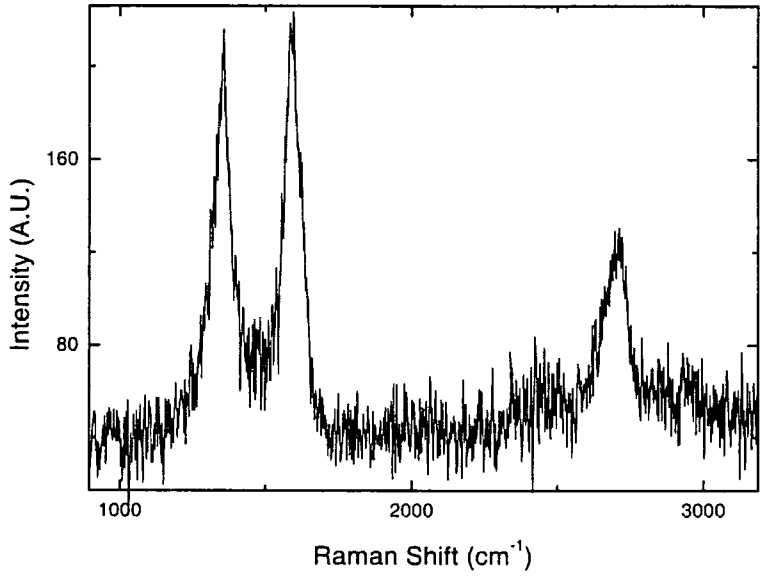

Fig. 5.16: Raman spectrum resulting from the subtraction of the two spectra of fig. 5.15: a typical nanocrystalline graphite fingerprint is obtained.

5.4 Density measurements by x-ray reflectivity

X-ray reflectivity measurements have been carried out on carbon cluster-assembled films [96] (see also Chapter 4). Nevertheless, the huge surface roughness (also confirmed by SEM pictures) results in a very high diffuse scatter, so that the specularly reflected intensity falls very rapidly with angle. No interference fringes were seen, from which the thickness of the films could be inferred (fig. 5.17a), in any of the films. Moreover, the carbon films possess a high fraction of voids and have a porous

structure, so that their density is lower than that of the Si substrate. This means that only the Si critical angle, or a double critical angle in some samples, could be seen (fig. 5.17b). Specular reflectivity curves were measured, with the incidence angle θ_i varying in the range 0-2000 arcseconds, with a step of 10 arcseconds.

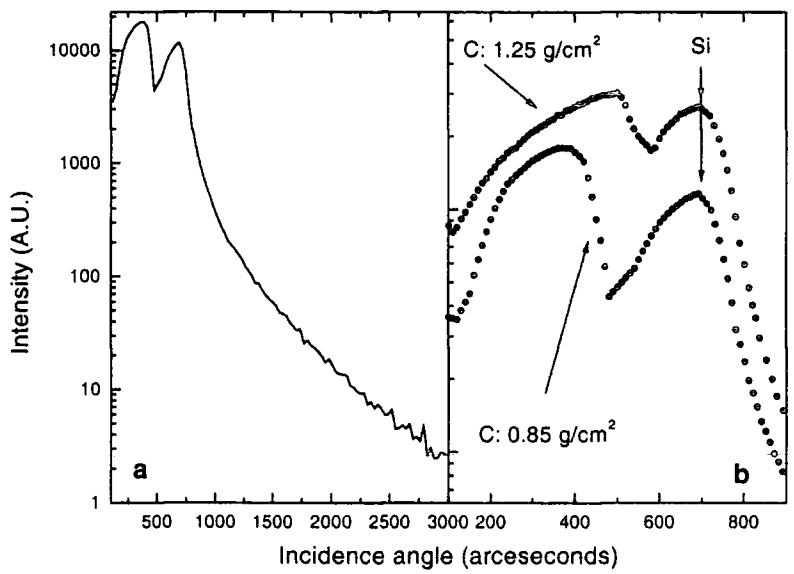

Fig. 5.17: a) typical complete reflectivity curve from a cluster-assembled carbon (no interference fringes, fast intensity fall); b) double critical angle (from C and from Si) in two samples with different densities.

The only information obtainable from these measurements is thus the density of the films, from the first critical angle, where a double critical angle is detected. The density in the case of films grown by non-focused beams has a value of 0.8-1.0 g/cm^3, in accordance with other measurements (e.g. optical ellipsometry). In films deposited in the first chamber (such as film BEAM) the density ranges from 0.8-0.9 g/cm^3 to 1.2 g/cm^3, moving from the centre towards the periphery of the deposition. In the case of films grown using a focused beam (and thus smaller clusters) the more compact nature of the films is confirmed by the higher density value of $\rho = 1.25 \pm 0.05$ g/cm^3.

5.5 Brillouin scattering from cluster-assembled carbon films

As discussed in chapter 2, inelastic light scattering can be used to study the vibrational properties of materials and in particular Brillouin scattering (BS) can detect thermally excited acoustic waves (long wavelength bulk or surface acoustic phonons) propagating in the medium.

In this section it is shown how BS can be used to study, at a typical length scale of hundreds of nanometers, the mesoscopic vibrational properties of the cluster-assembled nanostructured carbon films produced by the cluster source.

Brillouin scattering spectra were recorded at room temperature and in the backscattering geometry, using the Sandercock interferometer with the λ_L=514.5 nm Ar^+ laser excitation. The samples were kept in vacuum using the Oxford Instruments thermocryostat to prevent damage by photo-oxidation effects. These effects have already been observed in Brillouin measurements of fullerite crystals [97, 98] and have been seen also in the cluster-assembled carbon films, resulting in the formation of holes in the samples. The spectra were recorded with a free spectral range of 30 GHz using a laser power of 35 mW onto the sample. Due to the low signal intensity, long (about 180 minutes) acquisition times were required.

5.5.1 Films grown by a non-focused beam

The first measurement was carried out on a thick (thickness > 1 μm) film grown in standard deposition conditions, without tilting the source or focusing the beam (thus depositing the clusters from the central region of the beam, see its Raman spectrum in fig. 5.14). Only damped bulk acoustic phonons could be detected (see fig. 5.18). The typical wavelength of these phonons was λ_{ph} = 170 nm (see section 2.3.1, Eq. (2.19)). This indicates that for a length $d > \lambda_{ph}$ the films can be modelled as a continuum with translation invariance and effective elastic constants, although structural disorder at smaller scales scatters the phonons significantly. The presence of a rather strong central peak in the spectra can be ascribed to non-propagating (overdamped) or confined vibrational excitations within the films, probably connected with different correlation lengths smaller than d. The damped bulk acoustic phonons could be coupled to the

confined modes by a relaxation mechanism. The films exhibit a high degree of surface roughness and multiscale granularity; this leads to considerable broadening of the phonon peaks and to the presence of an intense elastic background. This impeded the measurement of surface phonons, which were detected only in thinner films.

In fig. 5.18 a weak and broad peak is just visible at about 17 GHz together with a strong central peak about 10 GHz wide. Varying the incidence angle θ_i did not shift the peak position in frequency, which is a behaviour typical of bulk phonon peaks. Assuming that the film is elastically isotropic the transverse peak should not be visible in backscattering. So the observed peak at frequency ν_L can be assigned to scattering from the longitudinal (L) bulk phonon with wavevector $q=(4\pi/\lambda)n$ and phase velocity $v_L=\lambda\nu_L/2n$. The longitudinal sound velocity v_L is connected to the adiabatic bulk modulus B and shear modulus μ by the formula

$$v_L = \sqrt{\frac{C_{11}}{\rho}} = \sqrt{\frac{B+\frac{4}{3}\mu}{\rho}} \qquad (5.5)$$

where ρ is the mass density, C_{11} is one of the elastic constants, B and μ are the bulk and shear modulus respectively. A direct ellipsometric measurement at 514.5 nm of the index of refraction n of a film deposited in the same conditions gave $n \cong 1.5$ [23]. We thus obtain $v_L \cong 2900$ m/s. We can assume $\rho \cong 0.80\text{-}0.85$ g/cm^3, from the x-ray reflectivity measurements, and so C_{11} is about 6.5 Gpa (see Table 5.1 below). B and μ cannot be evaluated from the shift of only one bulk peak and analysis of the surface modes in thinner films must be undertaken.

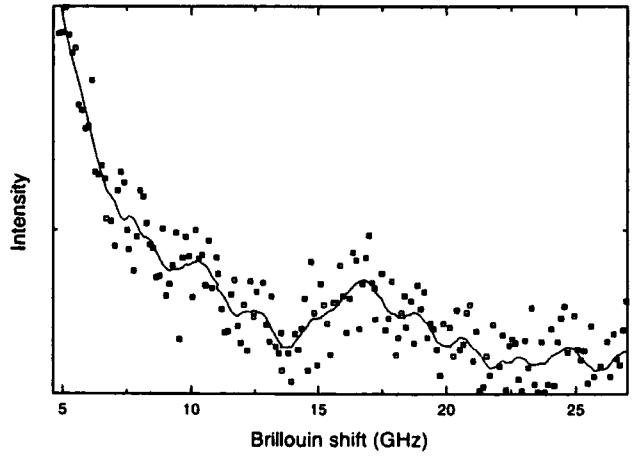

Fig. 5.18: Brillouin spectrum of a thick film grown with standard deposition conditions (without focusing of the beam). Points are experimental data, line represents data after smoothing.

The second series of measurements was carried out on sample BEAM in the same points where the Raman spectra were acquired. It is useful to remember that in this sample a variation in the thickness across the approximately gaussian profile (measured with the laser interferometry technique) corresponds to a variation of the precursor cluster size and also, probably, of the material nanostructure.

On the outer border of the deposition, far from the deposition centre, the film thickness is very small (about 10 nm); the film becomes thicker moving towards the centre (up to 1 μm). We expect the Brillouin spectrum of the thinner region to be a modification of the Si substrate surface spectrum, due to the presence of a very thin carbon film. This spectrum should vary as a function of thickness, and should become similar to the spectrum of the bulk sample, with a big central peak, close to the centre of the deposition where the film is thicker (and more graphitic). This is precisely what was observed (see fig. 5.19). The Rayleigh surface peak detected at 14.7 GHz for a pure Si substrate undergoes a redshift (about 300 MHz) for very thin carbon coverage; the peak then broadens as the layer thickness increases, until the central peak intensity does not allow the detection of surface modes. Indeed, a surface can not even be defined when the roughness is of the order of 100 nm or more.

Theoretical modelling of the dynamical behaviour of such a system is being developed in Milano. There is great interest in the central peak, characteristic of this system, which could give information on a fractal dynamical structure of the films (the so-called fractons discussed below in section 5.6). The interest is in the study of the dynamical properties of a system that cannot be thought of as a continuous film, having a "ball-assembled" structure with voids in it.

The problem while studying this film is the inherent coupling between two deposition parameters that vary together, the thickness and the precursor cluster size distribution. Since many studies (see for example [99]) show that in thin films the degree of surface roughness increases with increasing thickness, we may expect that the rise of the central peak, which we attribute to a rising disorder in the mesostructure of the film, is due to the increasing thickness while moving towards the centre of the film, and not to the variation of the size of the precursor clusters, which is believed to have an influence on the local nanometer order but not on the mesoscopic structure. Indeed, AFM measurements have shown that the huge roughness of cluster-assembled carbon films is a function of their thickness, and not of the size of the precursor clusters.

Roughness, of the order of tens or hundreds of nm, was found to increase linearly with thickness and saturation was not reached even for films thicker than 1 μm.

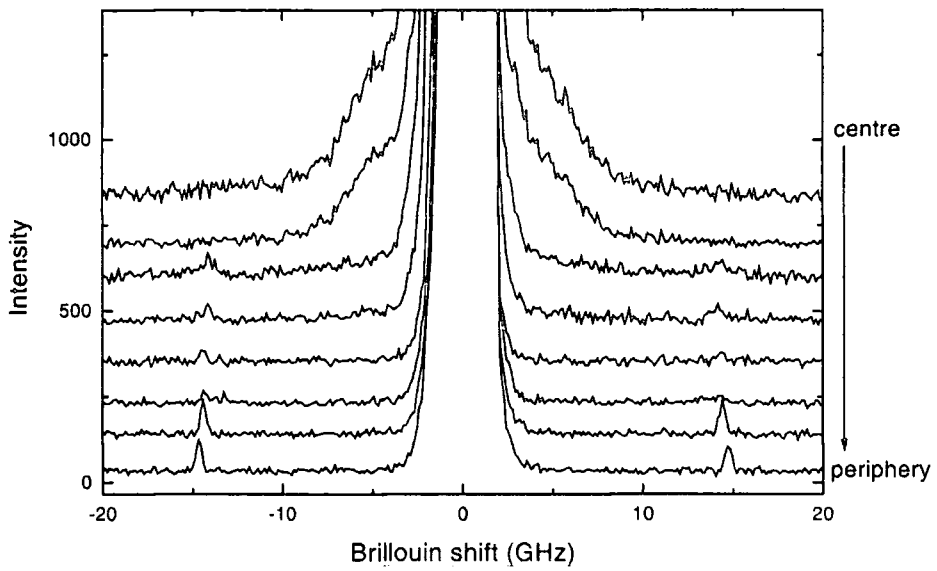

Fig. 5.19: Brillouin spectra from different points of sample BEAM, from the periphery (bottom) to the centre (top).

In order to test the effect of the thickness-related roughness, and separate thickness and cluster size distribution effects, on Brillouin scattering measurements, three series of films were grown. Each series consists of films grown with the same source conditions, but having different thickness. The source parameters were varied from one series to the other in order to achieve a different selection of the precursor cluster size distribution, but a substantial homogeneity over the area of the film. The difference in the local order (as well as the homogeneity within a single film or a single series) was demonstrated by Raman spectroscopy, as shown in section 5.3.4. It is thus possible to decouple the effect of varying the thickness from the effect of varying the precursor cluster size. The series were called "series 1", "series 2" and "series 3", going from the most amorphous (small clusters) to the most graphitic one (large clusters).

While thick films (thickness > 500 nm) and the film BEAM were grown on Si substrates, for the Brillouin measurement of these films and of thin films in general it turned out that a different substrate was preferable. Measurements from thin films grown on Si presented a very low signal-to-noise ratio. This can be ascribed to the non-negligible width (50-60 GHz) of the central peak that can be seen in the measurement

of a pure Si substrate, whose origin is a second order Raman difference mode. We thus decided to deposit the thin films on polycrystalline Al foils whose thickness was about 10 μm. Provided that the surface is smooth enough, this substrate allows a better signal-to-noise ratio, principally for the following reasons:

- absence of a wide central peak;
- high surface reflectivity of the substrate, and so bigger interaction of light with the film. Al is a metal, and the imaginary part of its refractive index is so high (2.03) that there is virtually no penetration in the substrate. This also accounts for the fact that the ripple effect is predominant over the elasto-optic contribution from the volume of the substrate, and this makes the Brillouin measurement more sensitive to the film properties. Also Raman measurements from films deposited on Al showed a signal intensity up to five times higher than in films deposited on Si.

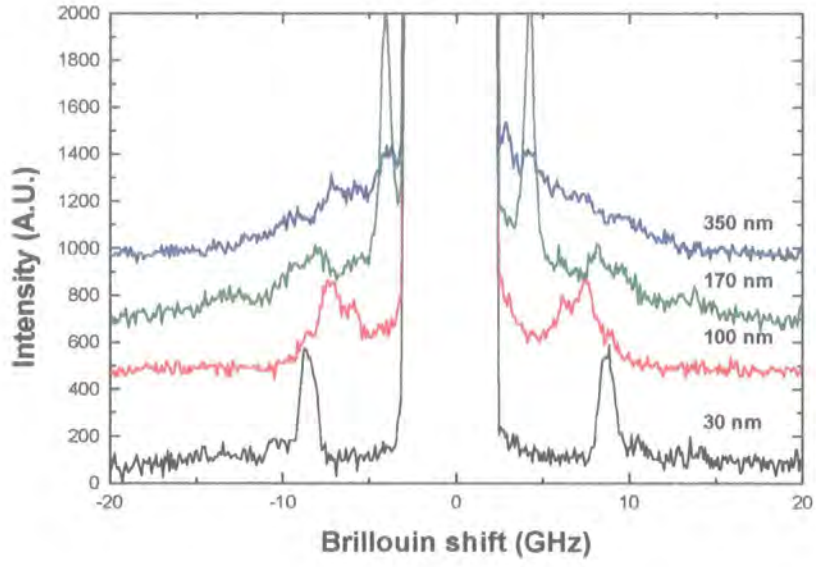

Fig. 5.20: Brillouin spectra from films of "series 2", deposited using unfocused beams, with the same cluster size distribution but different thickness. In these measurements the incidence angle is 50^{O}. The effect of varying the thickness is reflected in the nature of the modes travelling in the film and in their velocity.

In fig. 5.20 Brillouin scattering measurements for the films of "series 2" are shown. No particular difference has been found in the evolution of the central peak between the three series. This confirms that, as predicted, the localisation effects represented by the central peak are not affected by the local order (and thus by the cluster size), but only by the surface mesostructure, which is in this case a function of

thickness. We observed that increasing the film thickness, from a few tens to some hundreds of nanometres, a strong localisation is reached, in which the acoustic phonons do not propagate along the film surface (and a surface is probably not even well defined).

The effect of varying the size distribution of the deposited clusters has instead an effect on local bonding and on the elastic properties of the films, which is reflected in the position and dispersion relation of the surface acoustic peaks at a fixed thickness. Apart from the considerations on the origin of the central peak, the surface features observed in thin films can in fact be used to calculate the material elastic constants. This has been the object of extensive study and of a degree thesis project [100] in the Materials Laboratory at Politecnico di Milano.

One thin film for each series (thickness about 100 nm) has been measured varying the laser incidence angle between 10^0 and 70^0 in order to obtain the dispersion relation for the observed surface phonons (i.e. their frequency shift as a function of the incidence angle). The very thin films have been chosen to avoid, in the analysis of the data, complications arising from the central peak. The observed peaks have been assigned to a Rayleigh mode and to a Sezawa mode, and from the dispersion relation the elastic constants of the films have been estimated, using the software described in section 3.2.2 (fig. 5.21). The situation is that of a "slow film on a fast substrate", i.e. $v_t^{(f)} < v_t^{(s)}$ (see section 2.3.5).

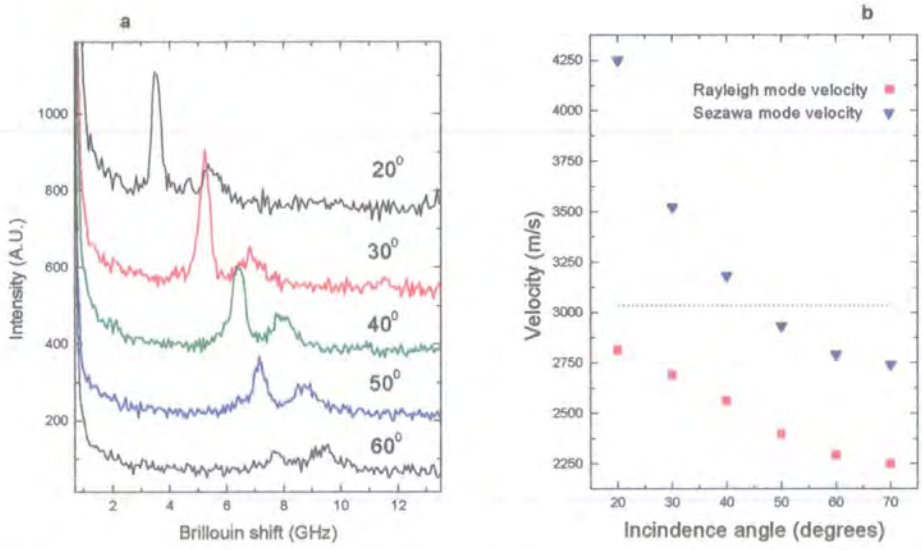

Fig. 5.21: a) Brillouin spectra from film "thin 3" as a function of the incidence angle; b) dispersion relation for the velocity of the Rayleigh and Sezawa peak in the same sample; the dashed line represents the transverse threshold of the Al substrate (courtesy C. Casari, Politecnico di Milano).

Differences in the calculated elastic constants were evidenced between the three samples. It was found that the Young modulus E increases (Table 5.1) from about 3 GPa to about 7 Gpa moving from a very amorphous film to a more graphitic one, while G (shear modulus) increases from about 1 GPa to about 2.5 GPa. Also C_{11} increases, and this could explain why in thick films a higher value of C_{11} was found for the non-focused film, where the local bonding is less amorphous than in focused films (see below). The films are called, in Table 5.1, "thin 1", "thin 2" and "thin 3" going from the most amorphous to the most graphite-like. In polycrystalline graphite $G \cong$ 2-5 Gpa [101]: this means that our films have a shear modulus comparable to that of graphite, confirming the sp^2 nature of most covalent carbon bonds. The porous disordered structure is instead responsible for the very soft value of the Young's modulus. This indicates a low-density, isotropic material with shear properties similar to those of graphite but with a different compressibility.

Table 5.1: Values of the elastic constants E and G for 3 thin film ("thin 1" is the most amorphous, "thin 3" the most graphitic) deposited with a non-focused beam, for the thick film deposited with a non-focused beam and for the thick film deposited using a focused beam (see Section 5.5.2).

SAMPLE	Nominal thickness (nm)	E (Gpa)	$G = C_{44} = \mu$ (Gpa)
thick non-focused	> 1000	6.5	--
Thin 1	100	2.7	1.1
Thin 2	80	3.4	1.6
Thin 3	100	7.2	2.6
thick focused	1100	5.3	2.4

5.5.2 Films grown by a focused beam

Films with a completely different nanostructure, more compact and smoother, can be grown using the focusing device described in section 5.2.

A thick film of thickness about 1.1 μm (measured by AFM) was deposited with a focused beam (small divergence) to achieve a high fraction of small cluster sizes with great selectivity with respect to the large clusters (see Raman spectrum in fig. 5.14). The films obtained in this way are more close-packed and smoother with respect to those deposited without beam focusing, and this reflects in Brillouin spectra where peaks and features are well defined and the broad central peak is absent.

These spectra are interesting mainly for the absence of the central peak and the high intensity and small width of the Rayleigh peak (see fig. 5.22), never observed before from nanostructured carbon films. This feature supports the conclusion that long life acoustic phonons can propagate along the film surface. In other words, at a mesoscopic scale of observation, this film appears as a homogeneous elastic continuum, and the relatively low surface roughness, acting as surface structural disorder, only introduces a small acoustic damping factor without hindering the phonon propagation. This fact is consistent with a smooth surface film of compact material made of close-packed small clusters and it is important in comparison with the results of the experiments on the PMCS films deposited without beam focusing in which the surface roughness increases with the film thickness (see also [16]). As shown above, for this kind of films the surface Brillouin spectrum for a thickness comparable to that of the focused beam film (> 1 μm) showed a central peak, and either no surface peaks or only a very weak bulk peak, because of the huge surface roughness (not allowing the propagation of surface modes). The only way to obtain information from surface Brillouin experiments on non-focused beam deposited PMCS films has been to measure thin films deposited on aluminium substrates in order to achieve a higher signal-to-noise ratio. Nevertheless RW peaks in these spectra showed lower intensities and higher widths than in the thick focused film, pointing to a non-negligible damping factor in the acoustic phonon mean lifetime caused by the surface disorder.

The detection of acoustic modes in a thick film gives an advantage, with respect to a thin film, in that we can consider the film as a semi-infinite medium and so the nature and the characteristics of the acoustic waves propagating in the system are not affected by the thickness and thus by the presence of the substrate. In our experiments the limit is about 500 nm.

Thus Brillouin scattering experiments were carried out to determine the velocity v of either surface acoustic waves (SAW) or bulk waves (BW) and possibly determine the elastic properties of the film without the need for a complete dispersion relation in thin films. When the thickness is higher than 500 nm the film can be regarded as a semi-infinite medium, a BW can travel inside the material, while the SAW velocity is non-dispersive and its propagation is not affected by the presence of the substrate.

Spectra recorded at different angles of incidence (θ_i =50° and 70°) are shown in fig. 5.22. They are characterised by three peaks: the peak just before 5 GHz and the one around 8 GHz correspond to surface and pseudo-surface waves respectively and are

characterised by a frequency shift depending on the angle of incidence θ_i. The former is a Rayleigh wave (RW). The latter is a longitudinal resonance (LR) or high-frequency pseudo-surface wave. This is a surface mode of a mixed character; its longitudinal polarization component is bounded near the surface while its shear polarization component is unbounded and radiates elastodynamic energy into the bulk. The broad peak at about 11 GHz is a true bulk mode and it has been assigned to the longitudinal bulk wave (LB) due to the isotropic assumption that does not allow the transverse bulk wave to be visible in backscattering geometry. Our interpretation of the observed peaks is also strongly supported by numerical simulation of the total scattering cross section (see below).

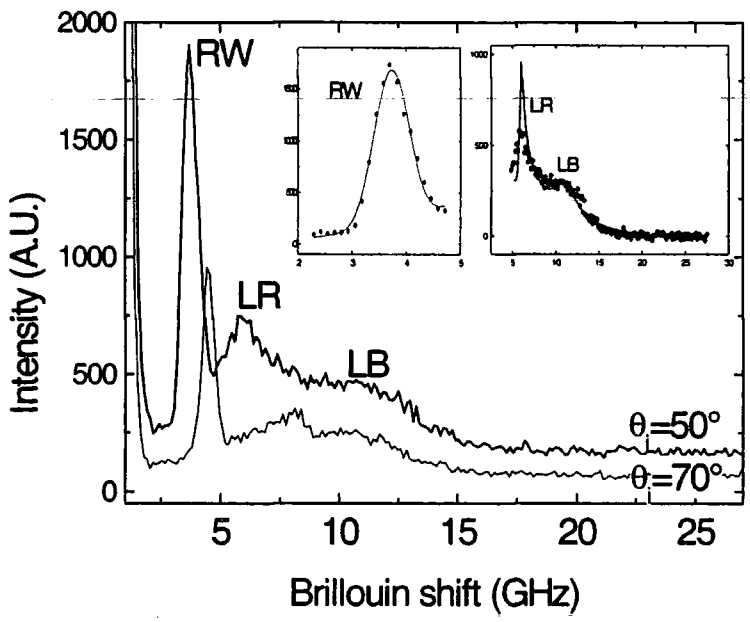

Fig. 5.22: Brillouin spectra from a focused film, at two different angles of incidence, θ_i=50° and θ_i=70°. The surface spectrum is characterised by the dependence on the angle of incidence of the peak frequency (Rayleigh wave, RW, and longitudinal resonance, LR) while the bulk spectrum presents a longitudinal bulk, LB, wave with a fixed frequency position. In the small inset boxes fitting of the θ=50° spectrum is shown (courtesy C. Casari, Politecnico di Milano). The numerical simulation of the scattering total cross section (line) is superimposed to the experimental points in the right box while in the left one the RW peak was fitted separately with a fitting procedure using a pseudo-Voigt function.

As explained in chapter 2, SAWs are visible as peaks at characteristic frequencies depending on the incidence angle θ_i according to Eq. (2.38):

$$v = \frac{\lambda_L \nu}{2\sin\theta} \tag{5.6}$$

while BW are usually observed at higher frequencies given by Eq. (2.21):

$$v = \frac{\lambda_L \nu}{2n} \tag{5.7}$$

where n is the refractive index of the medium.

Fitting peaks to the experimental data (as shown in fig. 5.22), we found v_R=1240±50 m/s for RW velocity and v_L=2070±50 m/s for the LB and LR velocity. For a semi-infinite medium the velocity of the surface Rayleigh wave v_R depends only on the longitudinal and transverse bulk wave velocities v_L and v_T. Solving numerically the corresponding equation (see [102]) we found v_T=1390 m/s. The velocities v_L and v_T and the corresponding frequencies ν_L and ν_T represent the thresholds between the discrete and the continuum regions of the spectrum (see section 2.3.5). In particular for a bulk material the RW is always at a frequency lower than ν_T ($\nu_T < \nu_L$), the LR mode is exactly at ν_L and the LB wave is at a frequency higher than ν_L.

The propagation velocities of the observed modes can be used to determine the elastic properties of the material. The longitudinal bulk wave velocity v_L is directly connected to the C_{11} elastic constant by the formula $v_L = \sqrt{C_{11}/\rho}$ where ρ is the mass density. Using the value ρ = 1.25±0.05 g/cm^3 obtained by X-ray reflectivity, we obtain C_{11}=5.4±0.2 GPa. A value of 2.4±0.1 GPa was found for the shear modulus (μ=G=C_{44}), determined using the relation $v_T = \sqrt{C_{44}/\rho}$. Knowing C_{11} and C_{44} allows one to characterise completely the elastic properties of an isotropic material and other elastic constants such as the bulk modulus B, Poisson ratio ν and Young's modulus E can be determined. We found E=5.3 GPa, B=2.2 GPa and ν=0.1 (see Table 5.1). These values are comparable to those obtained for the thin films (thickness of about 100 nm or less) deposited with the unfocused beam, in particular they are close to the values of the harder film of the thin film series (Table 5.1). The comparison with diamond elastic constants E=1141 GPa, B=442 GPa and ν=0.07 again indicates a very soft and highly deformable material.

The presence of both the longitudinal bulk wave and the surface resonance reveals a non-negligible elasto-optic effect as a scattering channel in addition to the ripple effect mainly responsible for the RW peak. This occurrence permits us to determine, without any other information, the real part of the refractive index as the

ratio between the frequency position of the LR and LB modes: $v_L/v_{LR} = n/\sin\theta$, and so n is evaluated to be about 1.4 (in agreement with ellipsometry measurements [23]).

The total scattering cross section was studied by Carlo Casari in the Materials Laboratory at Politecnico di Milano [100], by numerical simulations based on a Green's function approach, using the software described in section 3.2.2 [103]. The calculus requires the knowledge of the values of ρ, n, C_{ij} and the elasto-optic coefficients k_{ij}. The peak positions depend only on the physical quantities (ρ, Re(n) and C_{ij}) determined experimentally, while Im(n) and k_{ij} are responsible only for the relative peak intensities. The simulation can reproduce the experimental frequencies of the peaks. It does not succeed in calculating the intensity ratio between the discrete and the continuum spectrum for this kind of film. The reason of this is related to some physical phenomena that the homogeneous continuous elastic model does not include in its calculation, the most relevant in this case being the acoustic damping caused by the local disorder. For this reason we reported separately in the insets of fig. 5.22 the fit of the RW peak with a pseudo-Voigt function and the result of the numerical simulation for the continuum spectrum superimposed on the experimental points. A reasonable agreement for the peak intensities was achieved using k_{11}=8, k_{12}=2 and k_{44}=3. These values are only a rough evaluation of the order of magnitude of the elasto-optic constants, but so far they have never been measured in this kind of material. In particular the intensity ratio I_{LR}/I_{LB} of the LR and the LB peak is strongly related to the k_{11}/k_{44} ratio while the absolute values of k_{ij} have a weaker correlation with the intensity of the whole continuous part of the spectrum.

The imaginary part of the refractive index is responsible for the opacity broadening of the bulk peak and we used a value of 0.2 in an attempt to reproduce the experimental width of the LB peak. This value is in perfect accordance with the results of ellipsometry measurements [23].

Finally the layer projected phonon density of state (LPPDS) [104] calculated for the parallel (LPPDSx) and transverse (LPPDSz) polarization components with respect to the film surface are plotted in fig. 5.23 and reveal the surface nature of the RW and the pseudo-surface features of the LR wave. These simulations do not show the LB wave because they compute only the acoustic spectrum without considering the electromagnetic interaction. The analysis of these plots confirms our assumptions on the nature of the observed peaks, showing the positions of the transverse and longitudinal thresholds and pointing out that the LR wave is bounded partially at the

surface but extends partially also in the bulk. The RW has an exclusive surface nature and its peak is the result of the interference effect between the ripple scattering mechanism, active only for the transverse polarization component, and the elasto-optic effect, while the LR peak is visible only through the elasto-optic channel [105-107].

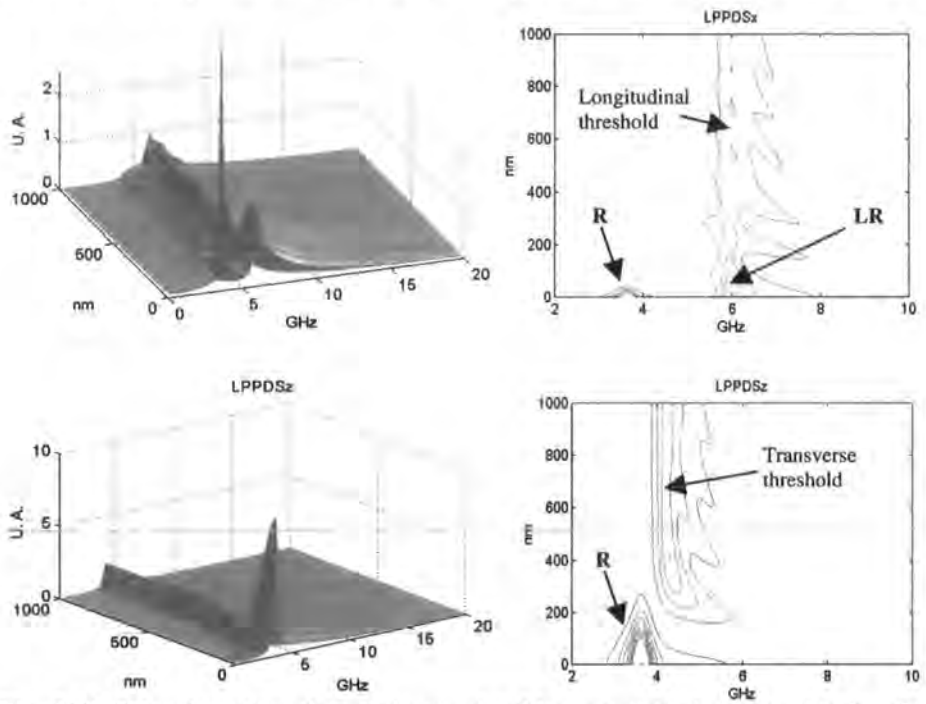

Fig. 5.23: 3D and contour plots of the simulated layer projected phonon density of state LPPDS for the polarization component perpendicular to the surface (LPPDSz, bottom graphs) and parallel to the surface (LPPDSx, top graphs) showing the RW and LR depth behaviour. The longitudinal and transverse thresholds between the discrete and continuum regions of the spectrum are also shown in these plots (courtesy C. Casari, Politecnico di Milano).

Finally, a series of thin films with thickness varying in the range 60 nm–400 nm was deposited with focused beams and measured for comparison with the series 1, 2 and 3 grown in standard configuration, without focusing (see fig. 5.24 and fig. 5.20). The difference is that now, although the nature of the detected surface modes is the same, there is no central peak. This must be ascribed to the compact nature of these films and to the smooth surface. AFM measurements have revealed that in this films the surface roughness is one order of magnitude smaller than in non-focused beams [17] (even in the periphery of a non-focused beam, despite the inertial separation effect, some big particles are probably present, which are instead eliminated by using the "focusing" device; moreover the divergence of a non-focused beam is much higher).

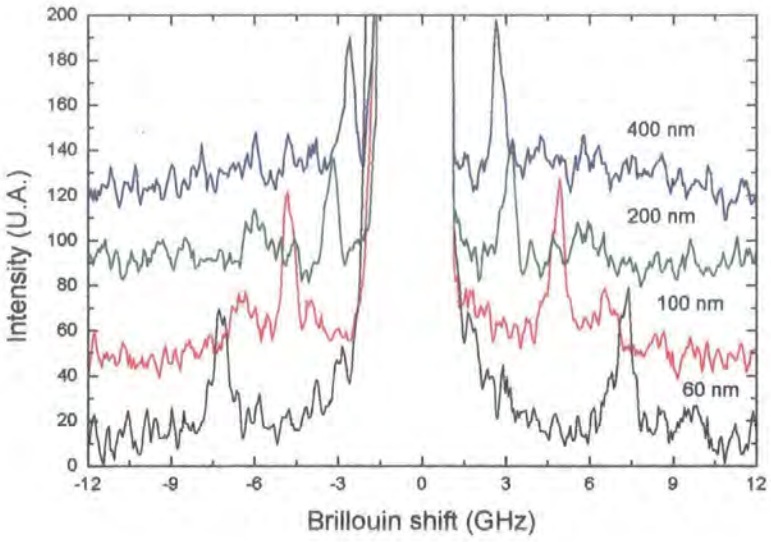

Fig. 5.24: Brillouin spectra from films deposited using a focused beam and having different thickness. In these measurements the incidence angle is 50^{O}. See for comparison fig. 5.20.

5.6 Disorder and confined modes

In disordered materials acoustic waves can be localized; the breaking of the translational symmetry does not allow the propagation of phonons as plane waves. A weak localization can be described by introducing a finite phonon lifetime, i.e. a broadening of the corresponding phonon peak in Brillouin measurements. This corresponds to an acoustic wave damping over a characteristic damping length (see also chapter 6 for damping of acoustic modes in metallic nanospheres). For strong localization the acoustic wave does not exist and localized, confined vibrational states can be excited.

A particular type of localization exists in materials with a fractal or self-similar organisation (see e.g. [108-114]). Many materials have been shown to possess a fractal-like static structure in a length interval defined by the lower and upper characteristic lengths ξ_1 and ξ_2 (see section 2.7 and [99]), for example using Small Angle X-ray or Neutron Scattering (SAXS or SANS), or even Small Angle Light Scattering. In this case the localized vibrational states have been studied and excitations possessing a dynamical fractal nature have been called "fractons". These modes are observed when studying the materials over dynamical lengths in the range ξ_1-ξ_2; phonons with wavelength larger than ξ_2 can propagate as they see the material as a homogeneous

effective medium. Several studies by Raman and particularly Brillouin spectroscopy have been devoted to investigate the presence of such excitations.

Since the SEM pictures of the cluster-assembled carbon films reveal a structure that resembles that of self-similar systems, and since AFM measurements have shown the same film to possess a self-similarly organised surface roughness [17], it appeared natural to investigate whether these materials have a volume fractal structure or can host fractons. In particular AFM studies [17] have shown that the growth of the cluster-assembled carbon films implies a columnar growth due to a ballistic deposition with shadowing effects, with self-affine properties in the height-height correlation function and in the scaling of roughness with deposition time (see also [99]).

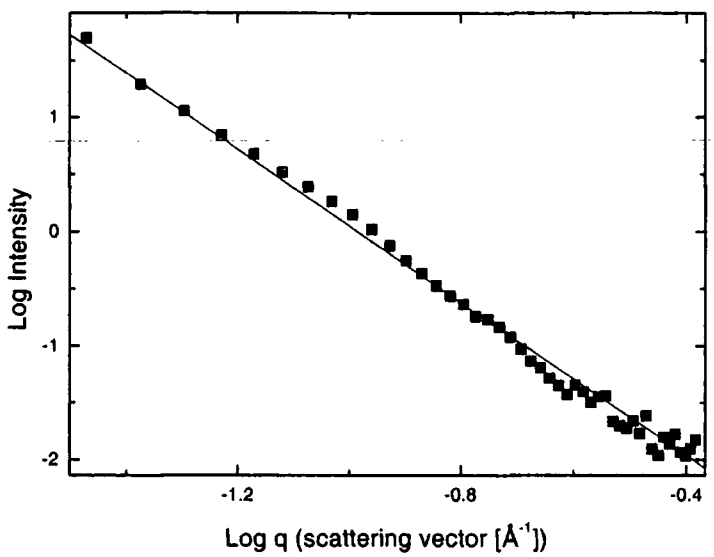

Fig. 5.25: Small Angle X-ray Scattering (λ=1.3 Å), after subtraction of background, from a cluster-assembled carbon film grown under standard deposition conditions, down to a scattering wavevector value of $4\pi\sin\theta/\lambda$ = 0.025 Å^{-1}, corresponding to a length of about 25 nm. A linear fit is shown, corresponding to an exponent value of about 3.3.

SAXS experiments have been performed to investigate this on station SRS 2.3 at Daresbury. Scattering wavevectors down to 0.025 Å^{-1} were investigated (fig. 5.25), which means that structures up to a length of about 25 nm were studied. The exponent found (see Eqs. (2.57) and (2.58)) was about 3.2-3.3. Thus, there is no clear evidence of a self-similar volume structure, at least up to this length scale. We could interpret this result as the scattering from a fractal surface with fractal dimension 2.7-2.8, which is indeed possible for films showing a structure like that revealed by SEM pictures (fig.

5.4). To analyse this over larger lengths, one should be able to study smaller scattering wavevectors, maybe using a dedicated beamline, or even Small Angle Light Scattering (i.e. a larger wavelength).

It has been shown (see e.g. [112-114]) that in inelastic light scattering the excitation of fractons should reveal itself in the presence of a low frequency scattering intensity following a power law:

$$I(\nu) \propto \nu^{\alpha} \qquad (5.8)$$

where the exponent α depends on the fractal dimension of the system and on a "dynamical" fractal dimension. Different models give different expressions for α. Unfortunately, these measurements are very difficult, because the presence of the elastic laser peak and the background diffuse intensity strongly affect the exponent determination. The central peak in our Brillouin measurements was investigated, but no definitive evidence of such a dynamical behaviour could be found for our material so far. Nevertheless, the evolution of the central peak with thickness in BS experiments and the thickness-dependent roughness evidenced by AFM analysis suggest that the localization mechanism is governed more by the irregular surface features than by volume effects.

5.7 Conclusions

In this chapter the Raman and Brillouin scattering characterisation of cluster-assembled carbon films (from the deposition of supersonic cluster beams produced by a Pulsed Microplasma Cluster Source) has been presented, together with x-ray scattering characterisation.

Being Raman spectroscopy a fast and standard technique for amorphous carbon characterisation, its use was indispensable to study the functioning of the source in different configurations and to relate it to the properties of the deposited films. Wide-angle x-ray scattering and Raman scattering showed the amorphous nature of the carbon films. On the other hand, rather ordered forms of carbon (onion-like particles, graphitic particles, nanotubes) were found to be formed in the source cavity. Raman scattering measurements confirmed the possibility of growing films with different local bonding topology by exploiting the inertial separation effect occurring in supersonic cluster beams, and thus tuning the size distribution of the deposited clusters.

The possibility of enhancing the focusing of the cluster beam, in order to deposit smaller clusters and grow more compact, smoother films, was indirectly confirmed by Brillouin scattering experiments. These measurements also permitted the determination of the elastic properties of the carbon films, revealing a very soft material. I would like to remember that the determination of the elastic constants in thin films and the evaluation of the elasto-optic coefficients in the focused film have been carried out by C. Casari at Politecnico di Milano [100].

The possibility of a self-affine or fractal structure of the films was investigated by Brillouin scattering and Small-Angle X-ray Scattering, though no conclusive evidence was obtained.

A general review of the complete work so far within the cluster-assembled carbon films project, together with some investigation of the control of the film nanostructure in view of possible applications (field emission, catalysis, and gas adsorption) can be found in refs. [5, 10, 11, 15-25]. At the moment of the submission of this thesis, a portable deposition apparatus (CLARA: CLuster Assembling Roaming Apparatus) has been designed and built, to be used for in-situ characterisation of the first stages of growth during thin film deposition. The contribution of the Materials Laboratory at Politecnico di Milano will be in the in-situ Raman scattering characterisation of the very first stages of growth. A UHV chamber with a micromanipulator and the possibility of interface with the Raman spectrometer and with CLARA has already been designed and assembled (see section 3.1.2), and the first experiments are about to be performed.

References for Chapter 5:

[1] R.W. Siegel, Mater. Sci. Eng. B **19**, 37 (1993)

[2] H. Gleiter, Prog. Mater. Sci. **33**, 223 (1989)

[3] A. Perez, P. Melinon, V. Dupuis, P. Jensen, B. Prevel, J. Tuaillon, L. Bardotti, C. Martet, M. Treilleux, M. Broyer, M. Pellarin, J.L. Vialle, B. Palpant, J. Lerme, J. Phys. D: Appl. Phys. **30,** 709 (1997)

[4] M. Ehbrecht, H. Ferkel, F. Huisken, Z. Phys. D **40**, 88 (1997)

[5] P. Milani, S. Iannotta, "Synthesis of Nanophase Materials by Cluster Beam Deposition", Springer, Berlin (1999)

[6] P. Milani and P. Piseri, in "Application of Accelerators in Research and Industry", edited by J. L. Duggan and I. L. Morgan, AIP Conf. Proc. **392**, 495 (1997)

[7] P. Melinon, V. Paillard, V. Dupuis, A. Perez, P. Jensen, A. Hoareau, J.P. Perez, J. Tuaillon, M. Broyer, J.L. Vialle, M. Pellarin, B. Baguenard, J. Lerme, Int. J. Mod. Phys. B **9**, 339 (1995)

[8] V. Paillard, P. Melinon, V. Dupuis, J.P. Perez, A. Perez, B. Champagnon, Phys. Rev. Lett. **71**, 4170 (1993)

[9] I. Yamada, Nucl. Instrum. Methods Phys. Res. B **112**, 242 (1996)

[10] E. Barborini, P. Piseri, S. Mutti, P. Milani, F. Biasioli, S. Iannotta, S. Gialanella, Nanostructured Materials **10,** 1023 (1998)

[11] E. Barborini, P. Piseri, A. Li Bassi, A.C. Ferrari, C.E. Bottani, P. Milani, Chem. Phys. Lett. **300,** 633 (1999)

[12] E. Barborini, P. Piseri, P. Milani, Journal of Physics D-Applied Physics **32,** L105 (1999).

[13] P. Piseri, A. Li Bassi, P. Milani, Rev. Sci. Instr. **69,** 1647 (1998)

[14] P. Piseri, S. Iannotta, P. Milani, Int. J. Mass Spectrom. Ion Processes **153**, 23 (1996)

[15] C.E. Bottani, A.C. Ferrari, A. Li. Bassi, P. Milani, M. Ferretti, P. Piseri, Carbon **36,** 535 (1998)

[16] C.E. Bottani, A.C. Ferrari, A. Li Bassi, P. Milani, P. Piseri, Europhys. Lett. **42,** 431 (1998).

[17] R. Buzio, E. Gnecco, C. Boragno, U. Valbusa, P. Piseri, E. Barborini, P. Milani, Surf. Sci. **444,** L1 (2000).

[18] L. Diederich, E. Barborini, P. Piseri, A. Podesta, P. Milani, A. Schneuwly, R. Gallay, Appl. Phys. Lett. **75,** 2662 (1999).

[19] C. Lenardi, P. Piseri, V. Briois, C. E. Bottani, A. L. Bassi, P. Milani, J. Appl. Phys. **85,** 7159 (1999).

[20] A. Li Bassi, P. Piseri, P. Milani, A. Ferrari, C. E. Bottani, C. Cepek, L. Giovanelli, E. Magnano, M. Sancrotti, Surf. Sci. **404,** 441 (1998).

[21] P. Milani, Rivista Del Nuovo Cimento **19,** 1 (1996).

[22] P. Milani, E. Barborini, P. Piseri, C.E. Bottani, A.C. Ferrari, A. Li Bassi, European Physical Journal D **9,** 63 (1999)

[23] P. Milani, M. Ferretti, P. Piseri, C.E. Bottani, A. Ferrari, A. Li Bassi, G. Guizzetti, M. Patrini, J. Appl. Phys. **82,** 5793 (1997).

[24] I. Boscolo, P. Milani, M. Parisotto, G. Benedek, F. Tazzioli, J. Appl. Phys. **87**, 4005 (2000).

[25] A.C. Ferrari, B.S. Satyanarayana, J. Robertson, W.I. Milne, E. Barborini, P. Piseri, P. Milani, Europhysics Letters **46**, 245 (1999)

[26] D. Donadio, L. Colombo, P. Milani, G. Benedek, Phys. Rev. Lett. **83**, 776 (1999)

[27] D.R. Miller, in "Atomic and Molecular Beam Methods", Ed. G. Scoles, Oxford University Press, New York (1988), p. 14.

[28] D. Eres, D.H. Lowndes, J.Z. Tischler, Appl. Phys. Lett. **55**, 1008 (1989)

[29] J.R. Engstrom, L.-Q. Xia, M.J. Furjanic, D.A. Hansen, Appl. Phys. Lett. **63**, 1821 (1993)

[30] G. Gantefoer, H.R. Siekmann, H.O. Lutz, K.H. Meiwes-Broer, Chem. Phys. Lett. **165**, 293 (1990)

[31] P. Milani and W.A. de Heer, Rev. Sci. Instrum. **61**, 1835 (1990)

[32] W.R. Gentry, in "Atomic and Molecular Beam Methods", Ed. G. Scoles, Oxford University Press, New York (1988), p. 54

[33] V.H. Reis, J.B. Fenn, J. Chem. Phys. **39**, 3240 (1963)

[34] E.W. Becker, K. Bier, Z. Naturforsch. **9a**, 975 (1954)

[35] P.C. Waterman, S.A. Stern, J. Chem. Phys. **31**, 405 (1959)

[36] J. Fernandez de la Mora, B.L. Halpern, J.A. Wilson, J. Fluid Mech. **149**, 217 (1984)

[37] P. Milani, P. Piseri, E. Barborini, patent pending

[38] A.C. Ferrari, J. Robertson, Phys. Rev. B **61**, 14095 (2000)

[39] D.S. Knight, W.B. White, J. Mater. Res. **4**, 385 (1989)

[40] F. Tuinstra, J.L. Koening, J. Chem. Phys. **53**, 1126 (1970)

[41] R. J. Nemanich, S. A. Solin, Phys. Rev. B **20**, 392 (1979).

[42] P. Lespade, R. Al-Jishi, M.S. Dresselhaus, Carbon **20**, 427 (1982).

[43] P. Lespade, A. Marchard, M. Couzi, F. Cruege, Carbon **22**, 375 (1984).

[44] N. Wada, P.J. Gaczi, A. Solin, J. Non-Cryst. Solids **35&36**, 543 (1980)

[45] R.O. Dillon, J.A. Woollam, V. Katkanant, Phys. Rev. B **29**, 3482 (1984).

[46] J. Wagner, M. Ramsteiner, C. Wild, P. Koidl, Phys. Rev. B **40**, 1817 (1989).

[47] M.A. Tamor, W.C. Vassel, J. Appl. Phys. **76**, 3823 (1994)

[48] J. Schwan, S. Ulrich, V. Bathori, H. Erhardt, S. R. P. Silva, J. Appl. Phys. **80**, 440 (1996).

[49] K.W.R. Gilkes, H.S. Sands, D.N. Batchelder, J. Robertson, W.I. Milne, Appl. Phys. Lett. **70**, 1980 (1997)

[50] V.I. Merkulov, J.S. Lannin, C.H. Munro, S.A. Asher, V.S. Veerasamy, W.I. Milne, Phys. Rev. Lett. **78**, 4869 (1997)

[51] F. Li, J. S. Lannin, Appl. Phys. Lett. **61**, 2116 (1992)

[52] D. Lin-Vien, N. B. Colthurp, W. G. Fateley, J. G. Grasselli, "The Handbook of Infrared and Raman Characteristic Frequencies of Organic Molecules", Academic, New York (1991)

[53] R.P. Vidano, D.B. Fishbach, L. J. Willis, T.M. Loehr, Solid State Commun. **39**, 341 (1981)

[54] I. Pocsik, M. Hundhausen, M. Koos, L. Ley, J. Non-Cryst. Solids **227–230**, 1083 (1998)

[55] M.J. Matthews, M.A. Pimenta, G. Dresselhaus, M.S. Dresselhaus, M. Endo, Phys. Rev. B **59**, 6585 (1999).

[56] D.G. McCulloch, S. Prawer, A. Hoffman, Phys. Rev. B **50**, 5905 (1994).

[57] D.G. McCulloch, S. Prawer, J. Appl. Phys. **78**, 3040 (1995)

[58] S. Prawer, K.W. Nugent, Y. Lifshitz, G.D. Lempert, E. Grossman, J. Kulik, I. Avigal, R. Kalish, Diamond Relat. Mater. **5**, 433 (1996)

[59] M.V. Klein, in "Light Scattering in Solids III", edited by M. Cardona and G. Guntherodt, Topics in Applied Physics Vol. 51, Springer-Verlag, Berlin (1982).

[60] A. Cuesta, P. Dhamelincourt, J. Laureyns, A. Martinez-Alonso, J.M.D. Tascon, J. Mater. Chem. **8**, 2875 (1998)

[61] B.S. Elman, M. Shayegan, M.S. Dresselhaus, H. Mazurek, G. Dresselhaus, Phys. Rev. B **25**, 4142 (1982)

[62] R. Shuker, R.W. Gammon, Phys. Rev. Lett. **25**, 222 (1970)

[63] M. Akagi, H. Nishiguchi, H. Shirakawa, Synth. Metals **17**, 557 (1987)

[64] M. Nakamizo, R. Kammereck, P.L. Walker, Carbon **12**, 259 (1974)

[65] A. Canning, G. Galli, J. Kim, Phys. Rev. Lett. **78**, 4442 (1997)

[66] G. Benedek, L. Colombo, Mater. Sci. Forum **232**, 247 (1996)

[67] B.E. Warren, Phys. Rev. **59**, 693 (1941)

[68] A.I. Cuesta Sejo, Ph.D. Thesis, Universidad de Oviedo (1994)

[69] C.S. Sundar, Y. Hariharan, A. Bharathi, M. Premila, V.S. Sastry, G.V.N. Rao, J. Janaki, D.V. Natarajan, K.V. Devadhasan, T.S. Radhakrishnan, N. Subramanian, P.C.

Sahu, M. Yousuf, S. Raju, V.S. Raghunathan, M.C. Valsakumar, Prog. Crystal Growth and Charact. **34**, 11 (1997)

[70] J.A. Nisha, J. Janaki, V. Sridharan, G. Padma, M. Premila, T.S. Radhakrishnan, Thermochimica Acta **286**, 17 (1996)

[71] H.P. Klug, L.E. Alexander, "X-Ray Diffraction Procedures for Polycrystalline and Amorphous Materials", Wiley, New York (1974)

[72] S. Tomita, M. Fujii, S. Hayashi, K. Yamamoto, Diam. Relat. Mater. **9**, 856 (2000)

[73] P.M. Ajayan, T.W. Ebbesen, Reports On Progress in Physics **60,** 1025 (1997)

[74] P. Milani, Riv. Nuovo Cimento **19**, 1 (1996)

[75] D.T. Colbert, J. Zhang, S.M. McClure, P. Nikolaev, Z. Chen, J.H. Hafner, D.W. Owens, P.G. Kotula, C.B. Carter, J.H. Weaver, A.G. Rinzler, R.E. Smalley, Science **266,** 1218 (1994)

[76] T.W. Ebbesen, H. Hiura, J. Fujita, Y. Ochai, S. Matsui, S.K. Tanigaki, Chem. Phys. Lett. **209** 83, (1993)

[77] W.S. Bacsa, W.A. DeHeer, D.Ugarte, A. Chatelain, Chem. Phys. Lett. **211,** 346 (1993)

[78] E.D. Obraztsova, M. Fujii, S. Hayashi, V.L. Kuznetsov, Y.V. Butenko, A.L. Chuvilin, Carbon **36**, 821 (1998)

[79] J.M. Holden, Z. Ping, X.X. Bi, P.C. Eklund, S.J. Bandow, R.A. Jishi, K. Daschowdhury, G. Dresselhaus, M.S. Dresselhaus, Chem. Phys. Lett. **220,** 186 (1994)

[80] H. Hiura, T.W. Ebbesen, K. Tanigaki, H. Takahashi, Chem. Phys. Lett. **202,** 509 (1993)

[81] W.S. Bacsa, D. Ugarte, A. Chatelain, W.A. Deheer, Phys. Rev. B **50,** 15473 (1994)

[82] W.Z. Li, H. Zhang, C.Y. Wang, Y. Zhang, L.W. Xu, K. Zhu, S.S. Xie, Appl. Phys. Lett. **70,** 2684 (1997)

[83] J. Kastner, T. Pichler, H. Kuzmany, S. Curran, W. Blau, D.N. Weldon, M. Delamesiere, S. Draper, H. Zandbergen, Chem. Phys. Lett. **221,** 53 (1994)

[84] P.V. Huong, R. Cavagnat, P.M. Ajayan, O. Stephan, Phys. Rev. B **51,** 10048 (1995)

[85] A.M. Rao, E. Richter, S. Bandow, B. Chase, P.C. Eklund, K.A. Williams, S. Fang, K.R. Subbaswamy, M. Menon, A. Thess, R.E. Smalley, G. Dresselhaus, M.S. Dresselhaus, Science **275,** 187 (1997)

[86] C. Journet, W.K. Maser, P. Bernier, A. Loiseau, M.L. delaChapelle, S. Lefrant, P. Deniard, R. Lee, J. E. Fischer, Nature **388,** 756 (1997)

[87] W.S. Bacsa, J.S. Lannin, D.L. Pappas, J.J. Cuomo, Phys. Rev B **47**, 10931 (1993)

[88] R.A. Jishi, L. Venkataraman, M.S. Dresselhaus, G. Dresselhaus, Chem. Phys. Lett. **209**, 77 (1993)

[89] P. Piseri, Ph.D. Thesis, Universita' di Milano (1999)

[90] S. Yang, K.J. Taylor, M.J. Craycraft, J. Conceicao, C.L. Pettiette, O. Cheshnovsky, R.E. Smalley, Chem. Phys. Lett. **144**, 431 (1988)

[91] P. Dugourd, R.R. Hudgins, J.M. Tenenbaum, M.F. Jarrold, Phys. Rev. Lett. **80**, 4197 (1998)

[92] R.O. Jones, G. Seifert, Phys. Rev. Lett. **79**, 443 (1997)

[93] J.H. Kaufman, S. Metin, D.D. Saperstein, Phys. Rev. B **39**, 13053 (1989)

[94] R.J. Lagow, J.J. Kampa, H.C. Wei, S.L. Battle, J.W. Genge, D.A. Laude, C.J. Harper, R. Bau, R.C. Stevens, J.F. Haw, E.L. Munson, Science **267**, 362 (1995)

[95] M. Kijima, Y. Sakai, H. Shirakawa, Synthetic Metals **71**, 1837 (1995)

[96] A. Li Bassi, A.C. Ferrari, V. Stolojan, B.K. Tanner, J. Robertson, L.M. Brown, Diam. Relat. Mater. **9**, 771 (2000)

[97] M. Manfredini, C.E. Bottani, P. Milani, J. Appl. Phys. **78** (10), 5945 (1995)

[98] P. Milani, C.E. Bottani, A. Parisini, G.P. Banfi, Appl. Phys. Lett. **72** (3), 293 (1998)

[99] A.L. Barabasi, H.E. Stanley, "Fractal concepts in Surface Growth", Cambridge University Press, Cambridge (1995)

[100] C. Casari, Degree Thesis (Tesi di Laurea), Politecnico di Milano (1999)

[101] M. Grimsditch, J. Phys. C **16**, L143 (1983)

[102] G.W. Farnell, "Properties of Elastic Surface Waves", in "Physical Acoustics", vol. 6, edited by W. P. Mason and R. N. Thurston, Academic Press, New York (1970)

[103] A. Amici, M.G. Beghi, C.E. Bottani, Computational Material Science **17**, 404 (2000)

[104] M. Beghi, C.E. Bottani, P.M. Ossi, T. Lafford, B.K. Tanner, J. Appl. Phys. **81**, 672 (1997)

[105] P. Milani, C.E. Bottani, "Vibrational Properties of Mesoscopic Structures", in "Handbook of Nanostructured Materials and Nanotechnology", Academic Press (1998)

[106] J.R. Sandercock, "Trend in Brillouin Scattering: Studies of Opaque Materials, Supported Films and Central Modes", in "Light Scattering in Solids III", edited by M. Cardona and G. Guntherodt, Springer-Verlag, Berlin (1982)

[107] P. Mutti, C.E. Bottani, G. Ghislotti, M.G. Beghi, G.A.D. Briggs, J.R. Sandercock in "Advances in Acoustic Microscopy", Vol.1, Ed. A. Briggs, Plenum Press, New York (1995), p.249

[108] V.V. Zosimov, L.M. Lyamshev, Physics-Uspekhi **38**, 347 (1995)

[109] S. Alexander, R. Orbach, J. Physique **43**, L625 (1982)

[110] A. Aharony, O. Entin-Wohlman, S. Alexander, R. Orbach, Phil. Mag. B **56**, 949 (1987)

[111] T. Nakayama, K. Yakubo, R.L. Orbach, Rev. Mod. Phys. **66**, 381 (1994)

[112] S. Alexander, Phys. Rev. B **40**, 7953 (1989)

[113] Y. Tsujimi, E. Courtens, J. Pelous, R. Vacher, Phys. Rev. Lett. **60**, 2757 (1988)

[114] A. Boukenter, B. Champagnon, E. Duval, J.L. Rousset, H.M. Rosenberg, Phil Mag. B **59**, 125 (1989)

Chapter 6

Melting of tin nanoparticles

6.1 Introduction

Nanoparticles have recently been the object of intensive work, both in the case of semiconductor quantum dots and metal nanocrystals [1-4]. Their properties differ from the bulk material properties, and strongly depend on their size. The main motivation for the growing interest in these systems is thus related to the possibility of tailoring their physical behaviour by tuning and controlling the nanoparticle size.

For metal nanoparticles above a particle radius about 10 Å the width of the discrete electron energy levels becomes comparable or larger than the separation between them. As a result, the conduction band becomes quasi continuous. When the radius R becomes ≥ 200 Å the behaviour of the nanoparticles progressively approaches that of the bulk metal [4]. In the intermediate size range 10 Å < R < 200 Å, significant deviations with respect to the bulk properties are observed, for example, in thermodynamic properties such as melting temperature and latent heat of fusion (see e.g. [5] and references therein), as well as optical properties.

When the ratio of the number of surface atoms to the total number of atoms exceeds 1:3 the melting temperature of the particles decreases to about 2/3 T_0 [6], since the reduced number of bonds on the surface causes an enhancement of thermal vibration. The melting temperature T_M of a particle of radius R has been described by Semenchenko [7, 8] from a classical point of view. For R > 15 nm he predicted:

$$T_M = T_0 \exp\left(-\frac{2\gamma_{sl}}{\rho L R}\right) \tag{6.1}$$

where T_0 is the bulk melting temperature, ρ the volume mass density, L the latent heat of fusion and γ_{sl} the interfacial free energy between solid and liquid (difference between the solid and the liquid surface tensions γ_s and γ_l). A simple thermodynamical approach can model the reduction of the melting point and is based on the surface tension difference between the liquid and the solid phases. A key point in the discussion is that, according to the Laplace law, the pressure on the surface of a small liquid droplet is different from the external pressure, and the pressure difference is

given by $\Delta p = p_l - p_{ext} = 2\gamma_l / R$ (i.e. in a sphere the surface tension creates a compressive force). A similar relationship is valid for a solid sphere, with γ_s instead of γ_l. Eq. (6.1) (or similar relationships) is obtained imposing that the melting will occur when the chemical potentials of the solid and of the liquid phase are equal. For smaller sizes, different approaches have been adopted (e.g. molecular dynamics simulations [9, 10]). In any case, experimentally it is well established [10] that

$$\frac{\Delta T}{T} = \frac{T_0 - T_M}{T_0} \approx \frac{1}{R} \tag{6.2}$$

which is simply the first order term in the series expansion of Eq. (6.1).

The interface energy balance explains the phenomenon of surface melting, which takes place if $\gamma_{sv} - \gamma_{sl} - \gamma_{lv} > 0$, where γ_{sv}, γ_{sl} and γ_{lv} are the solid-vapour, solid-liquid and liquid-vapor interfacial free energies [11]. In this case a thin liquid layer can exist considerably below the melting temperature of the whole particle, which, as stated above, turns out to be considerably lower than the bulk melting temperature. In addition, the phase transition is characterized by a hysteresis cycle [12] over a temperature range which can in some cases attain 150 K [3], which shows that melting takes place at temperatures above solidification (except for the very small sizes, where the hysteresis cycle disappears). The size dependence of the melting temperature has been observed experimentally [5, 10, 13-20] using X-ray diffraction [13, 19, 20], transmission electron microscopy and optical reflectance [5, 10, 14].

In this chapter, the use of in-situ high-temperature high-resolution x-ray powder diffraction to study the phase transition as a function of particle size is reported. The results are related to the measurement of a modified surface Rayleigh acoustic phonon in a supported SiO_x film containing Sn nanoparticles, using Brillouin inelastic light scattering. The melting transition does indeed occur at the same temperature as an abrupt redshift in the Brillouin peak; the melting temperature has then been related to the measured size of the particles. In the second part, some Raman scattering and low-frequency Raman scattering characterization will be presented, showing the detection of optical phonon modes and acoustic modes associated with the vibration of the nanoparticles.

6.2 Description of the samples and sample growth

The samples studied in this work contained Sn nanoparticles, and were deposited onto a Si (100) oriented substrate. The nanoparticles were embedded in a SiO_x (silica) amorphous matrix and were prepared by means of an evaporation-condensation technique in ultra-high vacuum (UHV) conditions [21], by P.Cheyssac and R. Kofman of the Condensed Matter Physics Laboratory (University of Nice). On a substrate kept at high temperature, a film of amorphous material is evaporated. After evaporation, the material constituting the nanocrystals is deposited on top so that its vapour is condensed on the underlying dielectric layer. The amorphous nature of the dielectric layer and its non-wetting or partially wetting character with respect to the nanocrystals are essential characteristics of the technique, together with the absence of strong perturbations due to chemical etching or mechanical distortions. During evaporation, the temperature of the substrate is kept at such a value that nucleation of nanoparticles takes place in the liquid phase, so that the surface tension plays a dominant role in determining the shape of the nanodroplets, which is approximately that of a truncated sphere. The liquid state of the deposit is an important step in the growth process, since it results in particles with a high degree of regularity. The temperature of the substrate is then lowered, so that the nanodroplets are frozen in the solid state, before being covered by an additional protecting amorphous layer; in this way, size and shape are kept constant. In order to improve the signal-to-noise ratio in the measurements, the total quantity of nanoparticles is usually increased by replicating the above-described depositions many times.

If a small quantity of liquid material A is deposited on a substrate of a species B, the intermolecular forces resulting in the surface free energy and the interfacial energies will lead to the optimisation of surface area in relation to the interfacial energy between A and B. Consequently, a particle of material A will not be able to take an arbitrary shape on the substrate B. The equilibrium is described by the Young equation [21]:

$$\gamma_B = \gamma_{AB} + \gamma_A \cos\varphi \qquad (6.3)$$

where φ is the contact angle between the two surfaces, γ_A and γ_B are the surface free energies of A and B respectively and γ_{AB} is the interfacial energy. In a real sample a wide range of contact angles can be found, due to the nature of the substrate (roughness, defects, etc.). One can distinguish three cases:

i) there is a flat layer instead of the particle ($\varphi = 0$, complete wetting);

ii) the particle has a contact angle ($0° < \varphi < 90°$, partial wetting; $90° < \varphi < 180°$, partial non wetting), generating a truncated sphere;

iii) the particle is completely spherical ($\varphi = 180°$, complete non wetting).

In our samples $\varphi \sim 90°$, so that the particles have an approximately half-spherical shape [22].

The size distribution is bimodal (presenting an interesting similarity with other techniques) [21]. Its larger portion ($\approx$ 95% in volume) is gaussian-like and has a relatively low size dispersion and a bell-like shape; a weak tail is also present at smaller sizes. By changing the growth parameters mean particle diameters between ten and a few thousand Ångstroms can be produced. The parameter used to indicate the deposited nanoparticle material quantity in each layer is the so-called equivalent thickness, i.e. the thickness of a film containing the same volume of material, supposed to be continuous.

Two series of samples were deposited and then studied. In the first series two samples were deposited with the same overall amount of Sn, but different nominal sizes: 2.5 nm (sample *SnA*, equivalent thickness 1.25 nm) and 20 nm (*SnB*, e.t. 10 nm). The overall thickness was 186 nm for both samples. For the second series, three different samples were deposited, each with the same volume amount of Sn but with different nanoparticle nominal sizes: 2.5 nm (sample *Sn1*, equivalent thickness 1.25 nm); 10 nm (*Sn2*, e.t. 5 nm); 20 nm (*Sn3*, e.t. 10 nm). The overall thickness was 186 nm for all the samples. A blank sample of SiO_x, 186 nm thick, without Sn, was deposited for reference purposes (sample *Snref*).

As the experiment involved use of expensive synchrotron radiation beamtime, the two samples of the first series were used for fast and preliminary measurements [23] in order to design the best experimental conditions for accurate measurements, which were performed on the samples of the second series. In the following only these final results, which were entirely consistent with the preliminary measurements, will be discussed.

6.3 Brillouin scattering

Inelastic light scattering has been widely used to study phase transitions [24]. Yet, to the best of our knowledge, the melting of neither a bulk crystal nor a nanocrystal has ever been examined in detail by this technique.

For all the samples the geometry of the system was designed to measure only one phonon peak at a fixed incidence angle. This peak is associated with a modified Rayleigh phonon propagating parallel to the surface and probing both the film and the substrate to a depth of the order of 270-300 nm with the vanishing tail of its displacement field. When the tin particles melt, their shear modulus drops discontinuously to a negligible value and the inverse of their bulk modulus jumps to the value of the finite compressibility of the liquid. This corresponds globally to a lowering of the effective elastic constants of the film. Thus the phase velocity of the surface phonon decreases abruptly inducing a redshift in the Brillouin peak position. In this way the melting temperature can be detected.

Surface Brillouin scattering data were recorded in a backscattering geometry at a fixed incidence angle (60° or 70°), for all the samples and all the different temperatures, using the Sandercock six-pass tandem Fabry-Perot interferometer described in section 3.2.1. For the temperature control the samples were placed inside the Oxford Instruments cryothermostat, with optical windows. The spectra were measured at different temperatures in the range 293-533 K, with a step size of 10 K and with a laser power of 40 mW incident onto the sample surface. This power was low enough not to enhance significantly the sample local temperature. Due to wave-vector conservation, surface phonons contributing to Brillouin scattering have a parallel wavelength (see chapter 2):

$$\lambda_{||} = \lambda_0/(2sin\theta) \qquad (6.4)$$

(which is 297 nm for incidence angle $\theta_i = 60°$ and 274 nm for $\theta_i = 70°$, for the argon ion laser wavelength $\lambda_0 = 514.5$ nm). The acquisition time for each measurement was about 2 hours. For surface acoustic waves the measured Brillouin shift ν_{BS} is proportional to the wave velocity v_{SAW} when the geometry of the experiment (i.e. the incidence angle θ_i) is fixed, according to Eq. (2.38). We thus refer in the following only to the Rayleigh peak frequency.

In fig. 6.1 Brillouin spectra from the sample *Sn3* are shown. They correspond to three different temperatures (293 K room temperature, 473 K just below melting, 493 K just beyond melting). Two features are important, a Rayleigh peak whose shift is about 9 GHz (undergoing a redshift beyond 473 K), and a central peak whose intensity (and FWHM) was not constant with temperature.

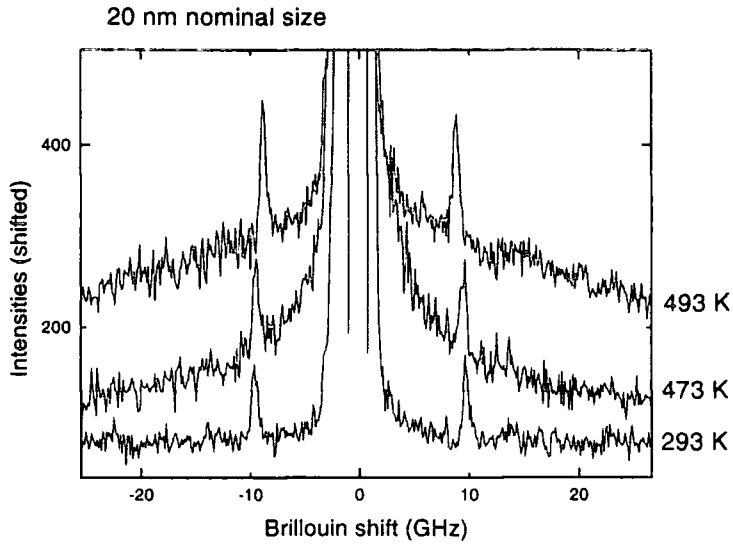

Fig. 6.1: Brillouin scattering for sample *Sn3* at three different temperatures: room, before and after melting. Note the shift of the Rayleigh peak and the rise of a central feature.

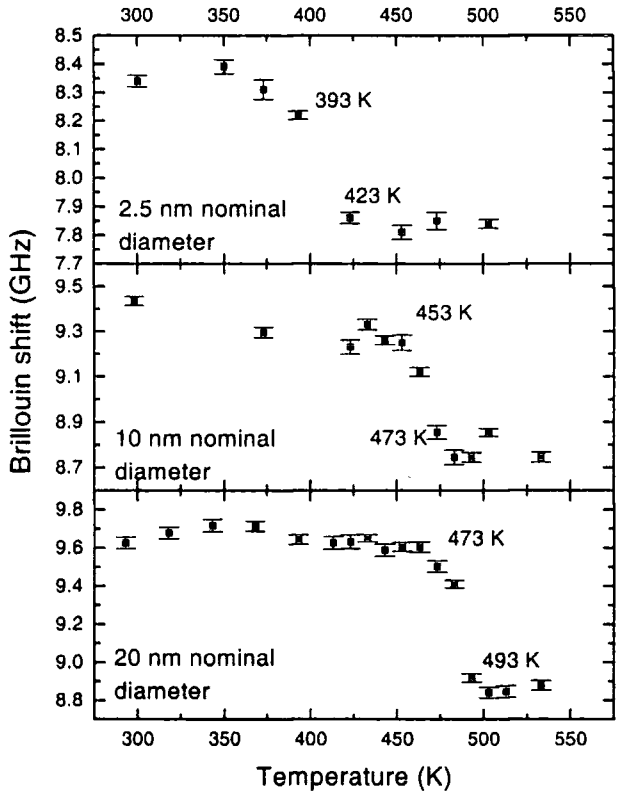

Fig. 6.2: Position of the Rayleigh peak as a function of temperature in sample *Sn1* (top graph), *Sn2* (middle) and *Sn3* (bottom).

In fig. 6.2 we show the experimental Rayleigh peak position as a function of temperature for each of the three samples. These positions correspond in sample *Sn3* to

a wave velocity variation from 2850 m/s to 2600 m/s. After an initially gradual variation, the final shift drop is rather sharp (it happens in a small temperature range of about 20 K) and it is always in the range 0.6-0.9 GHz. The transition temperature is between 473 and 493 K for sample *Sn3*, 453-473 K for sample *Sn2* and 393-423 K for sample *Sn1* (see Table 6.1 below). These values can be compared with the melting temperature of bulk tin, which is 505 K (232 °C).

The wavelength $\lambda_{\|}$ of the Rayleigh phonon is much larger than the particle radius and so it is possible to avoid a detailed description of the phonon-particle scattering. One can treat the film as an effective medium with average elastic properties. The effective elastic constants B and μ (bulk and shear modulus, respectively) of a film with spherical inclusions can be obtained within the Voigt-Reuss-Hill approximation [25] by the formulae

$$B = B_2 - f_1(B_2 - B_1)\frac{3B_2 + 4\mu_2}{3B_1 + 4\mu_1} \tag{6.5}$$

$$\mu = \mu_2 - f_1(\mu_2 - \mu_1)\frac{5(3B_2 + 4\mu_2)}{9B_2 + 8\mu_2 + 6(B_2 + 2\mu_2)\mu_1/\mu_2} \tag{6.6}$$

where we can neglect the elastic anisotropy of the tin nanocrystals (XRD shows that the tin crystals have random orientation with respect to the substrate, see below). 1 is for tin and 2 for silica; f_1 is the tin volume fraction in the film. Fig. 6.3 shows μ as a function of μ_1 for $f_1 = 0.2$ (as in our films).

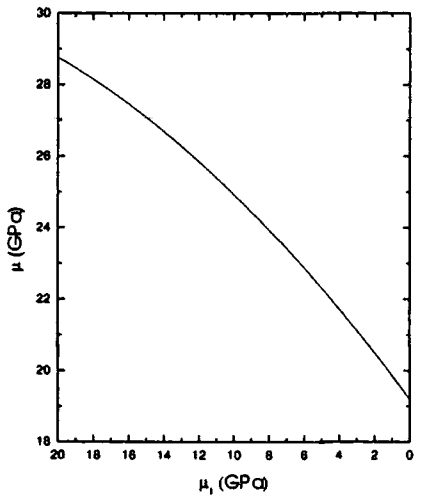

Fig. 6.3: Effective shear modulus μ of silica film containing a concentration f_1=0.2 of inclusions of shear modulus μ_1 vs μ_1. For solid Sn nanocrystals μ_1=0. For silica μ_2=31.2 GPa and B_2=36.9 GPa.

In order to obtain maximum sensitivity to nanoparticle properties, the sample geometry was designed to have only one Brillouin active surface phonon (modified Rayleigh phonon) travelling parallel to the surface and probing mainly the silica film containing the nanocrystals. In this way the modified Rayleigh phonon is localised in the film and has only a vanishing tail in the silicon substrate. This result was achieved by computing the layer projected phonon density of states and the corresponding Brillouin cross section using the software described in section 3.2.2 [26, 27]. The results are shown in fig. 6.4 and fig. 6.5 respectively.

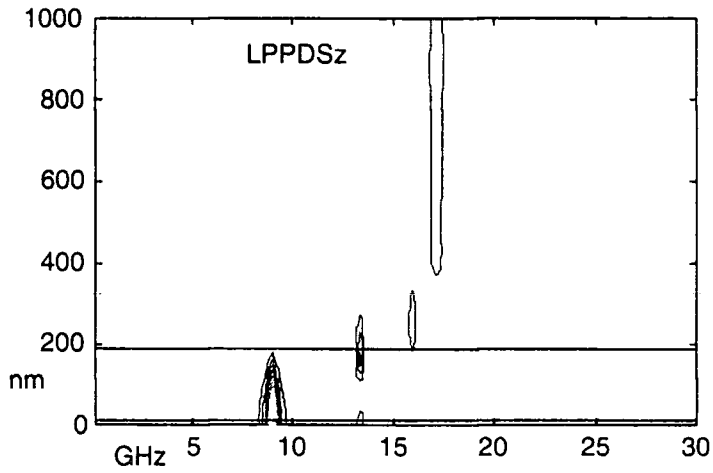

Fig. 6.4: Contour lines of the computed Layer Projected Phonon Density of States (LPPDS) as a function of the sample depth and frequency. The horizontal solid line at 186 nm represents the film-substrate interface.

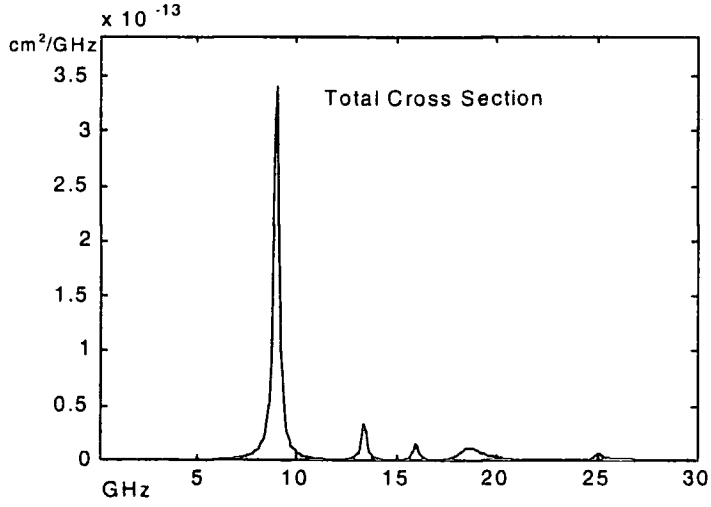

Fig. 6.5: Computed total Brillouin cross-section for our samples, showing the expected Rayleigh peak at a frequency of about 9 GHz.

In the case of very small sizes, when the particles melt, their shear modulus drops abruptly from a finite value to a much lower value (liquid phase). The contribution of the variation of the Sn nanoparticle density to the effective medium density across melting is negligible. The effect of varying B_1 is negligible too (the inverse of the nanoparticle bulk modulus jumps to the value of the higher finite compressibility of the liquid), and so the main effect of the melting is an abrupt lowering of μ of the order of 35% for our samples. In correspondence with this, computing again the Brillouin cross section, a redshift of the Rayleigh peak of the order of 1.5 GHz is found immediately beyond the melting temperature. Melting of bigger particles is indeed a two-step process, a surface melting followed by a complete melting. In real samples a size distribution exists leading to coexistence of solid, partially liquid and completely liquid particles at a given temperature. This corresponds to a progressive phase change in a rather wide temperature interval before the overall rather abrupt softening occurs. In summary, the softening of the shear modulus after melting is responsible for the decrease of the surface wave velocity (and so for the Rayleigh peak redshift).

Experimentally a shift of 0.6-0.9 GHz was detected for all the samples. The agreement roughly within a factor of two with the experimental results represents a good test for the interpretation reported above, considering also that:

a) the model computation was made using literature values of both tin and silica elastic parameters and the nominal film geometry was used;
b) effective-medium formulae do not describe particle scattering and do not include explicitly particle size but only the Sn concentration;
c) x-ray diffraction (see below) indicates that melting is occurring in the same temperature range as determined by Brillouin scattering.

A better quantitative interpretation would require going beyond the effective medium approximation to take explicitly into account particle size effects and not only the Sn concentration.

Indeed, this interpretation can be considerably refined considering that a liquid manifests a non-zero shear modulus when responding to a high frequency excitation [28, 29]. This frequency-dependent effective shear modulus can be related to the viscosity η of the liquid and to a characteristic relaxation time τ. In other words, while a spontaneous non-equilibrium shear stress fluctuation decays in the liquid with the relaxation time τ, the liquid can support shear acoustic waves propagation at

frequencies higher than $1/\tau$. In general the phenomenon can be described by a frequency-dependent complex shear modulus [28].

A non-zero value of the frequency dependent shear modulus would mean a lower value for the decrease of the effective medium shear modulus across melting, and so a lower redshift for the Rayleigh peak. As size effects on both viscosity and relaxation times are unknown for metal nanoparticles we do not attempt to describe this effect quantitatively.

The central feature, which is not present at room temperature, becomes more and more intense approaching the melting temperature, and after the shift of the Rayleigh peak the intensity seems to lower again (the central peak is wider than 30 GHz and so our data are not precise enough to study this behaviour in detail for all the samples or to investigate the width of the peak). We show the behaviour of the central peak area as a function of temperature for sample *Sn3* in fig. 6.6.

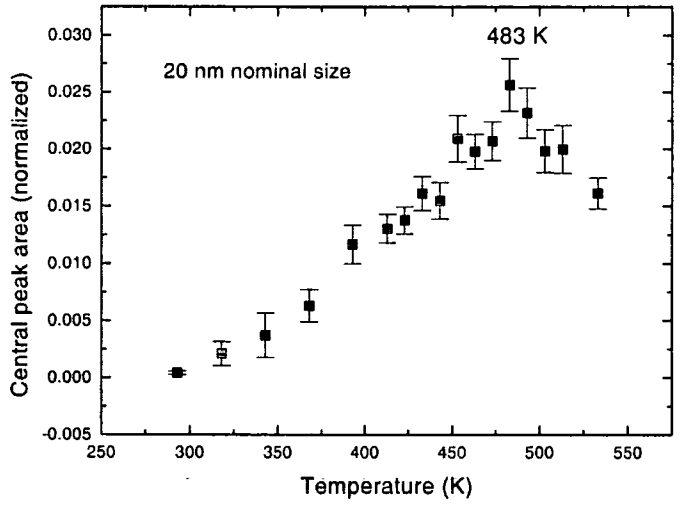

Fig. 6.6: Central peak area as a function of temperature in sample *Sn3*.

In the vicinity of a first-order phase transition one may analyse this central feature in terms of a direct contribution of entropy fluctuations to the dielectric function fluctuations responsible for Brillouin scattering [23]. These fluctuations are expected to reach a maximum at the melting temperature. Otherwise its origin could possibly be related to the coupling of soft modes in the single particles with relaxing degrees of freedom through a damping process [30], arising from dynamic inhomogeneities in the semi-liquid particles in the vicinity of the phase transition. As the Rayleigh phonon is a mesoscopic excitation of the whole effective medium, it cannot be assumed as the soft

mode characterising the single particle melting. Indeed the soft mode could be identified with the acoustic modes confined in the particles and studied by low-frequency Raman scattering as explained in section 6.5.

6.4 X-ray diffraction

X-ray diffraction was used to determine the crystallinity of the tin nanoparticles at room temperature and to study their structure as a function of temperature. In particular the nanoparticle melting temperature was measured as a function of their size (see also [19, 20]). High intensity, highly collimated beams of X-rays from synchrotron radiation sources were necessary for the detection of the very weak diffracted intensities scattered by the small tin nanoparticles in the amorphous matrix thin film.

Fig. 6.7: CCD camera image of the diffraction rings in sample *Sn3*. The strong diffraction rings not labelled are from the sample holder.

Preliminary data [23] were collected on the high-resolution powder diffractometer on Station 2.3 (Soller slit collimation of the detector) at the Synchrotron Radiation Source (SRS) at Daresbury (UK), with an x-ray wavelength of 1.3 Å. For the acquisition of most of the XRD profiles the two circle diffraction instrument at station BM16 at the European Synchrotron Radiation Facility (ESRF) at Grenoble (France) was employed, which consists, as described in chapter 3, of two high-precision, heavy-duty rotary tables aligned coaxially on a base plate; and a channel array of 111 oriented Ge crystals (single crystal analysers) each in front of a scintillation detector. Each channel is separated by 2^{o} [31].

The wavelength chosen was 0.55197 Å, and detector only scans were acquired, keeping the incident angle fixed at about 5^{o}. The reason for using a small incidence

angle is that this arrangement increases the x-ray path in the thin film, thus enhancing the interaction of the beam with the tin particles. The minimum value was limited by the geometry of the furnace.

In addition to the data collected by the scintillation detector, CCD camera diffraction images of the films were acquired and showed continuous Sn diffraction rings (fig. 6.7), indicating that the nanoparticles are randomly oriented in the matrix, without any preferential orientation with respect to the Si substrate. A diffraction CCD image of the reference sample (matrix only) revealed no rings, demonstrating that the SiO_x matrix was indeed amorphous.

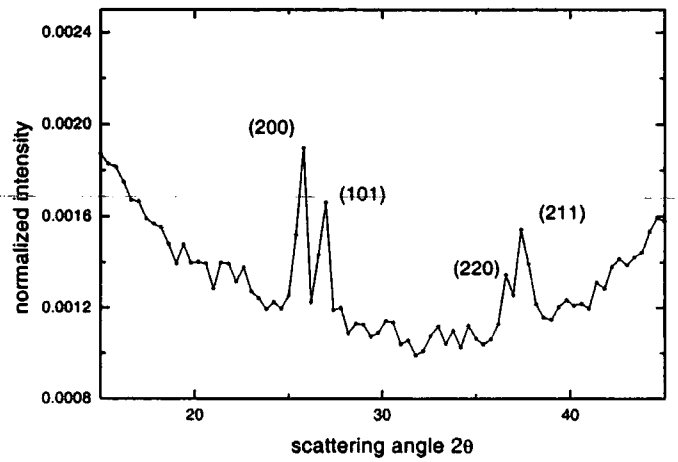

Fig. 6.8: Diffraction pattern from sample *Sn3*. In this measurement λ=1.3 Å.

Fig. 6.8 shows a section of the diffraction pattern at room temperature for the sample *Sn3*. The four peaks detected (superimposed onto a varying background) index precisely to the 200, 101, 220, 211 diffraction peaks of the tetragonal structure of β-tin, which is the stable tin phase at room temperature (white tin). The first two peaks were individually resolved for samples *Sn3* and *Sn2*, while only a broad band due to the superposition of two very broad and low intensity peaks could be detected for sample *Sn1*. We can thus affirm that at room temperature the nanoparticles are crystalline.

The peaks can be fitted well to Gaussian functions as well as to Pseudo-Voigt functions (combination of a Gaussian with a Lorentzian); a fit to Lorentzian functions is good, but not excellent in the case of sample *Sn2*. This could indicate the presence of a small amount of strain in this sample. Using Scherrer's equation one can obtain an estimate of the average diameter *L* of the diffracting nanocrystals:

$$L = \frac{0.94\lambda}{\Delta(2\theta)\cos\theta} \tag{6.7}$$

where λ is the x-ray wavelength, 2θ is the scattering angle and $\Delta(2\theta)$ is the FWHM (Full Width at Half Maximum) of the peak.

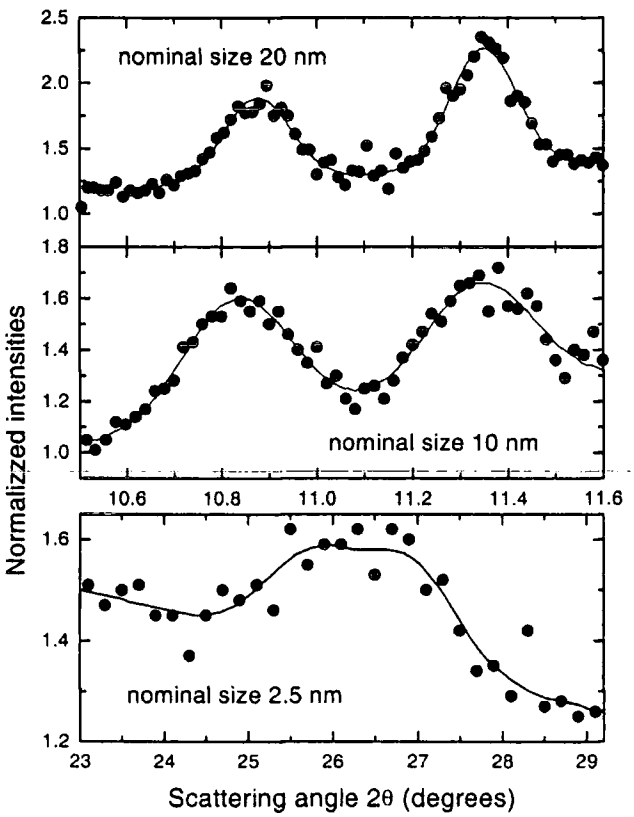

Fig. 6.9: (200) and (101) Bragg peaks of tin nanoparticles in sample *Sn3* (top graph), *Sn2* (middle) and *Sn1* (bottom). Points represent experimental data, lines are Pseudo-Voigt fits to the two peaks. For *Sn3* and *Sn2* λ = 0.55197 Å; for *Sn1* λ = 1.3 Å.

In fig. 6.9 Pseudo-Voigt fits for the 200 and 101 peaks in the three samples are shown (in sample *Sn2* the weight of the Gaussian component is predominant with respect to that of the Lorentzian component). The FWHM value obtained from the fit is the same for any of the three fitting functions. The calculated average diameters are 4.5±2 nm (*Sn1*, nominal size 2.5 nm), 11±1 nm (*Sn2*, nominal size 10 nm) and 18±1 nm (*Sn3*, nominal size 20 nm). The agreement with the nominal values is good.

6.4.1 Temperature Calibration

A furnace for high-temperature powder diffraction measurements at temperatures up to 1600 °C was employed for measurements of the diffraction profiles as a function of temperature. However, there is a serious difficulty in producing an absolute calibration of the sample temperature due to the inability of locating a thermocouple directly on the (rotating) sample. As it was not possible to determine the melting point directly from the furnace thermocouple, an internal calibration had to be performed in order to determine the temperature directly from the measurement of the lattice parameter of the single crystal silicon substrate on which the silica glass was deposited. However, the method is more widely applicable to high resolution powder diffraction, as silicon single crystal substrates are regularly used for their low background signal.

The calibration of the furnace was also needed to compare XRD data with the Brillouin data. Due to the very high resolution of the Ge (111) analyser we were able to detect the shift of a Si reflection from the substrate. This reflection indexes to the "forbidden" (002) peak of the Si structure, but could also originate from the 2nd harmonic of the strong allowed (004) reflection. In fact, harmonic suppression is not complete in the monochromatization of the main synchrotron beam, and a weak $\lambda/2$ component is indeed incident onto the sample.

In the powder diffraction patterns of the Sn nanoparticles films taken at station BM16 at the ESRF the fixed incident beam angle was about 5° and the sample was usually kept spinning at a rotation rate of 1 Hz. In fig. 6.10 reflections marked H arise from the sample holder, while the reflections from the Sn particles are indexed. The reflection from the silicon single crystal substrate is indicated. Its position is in excellent agreement with that calculated from the wavelength determined from a silicon powder standard and is clearly a single crystal reflection. It is not present when the incident beam angle is offset by (more than) 2°. As the Ge (111) analyser, once calibrated, provides an absolute angular measure, we were able to check the assignment by moving the detector to the angular position for the 004 (allowed) Si reflection and displacing the sample. The 004 reflection was found in the position expected and saturated the detector. When the sample rotation was stopped, we were able to locate the 004 reflection in reciprocal space by successive displacement of the specimen and detector. The peak maximum occurred at a detector angle of 23.456°, corresponding to a lattice parameter of 5.431 Å at 30°C, but with the specimen angle of 13.31°. This shows that the [001] direction is not coincident with the sample rotation axis.

It proved impossible to locate the position of the 002 reflection in reciprocal space in a similar manner as the precision of the diffractometer was insufficient to locate such an extremely narrow reflection with a stationary sample. However, due to the small angular offset of the [001] direction and the rotation axis, with the sample spinning, the 002 reflection flashes into the reflection condition twice per revolution. The narrow 002 Bragg peak (fig. 6.10) is limited by the Ge 111 analyser width, which at a wavelength of 0.55197 Å is 6 arcseconds.

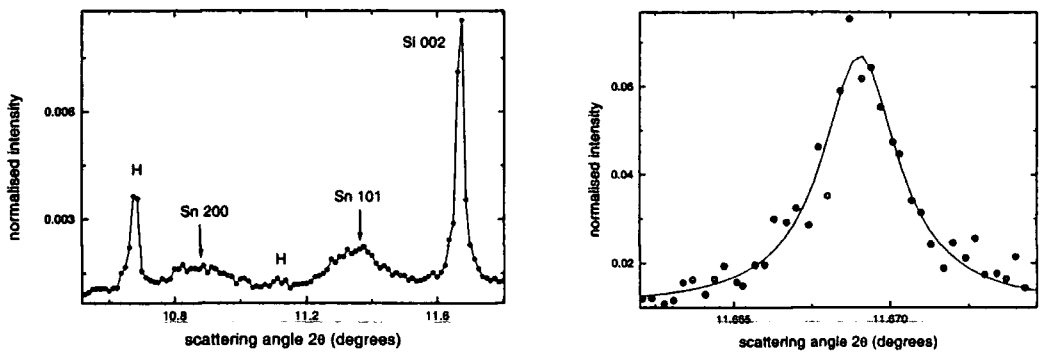

Fig. 6.10: Diffraction pattern for sample *Sn3* showing the "forbidden" Si(002) reflection (left). Distorted 002 silicon peak due to the sampling error arising from the count time and revolution period of the sample. The line is a Lorentzian fit to the curve (right).

As a result of its use as a standard, the thermal expansion coefficient of silicon is known very precisely. It is, however, small and to exploit this parameter as a thermometer we must have a high angular resolution diffractometer. For a temperature change of 10 °C, at wavelength 1 Å the change in the 004 reflection Bragg angle is only 2 arcseconds. The scattering angle therefore changes by 0.4 arcseconds per degree. For slit-collimated diffractometers, even in the parallel beam geometry, this constraint makes the technique impossible. This is even the case for the Soller-slit collimation at the powder diffraction station 2.3 at the Daresbury SRS, where the resolution is 0.07° [31]. The use of a crystal analyser is thus necessary for the method to work and it is therefore applicable only to high resolution powder diffraction using synchrotron radiation [32-36]. With a crystal analyser calibrated against a silicon powder standard, the angular position of the detector provides sufficient precision to monitor the change in lattice parameter of the silicon single crystal. For a symmetrically cut 111 Ge crystal analyser, the FWHM of the Bragg reflection is 11 arcseconds at 1 Å and when the peak centroid is determined by curve fitting, a precision approaching 1 °C can be anticipated.

The sample spinning does, however, present one significant problem when scanning the Bragg peak due to aliasing between the counting time and the period of rotation. In some sampling periods n rotations occur, while in others it may be n - *1*. If n is small, the peak shape can be very irregular (fig. 6.10) and care must be taken in determining the centroid of the peak. Despite this, it proved straightforward to fit the peak to pseudo-Voigt, or even simple Lorentzian, functions to determine the peak position. Repeated measurements at a single temperature indicated that the precision to which the peak centroid could be measured was 0.0003 degrees. From this peak position, it is straightforward to deduce the lattice parameter of the silicon. Relative to the lattice parameter at room temperature, the true temperature of the silicon can be deduced by assuming only the well-documented thermal expansion coefficient of silicon.

The linear thermal expansion coefficient is defined as $\alpha(T)=1/l_0(dl/dT)$, where l_0 is the lattice spacing at the reference temperature T_0. In cubic crystal $\alpha(T)$ is a scalar, independent of crystal direction. From $\alpha(T)$ the lattice parameter at the temperature T can be determined as

$$l(T) = l_0(\int_{T_0}^{T} \alpha(T)dT + 1) \qquad (6.8)$$

Data about the temperature dependence of α(T) can be found in the literature [37-40], and an analytical expression accounts very well for these data between 300 K and 1500 K [39]:

$$\alpha(T) = [3.725 \cdot (1 - e^{-5.88 \cdot 10^{-3}(T-124)}) + 5.548 \cdot 10^{-4} T] \cdot 10^{-6} \quad K^{-1} \qquad (6.9)$$

A parabolic fit of these data between 300 K and 600 K (which is our range of interest) provides good accuracy, and from integration of the last equation an expression for the lattice spacing at a given temperature between 300 K and 600 K can be easily obtained, provided one knows the lattice spacing value at room temperature, which is 5.431 Å. This expression fits very well the available data of the Si lattice spacing as a function of temperature [37, 39].

Unfortunately the Bragg angle of reflection of a given set of crystal planes θ is shifted if there is an "out of plane tilt" [41], that is if the normal to the plane of reflection is not in the scattering plane but is misoriented by a small angle φ. In this case, there is an apparent Bragg angle θ' where $\sin\theta = \cos\varphi \sin\theta'$. A simple approximation shows the error $\Delta\theta$ in θ to be

$$\Delta\theta = \frac{\varphi^2}{2}\tan\theta \quad \text{[radians]} \tag{6.10}$$

The $\tan\theta$ dependence can be considered a constant over the θ range of our experiment, and so the tilt error only shifts the lattice parameter curve by a given amount. In the case of sample *Sn3* we measured the 002 Bragg angle to be $\theta'=(11.6685/2)^0$ at room temperature, while the actual value should be given by $2\theta = 2\sin^{-1}(\lambda/5.431) = 11.6665^0$. This means that $\varphi \cong 1.1^0$, so that $\Delta(2\theta) = 0.002^0$.

Fig. 6.11a shows the measured lattice parameter of the silicon as a function of the temperature measured by the furnace thermocouple, located close to the heater but not in contact with the sample. The solid line is the lattice parameter $l(T)$ predicted at temperature T from the published thermal expansion coefficient α. Noteworthy is the very substantial difference in the measured and predicted lattice parameter on heating. Replacement of the sample and change of sample holder resulted in a heating curve of different slope.

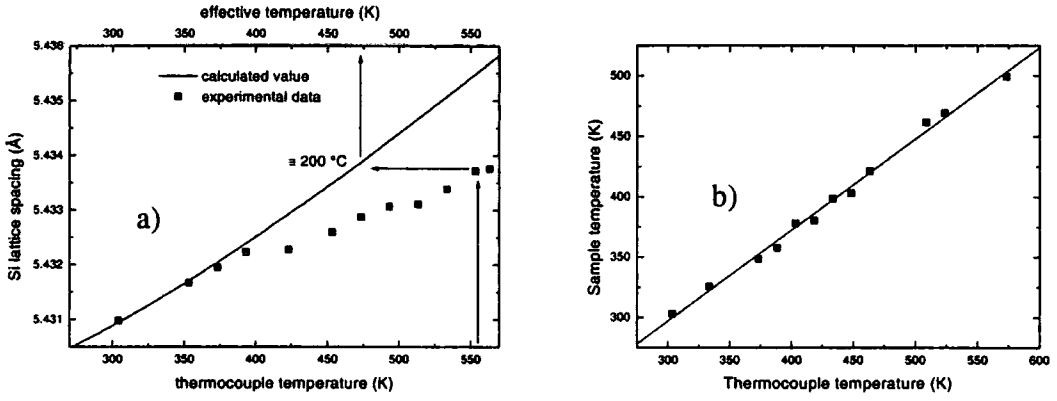

Fig. 6.11: a) points: measured silicon lattice parameter as a function of furnace thermocouple reading for the calibration of temperature; solid line: lattice parameter predicted from the published thermal expansion coefficient and measured lattice parameter at 30°C; b) calibration curve.

The calibration curve for the real sample temperature against temperature measured from the furnace thermocouple, resulting from the above described method, is shown in fig. 6.11b. The same calibration method has also been applied to a Si powder to test its reliability and the results show a remarkable agreement.

6.4.2 XRD as a function of temperature

In fig. 6.12 the diffraction peaks are shown as a function of temperature for sample *Sn3*, and for sample *Sn2*. Three features could immediately be noted: the peaks positions change systematically with temperature, this shift is higher for the 101 peak and the peak intensity falls sharply to zero in a small temperature range (≅ 20 K).

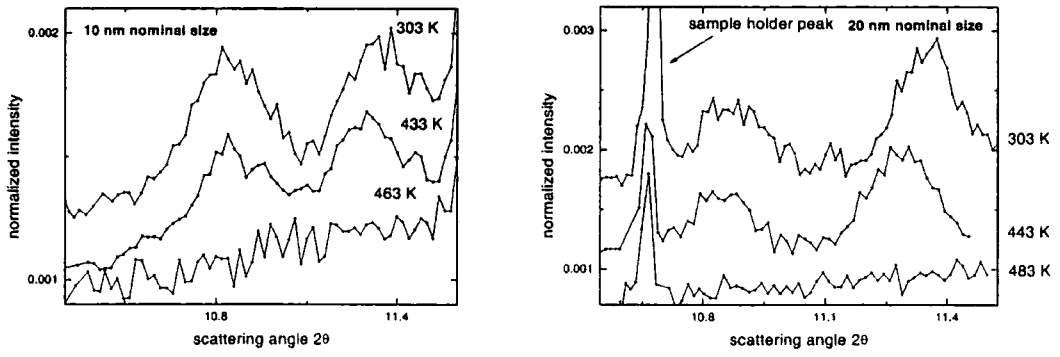

Fig. 6.12: (200) and (101) tin peak evolution as a function of temperature in sample *Sn2*(left) and *Sn3* (right).

The disappearance of the diffraction peaks indicates the loss of the crystalline order, and this can be identified with the melting of the particles. Within the precision of the temperature step size, it occurs at the same temperature as the abrupt redshift in the Brillouin spectra. In Table 6.1 the melting temperature detected for the three samples with Brillouin scattering experiments and with XRD measurements are reported. The agreement is good, particularly when considering that the temperature calibration was a major problem for the XRD measurements. The precision with which the melting temperature can be determined is thus limited.

Table 6.1:

Sample	Brillouin Rayleigh peak shift (K)	XRD melting temperature (K)
Sn1	393-423	393-423
Sn2	453-473	443-463
Sn3	473-493	463-483

Fig. 6.13 shows the melting temperature as a function of the particle size determined from the x-ray diffraction data. In all cases, the values are lower than the melting temperature of bulk tin, which is 505 K (232 ° C). The solid lines are fits to Eqs. (6.1) and (6.2), from which we determine the interfacial free energy between solid

and liquid γ_{sl} to be about 0.1 Nm^{-1}. Even though Eq. (6.1) is strictly applicable only to spheres of radius greater than 15 nm [7, 8] we believe that the γ_{sl} value we have evaluated is significant to an order of magnitude in our size range.

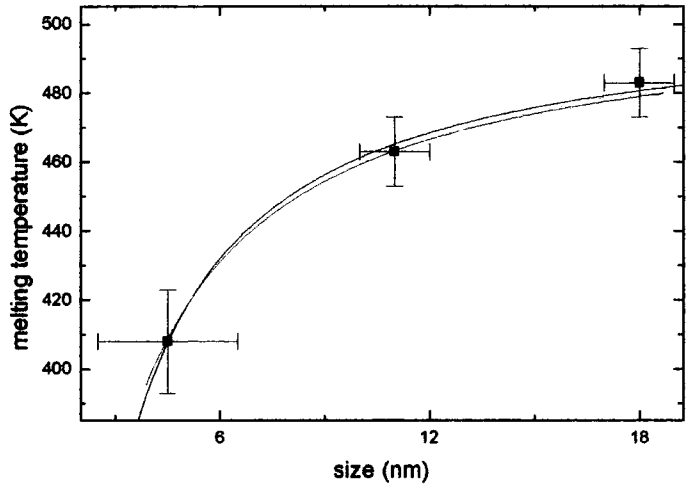

Fig. 6.13: Fit of equation $T_M=T_{bulk}-k/R$ (black line) and of equation $T_M=T_0\exp(-h/R)$ (red line) to experimental data.

After melting, cooling of the samples down to room temperature did not result in immediate recovery of the crystalline structure of the particles. After one or two hours the crystallinity was recovered perfectly.

In the case of the big nanoparticles (sample *Sn3*) the peaks were sufficiently sharp and intense to allow a precise determination of their position and as a consequence a precise measure of the β-tin lattice parameters in the particle. This could be done as a function of temperature, thus allowing for a calculation of the β-tin temperature expansion coefficients in the 20 nm nanoparticles. As we are observing the position of the 200 and 101 diffraction peaks, one can easily see that the tetragonal parameters *a* and *c* can be computed by means of the formula:

$$\frac{1}{d}=\sqrt{\frac{h^2+k^2}{a^2}+\frac{l^2}{c^2}} \qquad (6.11)$$

where *d* is the spacing corresponding to the (*hkl*) diffraction peak ($\lambda=2d\sin\theta$). Knowing the position of the two peaks (200) and (101), *a* and *c* can be obtained.

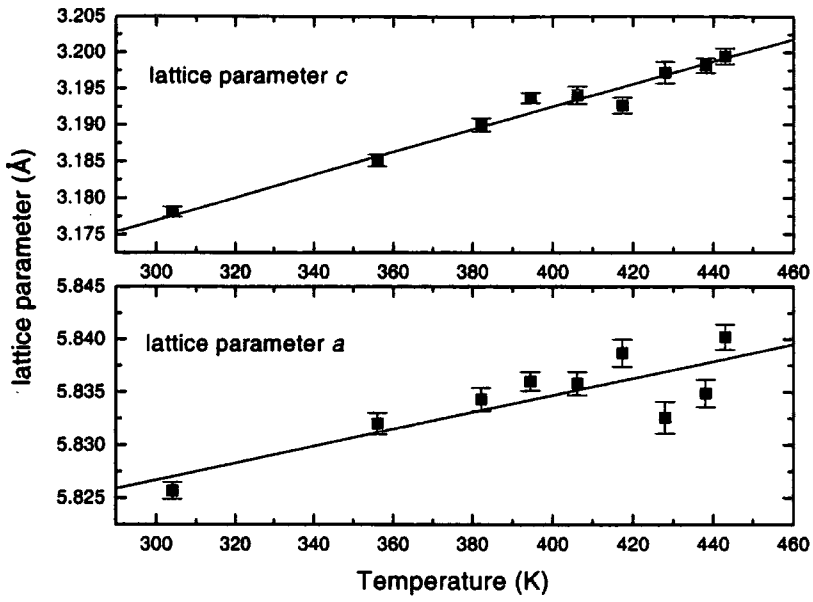

Fig. 6.14: Tin lattice parameters *a* and *c* as a function of temperature for sample *Sn3*. Solid lines are linear fits to the data for the calculation of the thermal expansion coefficients.

In fig. 6.14 the *a* and *c* values, determined from the (200) and (101) reflections, are plotted in the temperature range 303-443 K. The room temperature values for bulk tin are a=5.83 Å and c=3.18 Å respectively.

The lattice thermal expansion coefficient is defined as

$$\alpha(T) = \frac{1}{l_0}\frac{\Delta l}{\Delta T} \qquad (6.12)$$

where l_0 is the lattice parameter at the reference temperature and Δl its variation over the small interval ΔT. The expansion is anisotropic in the case of tetragonal crystals and the expansion coefficients of bulk tin single crystals are reported to be α_c between $30\cdot10^{-16}$ K^{-1} and $40\cdot10^{-16}$ K^{-1} and α_a between $15\cdot10^{-16}$ K^{-1} and $20\cdot10^{-16}$ K^{-1}, in the range 300-500 K [42]. We obtain, from fig. 6.14, $\alpha_c = (50\pm10)\cdot10^{-16}$ K^{-1} and $\alpha_a = (20\pm5)\cdot10^{-16}$ K^{-1}. At least for the largest particles there is no evidence of a different expansion behaviour with respect to the bulk. This can be interpreted as an absence of a high stress condition for the nanoparticles. There are two other considerations in support to this conclusion. First of all, the values of the lattice parameters at room temperature for both samples *Sn3* and *Sn2*, where they can be calculated with sufficient accuracy, are, within experimental errors, equal to the *a* and *c* bulk values. This indicates that there are no major distortions with respect to the bulk lattice. Further, we can perform a Hall

analysis of strains (see for example [43-46]) where finite size and strain both contribute to the peak width

$$\frac{\beta\cos\theta}{\lambda}=\frac{1}{L}+\eta\frac{\sin\theta}{\lambda} \tag{6.13}$$

(if the size and distortion line profiles are presumed to be Lorentzian), or

$$\left(\frac{\beta\cos\theta}{\lambda}\right)^2=\left(\frac{1}{L}\right)^2+\left(\eta\frac{\sin\theta}{\lambda}\right)^2 \tag{6.14}$$

(if the profiles are presumed to be Gaussian), where η is the strain, L the particle size and β the peak FWHM. Knowing with good precision the θ position and the FWHM of the first 4 diffraction peaks in sample *Sn3*, we can determine the contribution of strain to the width of the peaks. We find that the strain is very small ($\eta < 1\%$), well below the detection limits allowed by our data.

In conclusion, the possibility of detecting the melting of tin nanoparticles of different diameters with Brillouin inelastic light scattering, from the redshift of the surface Rayleigh wave travelling in the film, has been shown. This result has been validated and confirmed by XRD. Together with a series of basic characterizations (particle size, particle random orientation in the matrix, absence of significant stress) we have shown that the melting temperature, according to theory and previous experiments on other materials, decreases with decreasing size.

6.5 Raman scattering and low-frequency Raman scattering

In recent years several works have been published reporting low-frequency Raman measurements of acoustic vibrations confined in nanoparticles, usually embedded in an amorphous matrix [47-59]. In most of these works the nanoparticles are modelled as elastic bodies of approximately spherical shape. The theory [55, 60-62] shows that spheres can vibrate with two different types of eigenmodes, spheroidal and torsional, according to the classical theory of Lamb [60]. Theoretical calculations [63] have shown that selection rules exist which allow only some of these modes to be Raman active. The characteristic frequencies associated with these modes are usually only a few tens cm^{-1}, and this is the reason why the corresponding effects are usually measured in the low-frequency region of the Raman spectra. Within the continuum approximation, the frequency of both modes is proportional to the sound velocity in the

material and to the inverse nanocrystal diameter, and low-frequency Raman scattering is often used to estimate the average particle size.

At the mesoscopic scale, instead, long-wavelength surface acoustic phonons in the system composed by the thin film, in which the nanoparticles are buried, together with the substrate, manifest the nanoparticle presence as a perturbation in their dispersion relations. As long as the wavelength of the phonons is much bigger than the particle size, the effect can be treated within an effective medium approach, mainly as a modification of the shear modulus of the film, as shown in the previous sections. This type of modified surface phonon has been detected by means of Brillouin scattering; while low-frequency Raman scattering by the acoustic modes of individual nanoparticles is incoherent, Brillouin scattering from long wavelength surface acoustic phonons is coherent.

In this section the measurement of low-frequency Raman scattering from the localized acoustic vibrations in β-Sn nanoparticles as a function of temperature, across melting, is reported for the first time; in this way we utilise a direct and local coupling between vibrational dynamics, structural changes and dynamic light scattering. In particular, the evolution of these modes with increasing temperature, as the nanoparticles undergo the melting transition, is used here for the first time as a direct evidence of the particle melting. A measurement of the optical Raman modes in Sn particles as a function of particle size and temperature is also reported.

Raman measurements were performed in the range 30-200 cm^{-1}. The excitation was from the 532 nm line of the Nd:YAG laser. The samples were placed in the Oxford Instruments thermocryostat in which a 10^{-4} torr vacuum was induced in order to avoid scattering from the air, which produces a series of lines in the region of interest, due to the roto-vibrational spectrum of the molecules present in the atmosphere. In fig. 6.15 a spectrum with the sample *Sn3* in the thermocryostat is compared with a spectrum of the sample kept in air. The power incident on the sample was limited to 10 mW.

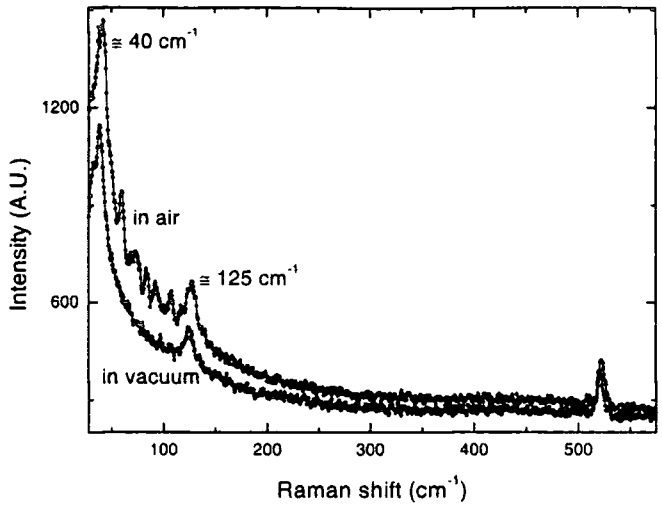

Fig. 6.15: Raman spectra from sample *Sn3* kept in air (top line) and in vacuum (bottom line), showing the optical phonons from β-tin.

For the low-frequency measurements the Sandercock multipass tandem Fabry-Perot interferometer, usually employed for Brillouin scattering experiments, was used. The mirror distance of the Sandercock interferometer was set to 0.5 mm, thus allowing a free spectral range (FSR) of about 300 GHz, which roughly correspond to 10 cm^{-1} (1 cm^{-1} ≡ 30 GHz). For the temperature control the samples were placed inside the thermocryostat. The spectra were measured at different temperatures in the range 293-533 K, usually with a step size of 15 K or 20 K. The excitation wavelength was the 514.5 nm line from the Ar ion laser; a power of 40 mW was incident onto the sample surface. Data were recorded in a backscattering geometry with the beam at a fixed incidence angle (θ = 50°) with respect to the surface normal direction, for all the samples and all the different temperatures.

6.5.1 Experimental results

In fig. 6.16 the room temperature optical Raman spectra for samples *Sn1* and *Sn3* and for sample *Snref* are reported. The high intensity elastic tail at low frequencies in the metal-containing samples is due to their high reflectivity. Measurements in a backscattering geometry but with a 50° incidence angle of the beam with respect to the direction normal to the sample surface helped to lower the elastic peak.

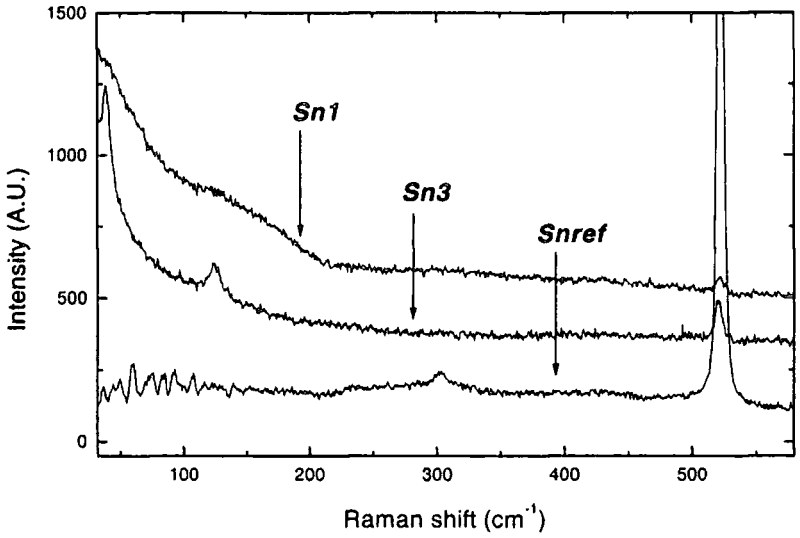

Fig. 6.16: Raman spectra from samples *Sn1*, *Sn3* and *Snref* (from top to bottom).

The lines at 40 cm^{-1} and 125 cm^{-1} in the *Sn3* sample are the visible optical Raman modes from tin [64-67]. In sample *Sn1* only a very broad feature is visible. This broadening is due to quantum confinement and therefore to the relaxation of the $\mathbf{q} \cong \mathbf{0}$ selection rule for Raman scattering in the nanoparticles (for the phonon dispersion in tetragonal β-Sn crystal see [68-70]). In the reference sample two peaks due to first ($\cong$ 521 cm^{-1}) and second ($\cong$ 300 cm^{-1}) order Raman scattering in the Si substrate are visible, which shows that the tin-free sample is transparent to the laser light.

As it will be shown in the next section, the eigenmodes of the tin particles are expected in a frequency region below 10 cm^{-1}. For this reason it was not possible to use a triple grating spectrometer as that employed for standard Raman scattering measurements, since the metallic particles strongly reflect elastically the laser light. The high contrast Sandercock interferometer, with higher resolution, was thus employed for these low-frequency measurements.

Fig. 6.17 shows the low-frequency spectra at room temperature for the three samples containing tin and for the reference sample. The spectrum is flat in the case of the reference sample, except for the peak at about 140 GHz, which is the bulk longitudinal peak from the silicon substrate. This again shows the amorphous matrix to be transparent to the laser light.

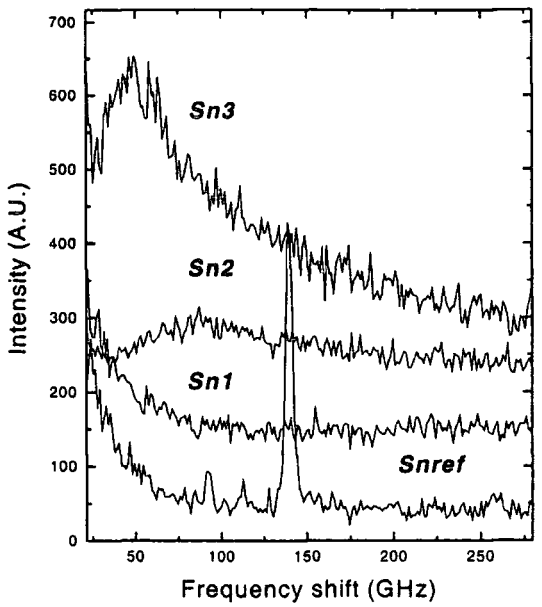

Fig. 6.17: Low frequency vibrational spectra from samples *Sn3*, *Sn2*, *Sn1*, *Snref* (from top to bottom, intensities shifted for clarity).

For samples *Sn3* and *Sn2* a broad peak is detected, whose maximum is at about 50 GHz and 85 GHz respectively, with a long tail at higher frequencies. In sample *Sn1* this feature was not detected, but a central peak is present.

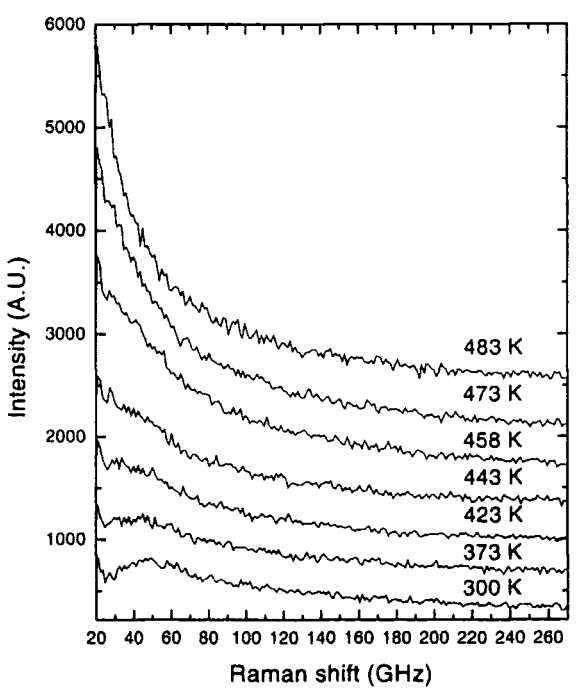

Fig. 6.18: Evolution of the low-frequency vibrational spectra with temperature in sample *Sn3* (intensities shifted for clarity).

Fig. 6.18 shows the evolution with temperature of the low-frequency spectrum for sample *Sn3*. The reference sample was also measured as a function of temperature, and no change was evidenced, as expected.

Finally the evolution of the optical Raman modes as a function of temperature was studied (fig. 6.19) for sample *Sn3*, showing broadening and weakening of the Raman peaks as the temperature increases and the local translational order is lost; no sudden change in correspondence of the melting temperature could be detected, probably because short-range order is still present at the transition.

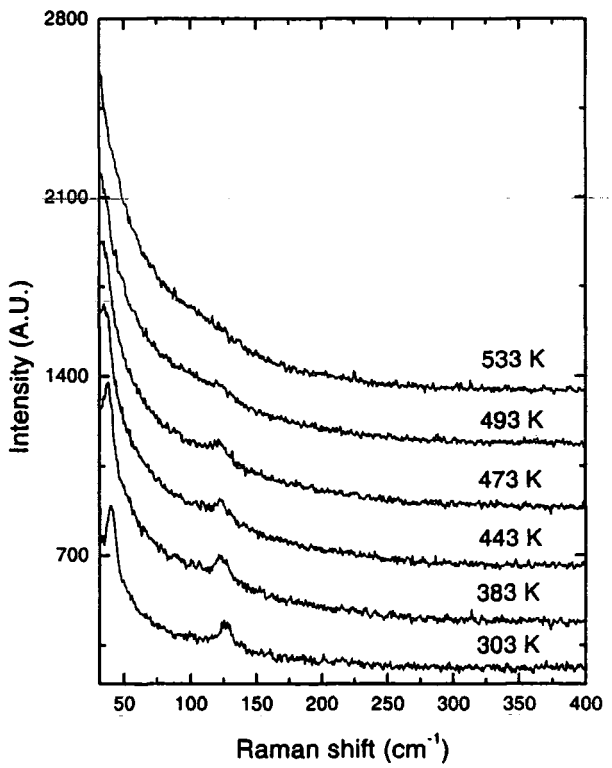

Fig. 6.19: Evolution of Raman-active optical phonons in sample *Sn3* as a function of temperature (intensities shifted for clarity).

6.5.2 Discussion

From the analysis of the free vibrations of a sphere two different families of modes are derived. The *spheroidal* modes are characterized by an angular momentum number l=0,1,2,..., and their nondimensional eigenvalues depend on the material through the ratio v_l/v_t, where v_l and v_t are the longitudinal and transverse sound

velocities, respectively. Conversely, the *torsional* modes, characterized by an angular momentum number l=1,2,3,... represent a vibration without dilatation and their non-dimensional eigenvalues do not depend on the material. The allowed frequencies are labeled by n and l (harmonic or *solution* number, and angular momentum number, respectively; n=0 are the modes confined at the surface).

When the particles are embedded in a matrix, different boundary conditions have to be taken into account (i.e. rigid or semi-rigid walls). This usually shifts the allowed modes to higher frequencies with respect to the free-sphere case.

The peak frequencies are proportional to the sound velocities and to the inverse nanocrystal diameters, $1/d$. Generally one can always write:

$$\nu = S_{l,n} \frac{v_t}{dc} \quad [\text{cm}^{-1}] \tag{6.15}$$

where d is the diameter expressed in cm and v_t is the transverse sound velocity; c (velocity of light) is introduced to express the frequency in cm^{-1}, as it is usual in literature. $S_{l,n}$ is a proportionality coefficient related to the eigenvalues of the allowed modes, and it depends on the angular momentum number l, the harmonic number n, the chemical composition and shape of the particle, the matrix, the boundary conditions. From selection rules [63] only l=0 and l=2 spheroidal modes are Raman-active at the first order. The l=0 mode leads to completely polarized scattering (at least for an ideal sphere), while the l=2 mode leads to depolarized scattering. A polarization analysis of the scattered light (parallel or perpendicular to the excitation light) was attempted, by introducing a dichroic polarizer before entering the interferometer, but the resulting signals were too low to give any useful information.

Solving the eigenvalue vibrational equation for tin spheres, one obtains that the lowest frequency modes are the l=2, n=0 spheroidal ($S_{2,0}{}^{S}$ = 0.84) and the l=2, n=0 torsional ($S_{2,0}{}^{T}$ = 0.85). The sound velocities in bulk tin are $v_t \cong$ 1500-1800 m/s, and $v_l \cong$ 3200-3500 m/s [25].

In our measurements, after subtracting a lorentzian wavefunction to account for the elastic central peak, the peaks were fitted with a damped oscillator wavefunction (see fig. 6.20):

$$I(\nu) = \frac{I_0}{\left[1-\left(\frac{\nu}{\nu_0}\right)^2\right]^2 + \left[2\zeta\frac{\nu}{\nu_0}\right]^2} \tag{6.16}$$

where ζ is the damping factor.

Thus we obtained ν_0 =2 cm^{-1} (60 GHz), ζ = 0.2 and ν_0 = 3.15 cm^{-1} (95 GHz), ζ = 0.3 for the 18 nm (*Sn3*) and the 11 nm (*Sn2*) particles respectively. These frequencies correspond to a $S_{l,n}$ value of about 0.7, i.e. the frequency of the two peaks scales exactly as $1/d$ but are lower than the calculated values.

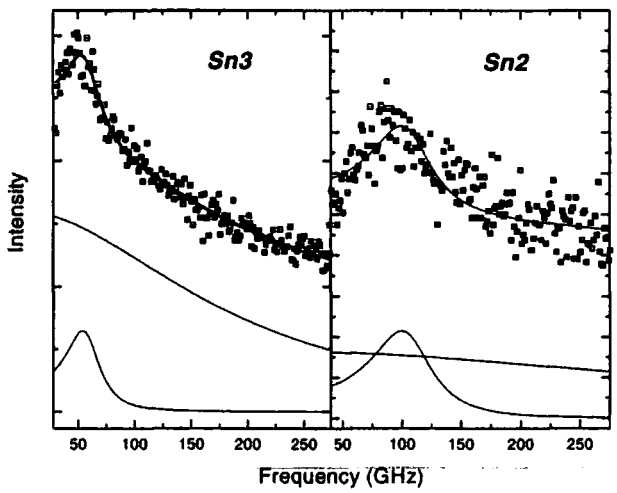

Fig. 6.20: Room temperature low-frequency spectrum for sample *Sn3* and *Sn2*. Points are experimental data; lines represent a fit with a damped oscillator wavefunction and a lorentzian central peak.

The difference between the experiment and the theory could be ascribed to a deviation from the spherical shape, as expected in our particles (see [58]), or, less likely, to non-bulk values of the elastic constants. Indeed, the difference could also be explained by the presence of the matrix. In fact, some studies have found that new modes, at lower frequencies, are allowed when considering the continuity of the solutions at the particle-matrix interface [71, 72].

Experimentally [49] it was found that, as the size decreases, the width of the peak gradually increases and its intensity rapidly decreases. This is usually attributed to damping, through an interaction with the matrix [73, 74]. Our measurements agree with these observations.

The asymmetric broadening of the peaks could arise from a mixing of different vibrational modes. Saviot *et al.* [55] attribute the tail at higher frequencies to overtone vibrational modes broadened by the size distribution. Ferrari *et al.* [53] suggest that the particle surface roughness is expected to allow higher frequency modes to appear and this could explain the important long tail of the experimental peak. Montagna and Dusi

[62] affirm that for deviations from the spherical shape, at higher l values the protrusions on the surface with a small radius of curvature become more and more important.

The absence of any peak in sample *Sn1* could be due to: a) its intensity is too low to be detected (and indeed the intensity is usually reported to be decreasing with the particle size); b) the shape of the (very small) particles is too irregular; c) the size distribution is very dispersed; d) the vibrational modes are overdamped.

Nisoli *et al.* [75] employed femtosecond pump-and-probe spectroscopy to study oscillations and damping in tin nanoparticles deposited with the same technique as for our samples. The observed oscillation frequencies are in agreement with our results, and also the damping was found to increase with particle size (see also [73]); the oscillations in the smallest particles (4 nm) were found to be overdamped.

In the room temperature measurement of sample *Sn3* a structured double peaked feature is present at the peak maximum. This could be due to the bimodal distribution of particles, which seems unlikely. A similar double feature was observed in reported measurements [55-57] and assigned to scattering from higher frequency modes. In our case other modes can be excluded because their frequencies would be too high (unless the $l=2$, $n=0$, $S_{2,0}{}^{T} = 0.85$ torsional mode is allowed maybe due to deviations from the spherical shape). One could think that in a non-perfect sphere the degeneracy of the $l=2$ spheroidal mode is removed, as explained by Mariotto *et al.* [76].

For the analysis of the measurements at different temperatures, we refer to the big particles (fig. 6.18), where the low-frequency peak is most intense. As the temperature increases, the strong central peak starts to increase. It is still possible to detect the vibrational peak superimposed onto the central peak as a shoulder. At 473 K the shoulder disappears, in agreement with the previously measured melting temperature of the nanoparticles. Fitting of the spectra, to a superposition of a lorentzian central peak and of Eq. (6.16), showed a gradual softening and broadening of the vibrational mode together with an increase of the elastically scattered intensity. After the melting temperature no vibrational mode could be detected.

The temperature dependence of the spectral density can be understood in the following way. In the case of the biggest particles melting should start at the surface. Just beyond surface melting temperature, the thin, viscous, liquid layer, coupled to the still solid vibrating sphere, damps the normal modes of the sphere (ζ increases) and shifts the peak maximum at lower frequencies.

As the melting process extends to the bulk, slower fluctuations in the phase composition (melting nuclei) manifest themselves both as a further softening of the coupled acoustic mode and as a strong central peak [30]. As the modes of the smaller particles are already overdamped in the solid state, in this case melting gives rise only to the central peak increase.

6.6 Conclusions

In this chapter it was demonstrated how a combined use of high-resolution synchrotron x-ray diffraction and Brillouin scattering was successfully employed to study different aspects of the melting phase transition in metal (Sn) nanoparticles of different sizes, embedded in an amorphous matrix thin film. Interesting and novel features in the light scattering mechanism were observed and investigated.

By performing surface Brillouin scattering measurements as a function of temperature, we detected an anomaly in the velocity of the Rayleigh wave travelling in the film, i.e. a softening of this velocity at high temperatures. The temperature at which the anomaly occurs was shown to be dependent on the particle size. XRD experiments confirmed that this temperature corresponds to the nanoparticle melting point and its trend as a function of the particle size is in agreement with theoretical predictions, although the transition is quite wide, due to the significant spread in the particle size distribution. A synchrotron-based furnace was used, and a careful calibration of the furnace temperature had to be performed. The anomaly in the wave velocity was explained by an effective medium model. XRD also provided information about the tin lattice structure (β-Sn), the low level of stress in the particles, their random orientation with respect to the substrate and their average size. Raman scattering showed confinement effects in the detection of the optical phonons, and low-frequency Raman scattering was used to detect acoustic modes confined in the particles and their behaviour across melting. A broad central peak, whose intensity increases with temperature, was detected in the inelastic light scattering measurements. A possible explanation lies in the coupling of the particle acoustic modes with some relaxing degree of freedom, through a damping process probably involving the matrix-particle interaction.

The combination of elastic x-ray and inelastic light scattering from thin films enables key structural parameters to be obtained and used in the modelling of the

Brillouin spectra, thus demonstrating the ability of the effective medium approach to interpret subtle effects in Brillouin spectroscopy.

References for Chapter 6:

[1] L. Banyai and S.W. Koch, "Semiconductor quantum dots", World Scientific, Singapore (1993)

[2] U. Woggon, "Optical properties of semiconductor quantum dots", Springer Verlag, Berlin (1997)

[3] A. Stella, P. Cheyssac and R. Kofman, in "Science and Technology of Thin Films", World Scientific, Singapore (1996), p. 57

[4] U. Kreibig, M. Vollmer, "Optical Properties of Metal Clusters", Springer, Berlin (1995)

[5] A.N. Goldstein, C.M. Echer, A.P. Alivisatos, Science **256**, 1425 (1992)

[6] N.T. Gladkikh, S.P. Chizhik, V.I. Larin, L.K. Grigor'eva, V.N. Sukhov, Izv. Acad. Nauk SSR Met. **5**, 196 (1982).

[7] V.K. Semenchenko, "Surface phenomena in metals and alloys", Pergamon Press, New York (1981)

[8] R. Kofman, P. Cheyssac, R. Garrigos, Y. Lereah, G. Deutscher, Z. Phys. D **20**, 267 (1991)

[9] F. Ercolessi, W. Andreoni, E. Tosatti, Phys. Rev. Lett. **66**, 911 (1991)

[10] R. Kofman, P. Cheyssac, A. Aouaj, Y. Lereah, G. Deutscher, T. Ben-David, J.M. Penisson, A. Bourret, Surf. Sci. **303**, 231 (1994)

[11] A. Stella, P. Cheyssac, R. Kofman, P.G. Merli, A. Migliori, MRS Proc. **400**, 161 (1996)

[12] P. Cheyssac, R. Kofman, R. Garrigos, Phys. Scrip. **38**, 164 (1988)

[13] A. Di Cicco, Phys. Rev. Lett. **81**, 2942 (1998)

[14] A. Stella, A. Migliori, P. Cheyssac, R. Kofman, Europhys. Lett. **26**, 265 (1994).

[15] S.B. Qadri, E.F. Skelton, D. Hsu, A.D. Dinsmore, J. Yang, H.F. Gray, B.R. Ratna, Phys. Rev. B **60**, 9191 (1999)

[16] P. Buffat and J.P. Borel, Phys. Rev. A **13**, 2287 (1976)

[17] S.L. Lai, J.Y. Guo, V. Petrova, G. Ramanath, L.H. Allen, Phys. Rev. Lett. **77**, 99 (1996)

[18] M. Schmidt, R. Kusche, B. von Issendorff, H. Haberland, Nature **393**, 238 (1998)

[19] K.F. Peters, Yip-Wah Chung, J.B. Cohen, Appl. Phys. Lett. **71**, 2391 (1997)

[20] K.F. Peters, J.B. Cohen, Y.-W. Chung, Phys. Rev. B **57**, 13430 (1998)

[21] E. Sondergard, R. Kofman, P. Cheyssac. A. Stella, Surf. Sci. **364**, 467 (1996).

[22] E. Sondergard, R. Kofman, P. Cheyssac, F. Celestini, T. Ben-David, Y. Lereah, Surf. Sci. **388**, L1115 (1997)

[23] C.E. Bottani, A. Li Bassi, B.K. Tanner, A. Stella, P. Tognini, P. Cheyssac, R. Kofman, Phys. Rev B **59**, R15601 (1999)

[24] W. Hayes and R. Loudon, "Scattering of Light by Crystals", Wiley, New York (1978)

[25] G. Grimvall, "Thermophysical Properties of Materials", North-Holland, Amsterdam (1986)

[26] M. Beghi, C.E. Bottani, P.M. Ossi, T. Lafford and B.K. Tanner, J. Appl. Phys. **81**, 672 (1997)

[27] A. Amici, M.G. Beghi, C.E. Bottani, Computational Material Science **17**, 404 (2000)

[28] P.A. Egelstoff, "An Introduction to the Liquid State", Clarendon Press, Oxford (1992), p.286

[29] M. Shimoji, "Liquid Metals", Academic Press, (1997)

[30] V.L. Ginzburg, A.P. Levanyuk, A.A. Sobyanin, Physics Reports **57**, 151 (1980)

[31] A.N. Fitch, Materials Science Forum **228**, 219 (1996); see also: www.esrf.fr

[32] W. Parrish, M. Hart, T.C. Huang, J. Appl. Cryst. **19**, 92 (1986)

[33] T.C. Huang, M. Hart., W. Parrish, N. Masciocchi, J. Appl. Phys. **61**, 2813 (1987)

[34] W. Parrish, M. Hart, Z. fur Kristall. **179**, 161 (1987)

[35] W. Parrish, M. Hart, Australian J Phys. **41**, 403 (1988)

[36] M. Hart, R.J. Cernik, W. Parrish, H. Toraya, J. Appl. Cryst. **23**, 286 (1990)

[37] K.G. Lyon, G.L. Salinger, C.A. Swenson, G.K. White, J. Appl. Phys. **48**, 865 (1977)

[38] A.K. Freund, J.A. Gillet, L. Zhang, SPIE Conf. On Crystal and Multilayer Optics, San Diego, vol. 3448 (1998)

[39] Y. Okada, Y. Tokumaru, J. Appl. Phys. **56**, 314 (1984)

[40] H.-Matsuo Kagaya, N. Shoji, T. Soma, Phys. Stat. Sol. B **142**, K13 (1987)

[41] Bond W.L., "Crystal Technology", John Wiley & Sons (1976)

[42] "Handbook of Physical Quantities", edited by I.S. Grigoriev and E.Z. Meilikhov, CRC Press (1997)

[43] S.B. Qadri, J.P. Yang, E.F. Skelton, B.R. Ratna, Appl. Phys. Lett. **70**, 1020 (1997)

[44] W.H. Hall, Proc. Phys. Soc. London, Sec. A **62**, 741 (1949)

[45] G.K. Williamson, W.H. Hall, Acta Metall. **1**, 22 (1953)

[46] H.P. Klug, L.E. Alexander, "X-Ray Diffraction Procedures For Polycrystalline and Amorphous Materials", John Wiley & Sons (1974)

[47] A. Roy, A.K. Sood, Sol. St. Comm. **97**, 97 (1996)

[48] L. Saviot, B. Champagnon, E. Duval, A.I. Ekimov, Phys. Rev. B **57**, 341 (1998)

[49] M. Fujii, T. Nagareda, S. Hayashi, K. Yamamoto, Phys. Rev. B **44**, 6243 (1991)

[50] A. Dieguez, A. Romano-Rodriguez, J.R. Morante, N. Barsan, U. Weimar, W. Goepel, Appl. Phys. Lett **71**, 1957 (1997)

[51] N.N. Ovsyuk, E.B. Gorokhov, V.V. Grishchenko, A.P. Shebanin, Pis'ma Zh. Eksp. Teor. Fiz. 47, 248 (1988) [JETP Lett. **47**, 298 (1988)]

[52] A. Tanaka, S. Onari, T. Arai, Phys. Rev. B **47**, 1237 (1993)

[53] M. Ferrari, F. Gonella, M. Montagna, C. Tosello, J. Appl. Phys. **79**, 2055 (1996)

[54] E. Duval, A. Boukenter, B. Champagnon, Phys. Rev. Lett. **56**, 2052 (1986)

[55] L. Saviot, B. Champagnon, E. Duval, I.A. Kudriavtsev, A.I. Ekimov, J. Non-Cryst. Sol. **197**, 238 (1996)

[56] B. Palpant, H. Portales, L. Saviot, J. Lerme, B. Prevel, M. Pellarin, E. Duval, A. Perez, M. Broyer, Phys. Rev. B **60**, 17107 (1999)

[57] P. Verma, W. Cordts, G. Irmer, J. Monecke, Phys. Rev B **60**, 5778 (1999)

[58] J. Zhao, Y. Matsumoto, Phys. Rev. B **60**, 4481 (1999)

[59] J. Zi, K. Zhang, X. Xie, Phys. Rev. B **58**, 6712 (1998)

[60] H. Lamb, Proc. London Math. Soc. **13**,189 (1882)

[61] A. Tamura, T. Ichinokawa, J. Phys. C **16**, 4779 (1983)

[62] M. Montagna, R. Dusi, Phys. Rev. B **52**, 10080 (1995)

[63] E. Duval, Phys. Rev. B **46**, 5795 (1992)

[64] H. Olijnyk, Phys. Rev. B **46**, 6589 (1992)

[65] S.H. Chen, Phys. Rev. **163**, 532 (1967)

[66] S.P. Lewis, M.L. Cohen, Phys. Rev. B **48**, 3646 (1993)

[67] J.M. Rowe, Phys. Rev. **163**, 547 (1967)

[68] A.S. Ivanov, N.L. Mitrofanov, A.Yu. Rumiantsev, Physica B **213&214**, 423 (1995)

[69] A.S. Ivanov, N.L. Mitrofanov, A.Yu. Rumiantsev, M.N. Khlopkin, N.A. Chernoplekov, Sov. Phys. Solid State **29**, 977 (1987)

[70] M. Holt, Z. Wu, H. Hong, P. Zschack, P. Jemian, J. Tischler, H. Chen, T.-C. Chiang, Phys. Rev. Lett. **83**, 3317 (1999)

[71] N.N. Ovsyuk, V.N. Novikov, Phys. Rev. B **53**, 3113 (1996)

[72] Gerard Koops, private communication

[73] G. Cerullo, S. De Silvestri, U. Banin, Phys. Rev. B **60**, 1928 (1999)

[74] N. Del Fatti, C. Voisin, F. Chevy, F. Vallee, C. Flytzanis, J. Chem. Phys. **110**, 11484 (1999)

[75] M. Nisoli, S. De Silvestri, A. Cavalleri, A.M. Malvezzi, A. Stella, G. Lanzani, P. Cheyssac, R. Kofman, Phys. Rev. B **55**, R13424 (1997)

[76] G. Mariotto, M. Montagna, G. Viliani, E. Duval, S. Lefratnt, E. Rzepka, C. Mai, Europhys. Lett. **6**, 239 (1988)

Chapter 7

Conclusions

7.1 Summary

This chapter will review the experimental results presented in the thesis and summarise the main conclusions that have been drawn.

The aim of this thesis work was the study of different nanostructured thin films, and carbon films in particular, with inelastic light scattering (Raman and Brillouin spectroscopy) and x-ray scattering techniques (mainly x-ray diffraction and x-ray reflectivity).

The main research undertaken was the characterisation of cluster-assembled carbon films grown with a supersonic cluster beam apparatus (PMCS, Pulsed Microplasma Cluster Source); it has been introduced and discussed in chapter 5. These films look promising for applications in the field of catalysis, supercapacitors, hydrogen storage and field emission (e.g. for flat panel displays). Moreover they are interesting for the study of the relationship between the properties of the clusters and those of the deposited nanostructured material ("memory effect"). Raman spectroscopy showed that the local bonding in the films is reminiscent of the size distribution of the precursor clusters. Deposition of larger clusters resulted in more graphitic carbon films, while deposition of smaller clusters led to carbon films of a more amorphous nature. It was demonstrated that it is possible to select the cluster size in order to deposit films with different, tailored properties. Moreover Raman spectroscopy gave a contribution to understanding the arc-discharge mechanism and the source functioning, and showed the growth of nanotubes and onion-like forms of carbon inside the source. Brillouin scattering demonstrated the difference at a mesoscopic scale between the films grown with a non-focused beam and the compact, smoother films grown using a focused beam. In the case of non-focused beam, the huge surface roughness was shown to increase as a function of thickness. An estimate of the elastic constants was obtained, revealing a value of the shear modulus similar to that of graphite. The value of the bulk modulus is very low, which is typical of a soft material with voids. Films grown with

smaller precursor clusters had lower values for the elastic constants. Additional information was provided by XRR (density of the films), WAXS (absence of relevant crystalline domains in the material) and SAXS (possible fractal-like character of the surface).

As an extension of the programme on cluster-assembled carbon films, a collaboration was started with the University of Cambridge for the study of density, layering and surface roughness of a wide range of amorphous carbon films, using X-ray reflectivity. These films were assembled "atom by atom" with traditional deposition techniques. The results of this collaboration were presented in Chapter 4. XRR was shown to be the best technique for obtaining the density of pure, hydrogen-containing and nitrogen-containing amorphous and tetrahedral amorphous carbon films. XRR from carbon films presents some peculiarities when compared to the standard application of this technique. The critical angle is very similar to (and sometimes smaller than) that of the Si substrate, the films often possess an irregular, unwanted (and thus unforeseen) internal layering, with a density which is varying along the direction normal to the surface, and the elemental composition of the films is often unknown. These aspects were studied in order to give to XRR from carbon films the character of a standard technique. By comparing XRR results with EELS results, a unique value for the effective mass was deduced and a general relationship between sp^3 content and density was found (and proved to be depending on the hydrogen content). Lack in uniformity was detected in filtered cathodic vacuum arc ta-C films and assigned to plasma instabilities in the deposition apparatus. Use of x-ray reflectivity is non-destructive and timesaving with respect to cross-sectional EELS or TEM, sometimes employed in the past. The evolution of roughness with thickness was studied, as well as the effect of etching on thin films. XRR provided a characterisation essential for the analysis and interpretation of Brillouin scattering measurements from ta-C films performed at Politecnico di Milano, being capable of obtaining information from very thin films (about 3 nm). Finally, it was proved how a combination of XRR and H effusion can be used to determine with good accuracy the hydrogen content in carbon films.

The last chapter was devoted to the discussion of the combined use of x-ray diffraction and inelastic light scattering for the study of the size-dependent melting temperature in tin nanoparticles, embedded in silica thin films. A small redshift in the position of a surface Rayleigh peak detected by Brillouin spectroscopy in the

temperature-dependent measurements was shown by XRD to be directly related to the melting of the nanoparticles. The redshift was explained by an effective medium model accounting for the softening of the film shear modulus upon melting. The melting temperature is a well-defined function of size, as theoretically predicted and confirmed also by these experiments. XRD clarified the crystalline nature of the inclusions and their random orientation, and provided also information on the low level of stress in the embedded particles. Finally, low-frequency Raman scattering was used to study the behaviour of the acoustic modes of a single particle as a function of temperature, showing the coupling between these modes and some relaxation of the degrees of freedom, through a damping process.

In summary, it has been demonstrated that a combination of x-ray and inelastic light scattering can provide a great deal of insight in the structural characterisation of nanostructured thin films, and that the combination of these scattering techniques with other techniques is a powerful tool for the investigation of these peculiar materials. X-ray and inelastic light scattering have the advantage of being fast and non-destructive techniques. The wavelength range attainable (by changing the excitation from visible to ultra-violet or infra-red in Raman spectroscopy or by changing the x-ray energy in x-ray scattering experiments) accounts for their flexibility, i.e. these investigation techniques can be used to study phenomena occurring over a wide range of length scales (atomic ordering with XRD, atomic vibrational dynamics with Raman scattering, particle acoustic vibrations with low-frequency Raman scattering, mesoscopic elastic properties with Brillouin scattering, mesoscopic structure of thin films with XRR, self-affine or fractal structure and dynamics with SAXS and Brillouin scattering).

7.2 Further work

In the framework of the cluster-assembled carbon films project, the future directions of research point towards a better characterisation of the source control, in order to achieve a sharp selection of the cluster size and energy distribution. Moreover, possible applications of these films will be tested within the context of an international research collaboration between universities and private companies financed by the European Community. The field emission properties of these materials rely upon the capability of growing very thin films. Also, the investigation of the first stages of growth of cluster-assembled films is a challenging task, and can provide useful

information on the cluster mobility and aggregation, and the growth mechanisms of the very first layers. For all these reasons, the portable cluster source (CLARA) has been designed and realised, and will be coupled with several diagnostic techniques in the next months. Among these techniques, in-situ Raman scattering will be very useful for the comprehension of the first stages of the deposition phenomena. Brillouin scattering measurements are currently being carried out to study in more detail the effect of the multiscale disorder on the vibrational spectrum (i.e. the central peak).

Although some works concerning X-ray reflectivity from carbon films have been published in the past, we believe that the wide spectrum of investigation carried out in this thesis work on almost all possible carbon films, pure and heterogeneous, and published in major scientific journals, will set this technique as a standard and fast tool for the characterisation of several properties of these films. Currently, measurements on SiC films are being performed, and we think that a detailed investigation of the effects of the deposition conditions on the surface roughness is what is most needed at the moment.

The study of embedded nanoparticles is also very interesting. In particular, the study of the particle acoustic vibrations by low-frequency Raman scattering and their coupling with the central peak through some relaxation process is a challenging problem. Similar investigations are being currently carried out to study these phenomena in semiconductor nanoparticles/amorphous matrix systems.

In summary, the work carried out had a heterogeneous character, both in the systems investigated and in the experimental techniques adopted. The unifying elements were the use of scattering from electromagnetic radiation and the study of films presenting some sort of nanostructure. The use of these techniques to characterise nanostructures is very recent and still not standardised, since interesting and peculiar features must be taken into account when passing from bulk materials to systems presenting some degree of confinement over a nanometre scale. The combination of inelastic light scattering and x-ray reflectivity applied to nanostructured thin films has proved to be capable of providing a great deal of information, especially when completed by other experimental investigations. Beside the materials characterisation aspect, we must also consider that interesting phenomena, related to confinement and disorder effects, and still lacking detailed investigation, manifest themselves in nanosystems similar to those here discussed.